



Estimation of hepatic tumors respiratory motion
using learning algorithms and surrogates

M. (Maryam) Berijanian

MSc Report

Committee:

Dr.ir. M. Abayazid
H. Naghibi Beidokhti, MSc
Dr. B. Sırmaçek
Dr.ir. F. van der Heijden
Dr. C. Brune

October 2018

043RAM2018
Robotics and Mechatronics
EE-Math-CS
University of Twente
P.O. Box 217
7500 AE Enschede
The Netherlands

Estimation of hepatic tumors respiratory motion using learning algorithms and surrogates

M. (Maryam) Berijanian

October 25, 2018

Summary

The respiratory motion in the abdomen is an important source of inaccuracy in clinical applications such as image-guided interventions (e.g. radiotherapy and tumor ablation) and image acquisition (e.g. MRI). The inaccuracies introduced to the treatments or diagnostic tests raise the probabilities of misdiagnosis, incomplete treatment, or destruction of healthy tissues.

Among the possible solutions to these problems, much attention has been paid to respiratory motion estimation by means of surrogate signals, in order to compensate the respiratory motion and target the points of interest more accurately.

In this study, a correlation between the collected surrogate signals and the liver tumor respiratory motion is obtained using learning-based algorithms. A robotic phantom is developed which simulates the respiratory motion of the liver, the diaphragm, and the abdomen skin in two directions as superior-inferior (SI) and anterior-posterior (AP). The surrogate signals are collected by means of optical markers attached to the abdomen skin and tracked by a digital camera, in addition to an inertial measurement unit (IMU) fixed to the hub of a plastic needle which is inserted into the liver. The liver incorporates a spherical tumor, the displacement of which is measured by an electromagnetic sensor. Using a finite element (FE) model which is developed based on the data collected from the physical phantom as the ground-truth, more surrogate and tumor motion data is generated with different values of parameters such as the tumor size, the tumor location in the liver, and the liver elasticity which differ among patients. Subsequently, a learning algorithm is employed to find a correlation between the tumor respiratory motion and the surrogate signals. A sensitivity analysis is also performed in order to find the effects of the parameters on the tumor respiratory motion. Also, the performance and estimation error of the learning-based model is compared between the estimation results from the measurement data and the results from the simulated data.

It is shown that the estimation error of linear regression for the SI and AP directions has been respectively 1.37% and 2.87%, and for quadratic polynomial regression have been 0.76% and 2.41% on the data from the experiments. With the presented phantom design, it is not possible to draw a general conclusion about which surrogate signals have higher correlation with the tumor motion, since it depends completely on the data set. However, by combining all surrogate signals, the estimation error decreases about 0.5-6.5% comparing to using only one of the surrogates. The sensitivity analysis shows that the simulation results are partly correct, and the main difference between the results and the literature information is due to the limitations in the phantom and FEM. Finally, it is discussed that by augmenting the measurement data with the simulated data, the motion estimation error changes from 2.9% to 2%, which is not significant and suggesting that the FEM is a sufficiently good representation of the experimental setup.

Contents

1	Introduction	1
1.1	Anatomical terminology	1
1.2	Liver cancer and clinical procedures	1
1.3	Challenges and common solutions	2
1.4	Respiratory motion estimation using surrogate signals	3
1.5	Objectives and research questions	6
1.6	Work-flow	7
1.7	Thesis outline	8
2	Improvement of a respiratory motion phantom	11
2.1	Properties of hepatic respiratory motion	11
2.2	Initial phantom design	12
2.3	Improvements of phantom design	13
2.4	MR-compatibility test	24
2.5	Summary and important notes	25
3	Sensors and experimental setup	27
3.1	Motion of interest and surrogate signals in similar works	27
3.2	Sensors and experimental setup	28
3.3	Data post-processing	30
3.4	Finite element model	35
3.5	Summary	35
4	Supervised-learning results from the experimental data	37
4.1	Experimental data	37
4.2	Selecting appropriate algorithms for the problem	37
4.3	Optimization and acquiring the models	40
4.4	Motion estimation results and performances	44
4.5	Comparison between the surrogate signals	52
4.6	Summary	55
5	Model generalization with FEM	57
5.1	Creation and validation of FE model	57
5.2	Data sampling frequency	59
5.3	Sensitivity analysis	59
5.4	Generalization of the regression model	65
5.5	Summary	69

6 Conclusion and recommendations	71
A Arduino code for the phantom motion with digital regulator	73
B MATLAB script for image segmentation based on color thresholds	75
Bibliography	77

1 Introduction

In this chapter the problem statement will be defined. First, related backgrounds and literature will be reviewed. Following that, the purpose of this project is explained, and then the outline of the next chapters will be presented.

1.1 Anatomical terminology

Figure 1.1 shows the anatomy of the human body's chest and abdomen. The liver is located in the abdomen, in contact with the diaphragm.

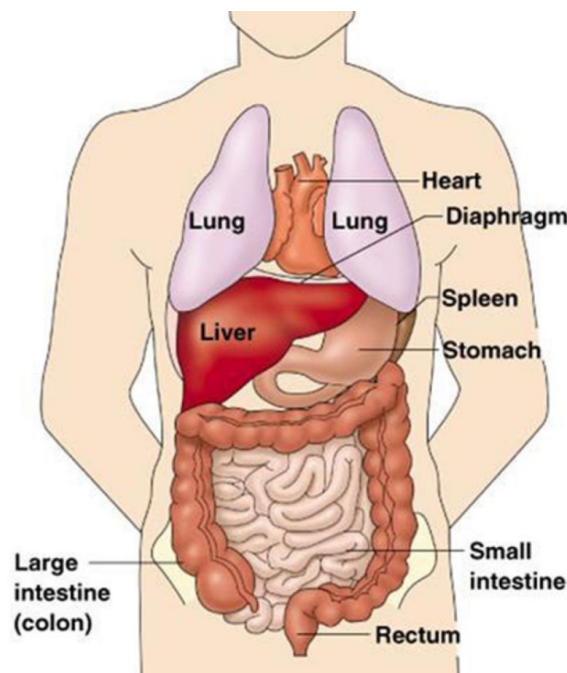


Figure 1.1: Anatomy of the abdomen and chest of the human body [24].

Figure 1.2 demonstrates some of the directional terms used for human body. The anterior-posterior (AP), superior-inferior (SI), and medial-lateral (ML) directions are respectively back-front, head-foot, and right-left directions, which are the main focus in this report.

1.2 Liver cancer and clinical procedures

According to World Health Organization (WHO) [31], cancer is the second cause of total deaths worldwide. Liver or hepatic cancer is the second most common cause of cancer death and it was responsible for 788,000 deaths in 2015. About two thirds of cancer deaths occur in lower-income countries, where the diagnosis and treatment services are less accessible [32]. It means that early diagnosis and treatment increase the survival chance. Due to the mentioned issues and the high death rate of liver cancer, this project focuses on liver and liver tumor.

The clinical diagnosis and treatment procedures are as follows.

- The diagnostic procedures consist of: blood test, ultrasound scan, CT scan, MRI scan, and biopsy [50].
- Some types of treatments are: ablation, embolization, immunotherapy, surgery, radiotherapy, and chemotherapy [44], [51].

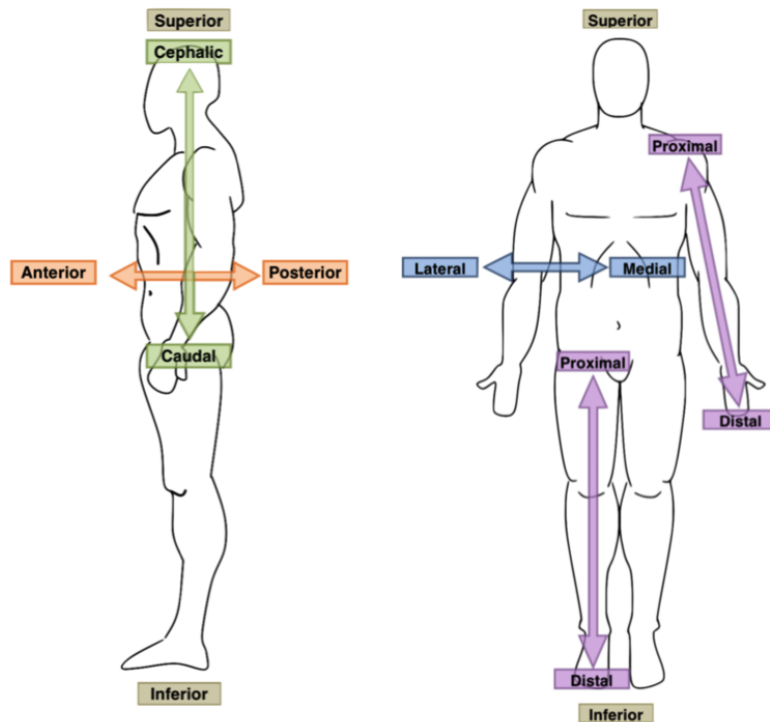


Figure 1.2: The anatomical terms of location shown on the human body [27].

1.3 Challenges and common solutions

The organ motion secondary to the respiration has been always one of the challenges in the aforementioned clinical procedures. It is not always possible to observe the organ of interest directly in real-time, since the updating rate of the imaging modalities are not high enough (specifically in MR imaging), or in some cases, the organ is not observable and is hidden by other organs or tissues, or the imaging devices are not capable of deep imaging (for example ultrasound).

In the treatments and image-guided interventions such as radiotherapy, surgery, tumor ablation, and biopsy, the information about the lesion's position is affected by the respiratory motion [25], [2].

The inaccuracies of the lesions position and images induced by the respiratory motion affect the quality of diagnosis and treatment and cause misdiagnosis, insufficient treatment, or destruction of healthy tissues.

In order to minimize the inaccuracies, several strategies have been employed in the literature [2], [29]:

- **Breath holding:** It is the simplest approach, but limits the duration of the procedure to less than 30 seconds, which is not usually sufficient.
- **Respiratory gating:** The lesions are scanned constantly and during a limited window of the respiratory cycle. This method increases the duration of the procedure.
- **Respiratory motion estimation:** In this method, it is possible to track the motion of the points of interest in real-time, in contrast with the previous methods. This method can be performed in different ways:

- Real-time imaging of the tumor: It is difficult to acquire the motion via imaging during the medical procedure, and the updating rate of the image acquisition can be low and insufficient for accurate tracking.
- Imaging of the markers or receiving signals from devices implanted close to the tumor: This method is invasive and it is challenging to put the implants close to the lesion. Also, only the motion of the markers is tracked instead of the region of interest.
- Correlating an external surrogate signal with the actual tumor position: One of the limitations of this method is the fact that the surrogate signal must have a strong correlation with the actual tumor motion.

In this project, the last approach (respiratory motion estimation using external surrogate signals) has been chosen, because of the mentioned drawbacks and limitations of the other methods. Also, the advantage of this method is that the updating rate of the surrogate signals can be high, which makes it a suitable method for real-time applications.

1.4 Respiratory motion estimation using surrogate signals

This section gives more information about the approach of respiratory motion estimation.

1.4.1 Previous works

Table 1.1 includes a number of studies in the literature about respiratory motion estimation of abdominal organs using surrogate signals. Although various methods for the estimation of the respiratory motion of different organs exist in the literature, they have the following components in common [2]:

- Surrogate signals: the signals that are used as inputs to estimate the respiratory motion of the region of interest. They should be easily measurable, have a strong relation with the respiratory motion, and have a sufficiently high updating frequency.
- Motion models: a model that correlates the input (surrogate) signals with the output (the actual motion of the region of interest) and is capable of estimating the output signal given the input signals.
- Fitting methods: a method that is used to fit the correlation between the surrogate and output signals, which is called typically a supervised learning algorithm.
- The estimated motion of the region of interest: if the relation between the surrogate signals and the motion of interest is successfully modeled, then the output of the model will be an estimation of the motion of interest.
- The actual motion of the region of interest: this signal is used as a ground truth to find a motion model and is compared to the estimated output in order to calculate the errors of the estimation.

Figure 1.3 shows the procedures and components of the respiratory motion estimation using surrogate signals. In Figure 1.3-(a) the learning phase is observable, in which the external surrogate signals and the actual motion of the region of interest are measured simultaneously during a validation experiment. Then, a correlation between them is found using a fitting method, and the motion model is built. Figure 1.3-(b) shows the estimation phase, in which the previously-made motion model is used to estimate the motion of interest (the output) from the surrogate signals (inputs). In this phase, only the surrogate signals are measured during the experiment.

Table 1.1: Related studies about respiratory motion estimation using surrogate signals. Typical surrogate signals, the motion of interest measurement methods, and the means of validation experiments are listed.

Reference	Surrogate signals	Motion of interest	Validation experiments
Abayazid et al., 2018 [29]	IMU ^a	EM ^b tracker	motion phantom
Fahmi et al., 2018 [25]	external markers	MRI	human subjects
Shin et al., 2017 [46]	digital protractor & calipers	4D CT	motion phantom
Ahn et al., 2014 [7]	radio-opaque markers	fluoroscopic images	human subjects
Durichen et al., 2013 [9]	multi-modal sensors	3D ultrasound	human subjects
Lei et al., 2012 [36]	EM tracker	CT scan	animals & saline bags
Cerviño et al., 2010 [41]	fluoroscopic images	fluoroscopic images	human subjects
Torshabi et al., 2010 [10]	external markers	X-ray imaging	human subjects
Ehrhardt et al., 2010 [12]	4D CT	4D CT	human subjects
Cerviño et al., 2009 [40]	fluoroscopic images	fluoroscopic images	human subjects
Ernst et al., 2009 [1]	active optical markers	X-ray imaging	human subjects
Beddar et al., 2007 [39]	external markers	4D CT	human subjects
Ionascu et al., 2007 [35]	abdominal surface motion	markers & x-ray	human subjects
Lu et al., 2005 [17]	spirometry & abdominal motion	4D CT	human subjects
Isaksson et al., 2005 [28]	external markers & fluoroscopy	markers & fluoroscopy	human subjects
Hoisak et al., 2004 [18]	spirometry & abdominal motion	X-ray fluoroscopy	human subjects
Ahn et al., 2004 [6]	external markers & fluoroscopy	fluoroscopy	human subjects
Koch et al., 2004 [4]	external markers & MRI	MRI	human subjects
Vedam et al., 2003 [37]	markers & infrared camera	fluoroscopy	human subjects
Schweikard et al., 2000 [19]	infrared emitters	X-ray imaging	human subjects

^aInertial Measurement Unit

^bElectromagnetic

Once the motion model is built in the learning phase, it can be used to estimate the motion of interest in real-time if the surrogate signals are measured in real-time (with a high updating rate).

1.4.2 Literature gap

Most of the relevant works emphasize that the respiratory motion pattern changes from cycle to cycle (inter-cycle variations), between different patients (inter-patient variations), between different treatment sessions (inter-fraction variations), etc. [2]. Several papers have neglected the mentioned variations for simplification in their works, while many studies have considered them to an extent. However, rather less studies have taken the effects of the following patient-specific parameters on the tumor respiratory motion or on the estimation model into account:

- Size of the tumor
- Shape and deformations of the tumor
- Location of the tumor inside the organ
- Properties of the organ tissues (e.g. elasticity and density of the tissue), which depends on the percentages of the main tissue, fat, blood vessels, etc.
- Properties of the tumor tissue
- The breathing pattern (e.g. diaphragmatic (deep), thoracic (shallow))
- The position of the sensors, trackable markers, etc. relative to the moving organs and regions of interest

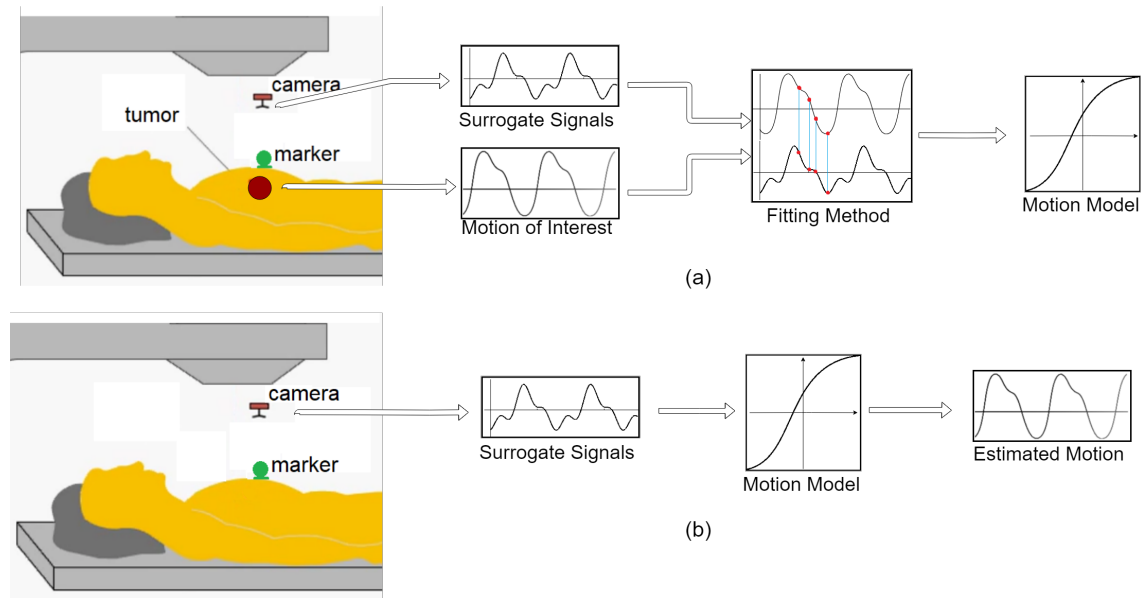


Figure 1.3: Schematic view of the steps of the respiratory motion estimation using surrogate signals. (a) The learning phase, (b) The estimation phase.

Table 1.2 shows the relevant works that considered the effects of some of the mentioned parameters on the respiratory motion of interest or on the estimation/simulation/imaging accuracy.

Table 1.2: Related studies considering the effects of some parameters on the respiratory motion of interest or on the estimation/simulation/imaging accuracy.

References	Parameters	Effects on the motion or estimation
Plathow et al., 2004 [14], Liu et al., 2007 [23], Ehrhardt et al., 2010 [12], Cai et al., 2008 [20]	tumor size	Larger tumors have smaller amplitude of motion and they reduce the mobility of the malignant organ as well. Also, the resulting images are less blurry.
Liu et al., 2007 [23], Ehrhardt et al., 2010 [12]	tumor location in AP ^a direction	Tumors closer to the posterior chest wall have smaller motion amplitudes.
Plathow et al., 2004 [14], Liu et al., 2007 [23]	tumor location in SI ^b direction	Tumors closer to the diaphragm have larger motion amplitudes.
Plathow et al., 2005 [26], Koch et al., 2004 [4], King et al., 2008 [22]	breathing pattern ^c	The respiratory motion amplitude is larger in deep breathing and the correlation between the surrogates and motion of interest is higher
Fahmi et al., 2018 [25], Ahn et al., 2014 [7], Chi et al., 2006 [45], Liu et al., 2004 [3]	position of sensors or markers (on the abdomen or the chest)	The internal respiratory motion in SI direction has the highest correlation with the abdominal motion and in AP direction with the chest motion

^aAnterior-Posterior

^bSuperior-Inferior

^cdeep (abdominal), shallow (thoracic or normal)

To the author's knowledge, some of the mentioned parameters have not been taken into account in the literature. The rest of the parameters have been considered in a few studies as in Table 1.2. Although they investigated the effects of the parameters on the results, they did not use the mentioned parameters as inputs to the motion model and learning algorithm in order to quantify the respiratory motion dependency on the parameters and increase the accuracy

of the model. In this project, the effects of the parameters: tumor size, liver elasticity, and tumor location inside the liver on the respiratory motion estimation are investigated and used as inputs to the supervised learning algorithm.

Some studies have created a simulation model of the respiratory motion of the organ of interest instead of motion-estimation via learning algorithms in order to investigate the effects of different parameters on the respiratory motion. In a study by Tehrani et al. as well as Werner et al. a finite element model of the lung and lung tumor has been created [15, 16]. In the former, the sensitivity of the simulation model accuracy to the tissue properties (e.g. elasticity) as well as the modeling approaches has been evaluated and in the latter, the effects of lung tumor size and location on the simulation accuracy are reported.

In most of the studies, the validation and testing experiments have been conducted on human subjects. An exception is [36], in which animals and saline bags have been used for the experiments as in Table 1.1. Also, [29] and [46] have made use of motion phantoms.

Since the respiratory motion of tumors depends on numerous parameters and variations as mentioned and is unique for each patient, it is not possible to completely and accurately observe the effects of the changes in the parameters on the respiratory motion. However, through phantom experiment setups or simulations, the procedures are repeatable and the parameters can be controlled and manipulated. For example, due to inter-fraction variations, the respiratory motion pattern of a specific patient changes from one diagnosis session to another. Nevertheless, in a simulation, it is possible to change one of the parameters while fixing the rest parameters and the respiratory pattern in order to observe the effects of the changing parameter.

In this project, a respiratory motion liver phantom is developed in order to collect the motion of interest and surrogate data via experiments. Also, a finite element model (FEM) was used in order to make the possibility of changing the mentioned parameters and observing the resulting changes quantitatively, and generating more input and output data sets for supervised learning and motion estimation model. The main reason of using FEM instead of repeating the experiments has been the fact that the repeat-ability of the experiments with the phantom has been low. It was not possible to keep all parameters the same while changing only one of the parameters. The difference between the papers that have used FEM ([15, 16]) and this project is that they simulated the respiratory motion in order to investigate the effects of certain parameters or modeling approaches on the FE model accuracy, while in this project FEM is used to simulate the experiments in order to generate surrogate and motion data for a learning algorithm which quantifies the tumor motion dependency on the parameters.

This project is related to [29] and [25] as well, in which the hepatic tumors motion secondary to respiration has been estimated using supervised learning algorithms and surrogate signals. The former used the outputs of an IMU attached to the hub of a needle inserted into a respiratory motion phantom as surrogate signals, while the latter used the displacement of external markers placed on human subjects' abdomen and tracked by a digital camera as surrogate signals. Another goal of this work is to use both IMU and external markers as surrogates in order to make a comparison between them in terms of the resulting performance and accuracy of the learning-based motion estimation.

1.5 Objectives and research questions

The objectives of this project are:

- improving an already existing robotic phantom to mimic the hepatic respiratory motion more realistically (Chapter 2),

- designing an experimental setup with the phantom and sensors in order to collect the respiratory motion of interest and surrogate data through experiments (Chapter 3),
- liver tumor's respiratory motion estimation using supervised learning algorithms and surrogate signals (Chapters 4 and 5),
- modeling the experiments by FEM (made and validated by a colleague¹ from the experimental data of the physical phantom) to generate more data sets for different parameters (Chapter 5).

Also, the research questions are as follows, which will be answered in the next chapters.

- Which surrogate signals have a higher correlation with the tumor motion? (Answered by comparing the estimation accuracy for different choices of surrogates in Chapter 4.)
- What are the effects of the parameters (tumor size, liver-tissue elasticity, and tumor location in the liver) on the tumor motion in this work? Are the results different from the previous works? (Answered by sensitivity analysis in Chapter 5.)
- Is it possible to extend the experimental data with FE simulations with a comparable accuracy? How does the motion estimation error change? How good is the FE model? (Answered by comparing the results of learning-based models in Chapter 5.)

1.6 Work-flow

Following are more details about the general work-flow and steps of this project, which are shown in Figure 1.4.

The first phase of the project is done as illustrated in part (a) of the figure. A robotic phantom which mimics the hepatic respiratory motion is improved using the information about the respiratory cycles and the physical properties of the liver from the literature. These specifications affect the choice of actuators, system design, and control.

Then, experiments are performed on the robotic phantom in order to measure the surrogate signals and the motion of the liver tumor. Following that, given the physical properties of the liver, a finite element model (FEM) for simulating the phantom respiratory motion is developed and validated by a colleague¹ using the experimental data.

The second phase of the project is data generation and machine learning as shown in part (b) of Figure 1.4.

As it is noticeable in Figure 1.4-(b), the aforementioned parameters (tumor size, liver elasticity, and tumor location inside the liver) are changed in the previously developed FEM and various sets of motion data and surrogate signals are generated via FEM simulations.

Next, all sets of data (for different parameters) are used in a supervised-learning algorithm in order to find a correlation between the inputs (surrogate signals) and outputs (tumor motion). This results in a respiratory motion model, which can be used for motion estimation.

Figure 1.4-(c) shows the last (third) phase of the project, which is the testing and evaluation phase. In this phase, a new set of surrogate data from either the phantom experiments or the FEM simulations is used as the input of the previously made motion model and the output is estimated which is the tumor motion.

The final step is that the estimated tumor motion is compared with the measured or simulated tumor motion from the phantom or FEM in order to evaluate the accuracy and the performance of the learning-based model. The data used for the estimation in this phase should not be used

¹ Hamid Naghibi Beidokhti M.Sc

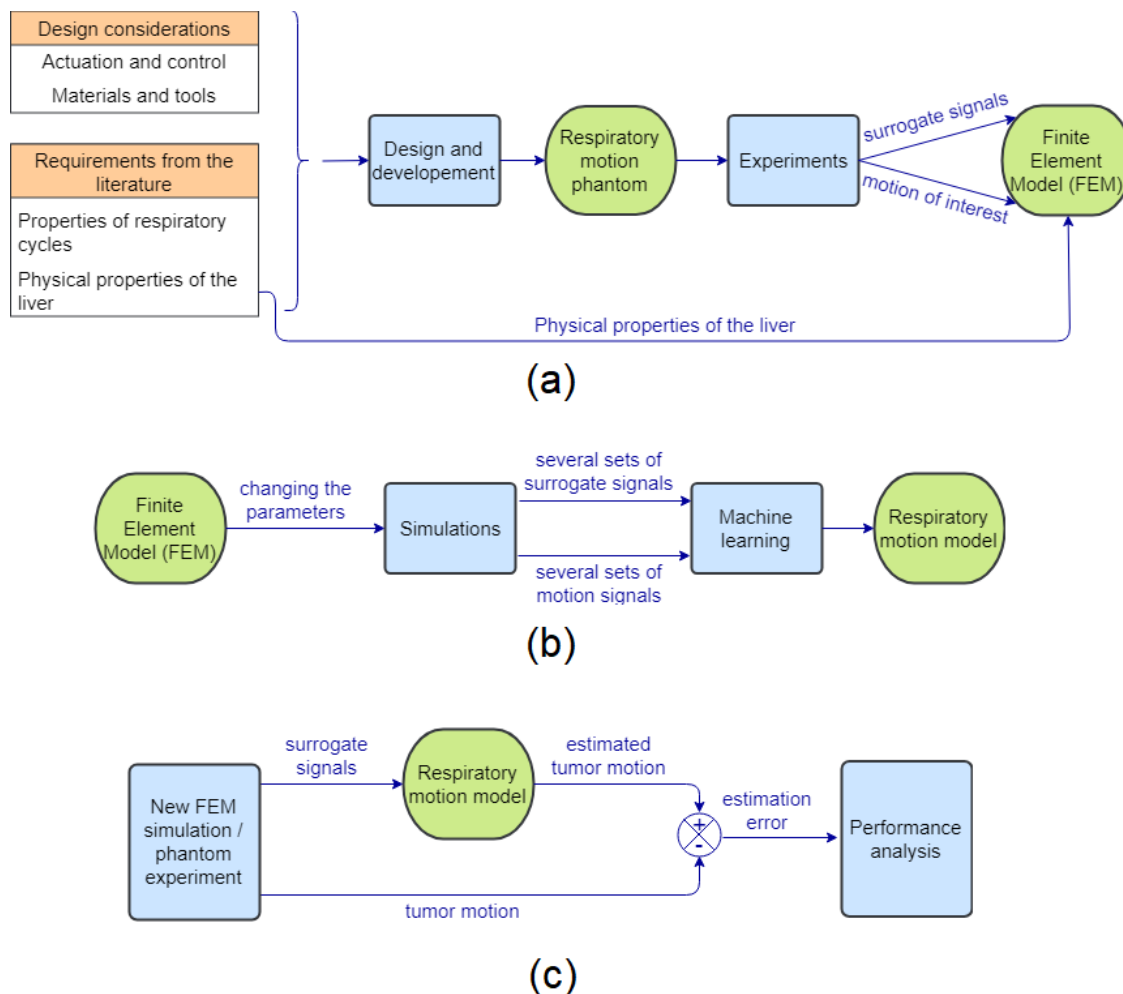


Figure 1.4: The steps of the project. (a) The practical phase, (b) data generation and machine learning, and (c) testing and evaluation.

for the machine learning in the previous phase, as it will not be a proper way of evaluating the accuracy.

1.7 Thesis outline

This report is organized as follows.

Chapter 2 explains how the robotic phantom that mimics the hepatic respiratory motion and is used for the experiments is developed and how different parts of the phantom are designed and controlled.

In Chapter 3, an explanation of the types of surrogate signals and sensors that have been chosen for this project is given. Then, the experimental setup is described along with the procedure of the experiments. Next, the experiment data post-processing is explained. This chapter ends with a description of how the finite element model is created and contributes to this project.

Chapter 4 analyzes the data obtained from two experiments and demonstrates what kind of supervised-learning algorithm is most suitable for the data and how the mathematical motion model is acquired for the respiratory motion estimation. Then, the results of the learning algorithms and the motion estimation are presented. In addition, a comparison is made between the performances of different algorithms. Finally, different surrogate signals are compared in

terms of their contribution to the resulting motion-estimation accuracy (which is the answer to one of the research questions).

In Chapter 5, by performing a sensitivity analysis on the data sets generated by FEM, the effects of the parameters (tumor size, liver elasticity, and tumor location inside the liver) on the resulting motion are analyzed and compared with the information from the literature. Then, the previously created supervised-learning algorithm is generalized to include the parameters. Next, the data sets are used as inputs to the generalized code to evaluate the estimation accuracy. This chapter ends with answers to the remaining research questions.

In Chapter 6, a conclusion is given along with recommended future works and researches.

2 Improvement of a respiratory motion phantom

This chapter describes the hepatic respiratory motion based on the literature and how an already existing respiratory motion phantom is improved. First, the properties and patterns of the hepatic respiratory motion is presented according to the literature. Next, the initial motion phantom designed by the former master's student Paulo Costa [33] is presented. Then, its weaknesses and drawbacks are discussed as well as how it can be improved in order to make it more similar to the real respiratory motion of human body. Finally, the procedure of improving the motion phantom to make it suitable for the experiments of this project is explained along with a description of how different parts are designed and how they work.

2.1 Properties of hepatic respiratory motion

In this project, as shown in Figure 1.4 of Chapter 1, the aim is to simulate the respiratory motion by the robotic phantom with a good approximation, to use it for an experiment and collection of surrogate signals and motion of interest signals, and then to make a FE model of the liver and liver tumor's respiratory motion using the collected signals for validation. The experiment that is performed on the phantom represents the hepatic respiratory motion for one case. As shown in Figure ?? of Chapter 1, once the FE model is created, it is used for simulating other cases, e.g. for other breathing modes, or for other parameters such as the tumor size, the tumor location in the liver, and the liver elasticity.

As shown in Figure 1.4 of Chapter 1, the requirements for the design of the respiratory motion phantom are the properties of respiratory cycles, which are derived from the literature. The reason is that the phantom is intended to mimic the hepatic respiratory motion realistically; therefore, it should be created in accordance with the real respiratory cycles' properties and patterns that are reported in the literature.

The properties of respiratory cycles that have been considered in this project are: the amplitude of motion cycles, the breathing frequency, and the pattern of cycles.

The amplitude of the liver motion secondary to respiration in normal breathing mode is averagely in the range 10–40 *mm* in superior-inferior (SI) direction, 1–12 *mm* in anterior-posterior (AP) direction, and 1–5 *mm* in medial-lateral (ML) direction. In deep breathing mode, the average range of amplitudes is 30–80 *mm* in SI direction, larger than that of normal breathing mode [21, 8, 56, 5]. The mentioned anatomical directions are in accordance with Figure 1.2 of Chapter 1.

The average human respiration frequency is respectively 12–20 *cycles.min*⁻¹ and 7–8 *cycles.min*⁻¹ for normal and deep breathing. Equivalently, the period of respiratory cycles is 3–5 *sec* and 7–8 *sec*, respectively. Also, the average duration of exhalation in normal breathing mode is 2–4 *sec*, usually longer than inhalation which is 1–2 *sec* [57, 38].

The pattern of the respiratory cycles is shown in Figure 2.1. The upper image represents the tidal volume (airflow volume) over time [13], and the lower image shows the respiratory patterns in SI, AP, and ML directions which are the displacements of infra-red markers on a patient body [8]. The figures indicate that the surface displacement or the tidal volume change smoothly over time, and there is a short pause after each exhalation.

The assumptions and the chosen properties of the respiratory cycles of the phantom are as follows.

- The robotic phantom moves in two directions to mimic the two most dominant motion directions SI and AP. The respiratory motion in the ML direction is negligible comparing to the other two directions [21, 8, 56, 5].

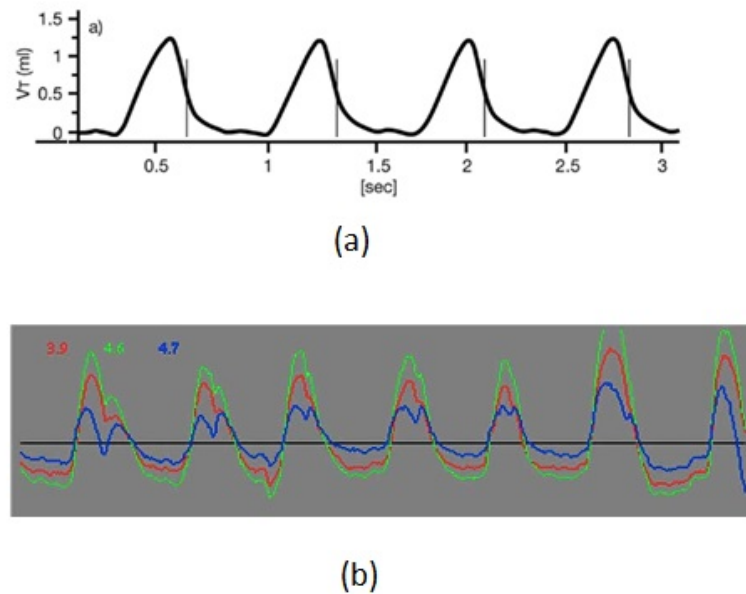


Figure 2.1: The pattern of the respiratory cycles. (a) The tidal volume (V_T) or the volume of the airflow vs. time [13], (b) The respiratory patterns in SI, AP, and ML directions which are the displacements of infra-red markers on patient body [8].

- The breathing type of the phantom is normal.
- No variation or random behavior is included in the phantom motion. The reason is that without variation, the validation of FE model is more straightforward. Once the FEM is created, variations and changes like inter-cycle variations can be added to the model of breathing cycles.
- The amplitude of motion of the phantom in SI direction is 3 cm and in AP direction is 1 cm.
- The breathing frequency is 20 $cycles.min^{-1}$.
- The duration of inhalation and exhalation is respectively 1 sec and 2 sec.

The goal of phantom development is to mimic the above mentioned properties with a smooth and realistic motion of the phantom similar to Figure 2.1.

2.2 Initial phantom design

A prototype of an MR-compatible respiratory motion phantom was designed and created by Paulo Costa [33], a former master student. The phantom was designed such that it moves in two directions SI and AP, the two most dominant respiratory motion directions. Different parts of the phantom are illustrated in Figure 2.2 and can be listed as follows.

- The main structure made of acrylic sheets.
- Four plastic wheels on acrylic rails to guide the phantom motion.
- Three soft actuators made of Agilus 30 by 3D printing. The air is blown into the actuators to move the phantom.
- An external air compressor to provide the required air flow.
- Flexible tubes for the air flow.

- Manual pressure regulators for changing the air pressure and therefore, changing the amplitude of motion to the desired value.
- Two solenoid valves¹ to switch the air flow between the tubes.
- A micro-controller board² to control the air flow via the solenoid valves. The solenoid valves are connected to the digital pins of the Arduino board, and they are switched periodically between "high" and "low" states by the Arduino.

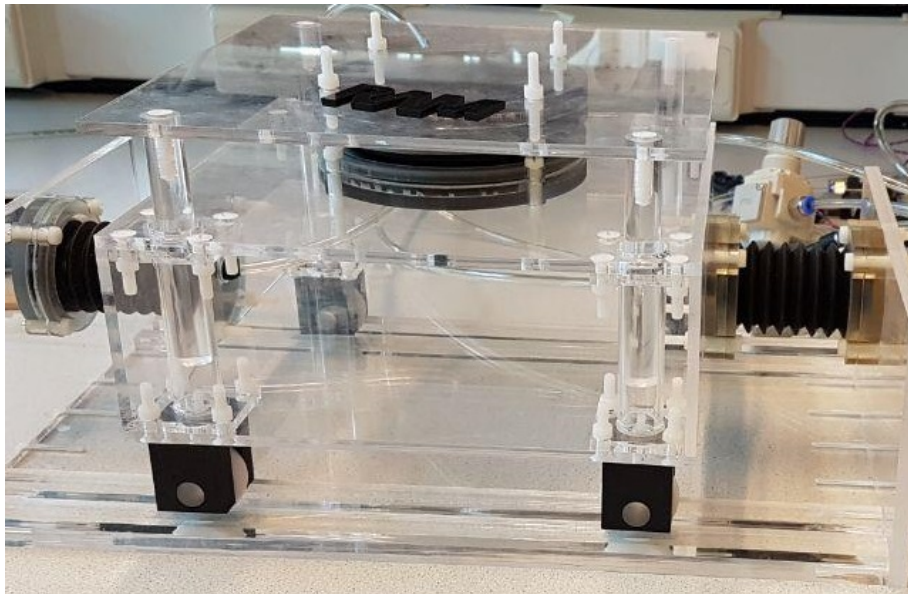


Figure 2.2: The initial phantom prototype designed and created by Paulo Costa [33].

Figure 2.3 shows a diagram of the electrical and mechanical connections of the initial phantom design. As shown in the figure, two of the three actuators are responsible for creating the side motion (or SI-direction motion), and the last one for the up and down motion (or AP-direction motion). An external air compressor provides a constant air flow, which is used to drive the actuators and move the phantom in two directions. The input air flow is divided between two solenoid valves. One valve is connected to the AP-actuator, and the other is connected to the two SI-actuators. The micro-controller changes the openings of the valves with a desired frequency. Via the SI solenoid-valve, the input air flow switches between the right and left actuators, producing leftward and rightward motion respectively (only one of the SI-actuators gets filled by the air flow at a time). In the AP solenoid-valve, one output is closed, and the other is connected to the AP actuator, meaning that when the AP-actuator is switched on, it gets filled by the air and goes up, and when it is off, it goes down due to the gravity.

The phantom motion amplitude can be controlled by changing the pressure of the air flow via the manual regulators, as the motion amplitudes are proportional to the input air pressure. Also, the frequency of motion (or the frequency of the switching action of the solenoid valves) can be changed by means of the micro-controller program³.

2.3 Improvements of phantom design

The first phantom was improved in order to make it possible to measure the liver tumor motion along with surrogate signals.

¹TEMCo PV3211 solenoid valve, Model VC-C1, Temco Industrial

²Arduino UNO, Arduino, Italy

³Arduino IDE

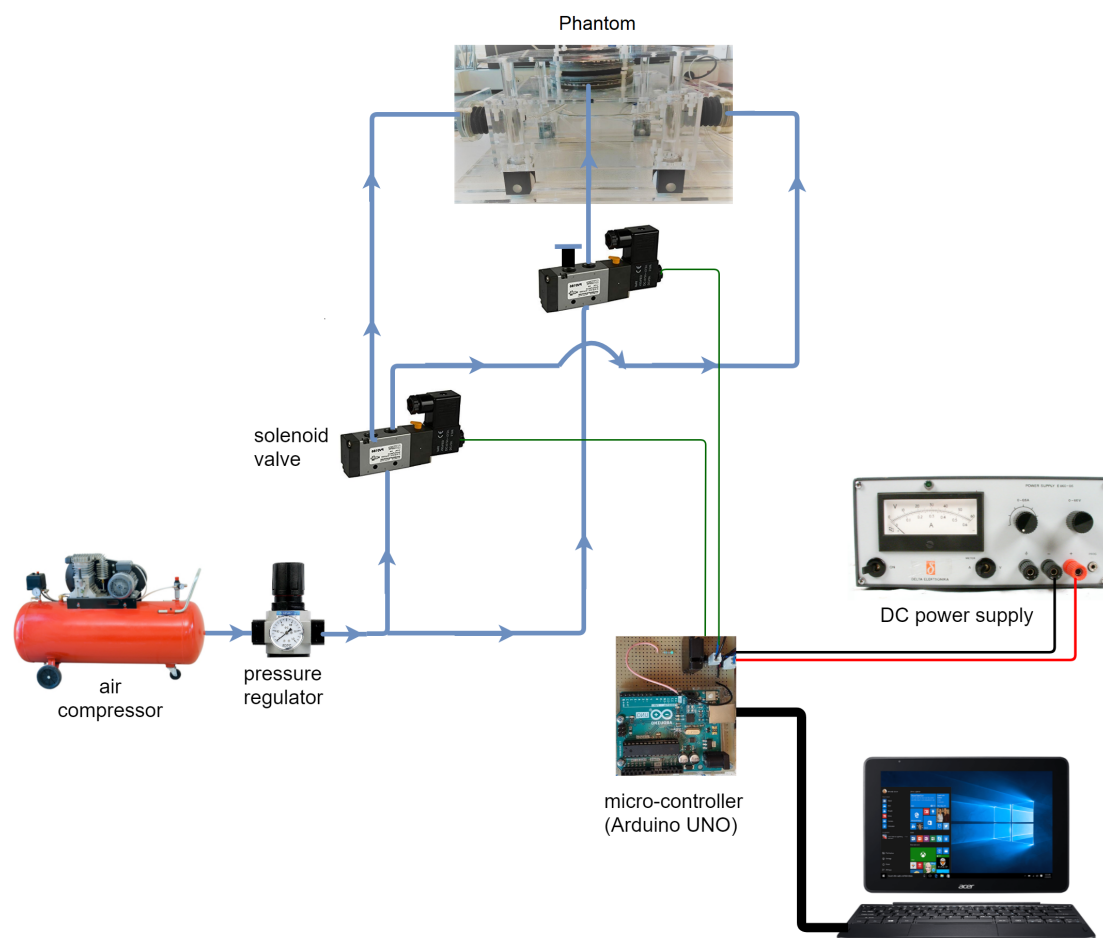


Figure 2.3: The electrical and mechanical connections of the initial phantom design.

2.3.1 Structural improvements

A number of additional parts have been designed, manufactured, and attached to the first prototype to make it a more realistic representation of the hepatic motion. For this purpose, the properties of the liver and tumor tissue and abdomen skin have been derived from the literature (as shown in Figure 1.4 of Chapter 1).

Liver phantom

According to the literature, the elastic modulus (E) of human liver ranges between 8 – 48 kPa and the average value is 20 kPa [55].

One of the frequently used materials for artificial tissues in medical engineering studies is a mixture of gelatin and water due to its easy availability, cheap price, and similarity of its elastic behavior to soft tissues [54].

In a study about needle and gels interactions [53], the elastic moduli of three different mixtures of gelatin and water have been estimated. For the mixtures of 8%, 14.9%, and 20% mass percentages of gelatin to water, the elastic moduli have been reported as 8.7 kPa , 35.5 kPa , and 58.1 kPa , respectively.

In this project, a gelatin⁴ to water mixture of 10% mass percentage has been selected for creating the liver phantom. By interpolation, the corresponding elastic modulus is obtained to be $E = 16.5 kPa$, which is realistic comparing to the real values from the literature.

⁴Dr.Oetker professional gelatin powder

For manufacturing the liver phantom, a liver-shaped mold has been designed by Charlotte Overwijk (former bachelor's student) and 3D printed.

Note that the value of liver elasticity is required for finite element modeling in this project.

Liver tumor

In American Cancer Society [43], it is reported that the liver tumors size in very early stage is smaller than 2 *cm*, in early stage is 2 – 5 *cm*, and in intermediate stage is either larger or more than one tumor. The stiffness of lesions is normally higher than the healthy tissues. According to [58], the value of liver (malignant) lesions module of elasticity is in the range 4.4 – 188 *kPa*. In addition to gelatin, another promising candidate for manufacturing soft tissues is polyvinyl chloride (PVC), because it does not decay after a few days as opposed to gelatin, and its elasticity value can be chosen easily by changing the percentages of the plasticizer and hardener. The tumor has been manufactured of PVC, with the percentages of 35.7% and 64.3% of hardener⁵ and plasticizer⁶, respectively. The elastic modulus of the resulting PVC material is 71.4 *kPa* and it has been calculated by interpolation, according to the information about the elastic moduli of PVC material with different percentages of hardener given in [34]. PVC has been chosen to manufacture the liver tumor, because it is stiffer than the gelatin liver which is similar to the real case. Also, for measuring the tumor motion, an electromagnetic sensor (which will be explained in more details in the next chapter) has been placed inside the tumor. Therefore, the tumor material should not be cracked easily. In this project, the tumor shape is spherical as shown in Figure 2.4-(a) and the shape changes of the tumor have not been considered. The tumor diameter is 4.5 *cm*, which is realistic comparing to the values reported in the literature. Figure 2.4-(b) presents the manufactured gelatin liver containing the PVC tumor.

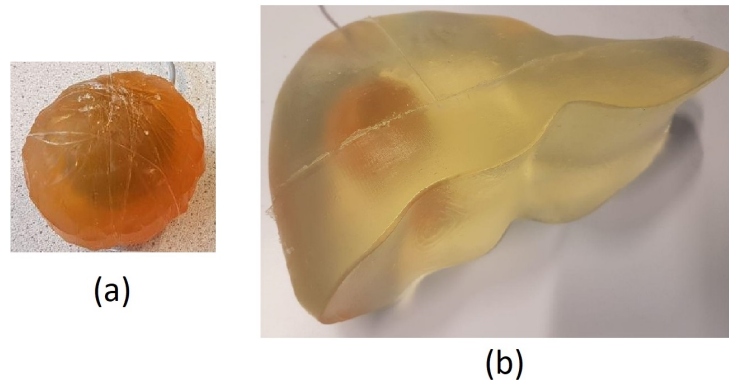


Figure 2.4: Photos of the manufactured tumor and liver phantom. (a) The PVC tumor, (b) The gelatin liver phantom containing the tumor.

Diaphragm, abdomen skin, and grippers

In this project, the diaphragm and abdomen skin are made of latex sheets. Latex produces a tension force similar to the real diaphragm and skin. In order to fix and hold the latex diaphragm and skin, a number of additional parts (grippers) have been designed via computer aided design (CAD) software⁷ as shown in Figure 2.5. The grippers are made of acrylic sheets and hold the latex skin and diaphragm and are attach to the phantom by means of plastic screws and nuts. The completed phantom with the liver and latex parts is shown in Figure 2.6. The latex sheets are moderately tightened. The tension force has not been measured and the amount of tightness has been chosen by trial and error. If the tension is too large, the liver

⁵LUPA hardener, Lureparts.nl

⁶Plastileurre Soft, Bricoleurre, France

⁷SolidWorks

motion will be too small, and if the latex is too loose, the addition of the skin and diaphragm would be pointless and non-realistic.

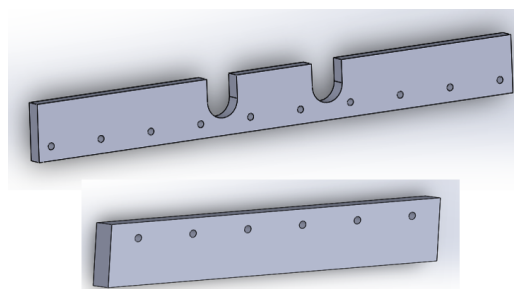


Figure 2.5: Extra parts (grippers) designed in SolidWorks.

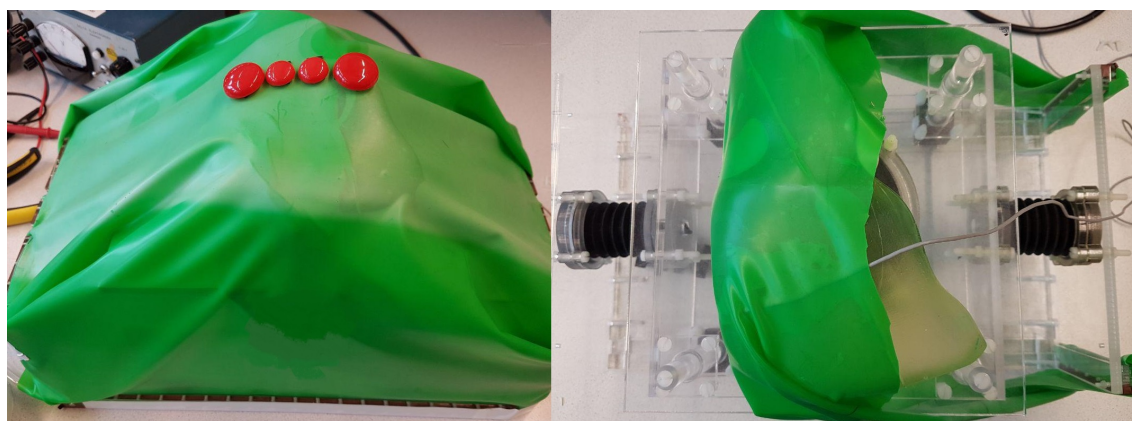


Figure 2.6: Photos of the liver phantom along with the diaphragm (at right) and skin (at left).

Assessment experiment 1

A preliminary experiment was performed on the developed phantom to evaluate its motion. In this experiment an electromagnetic sensor (which will be explained in the next chapter) was placed inside the tumor to measure the phantom displacement in three directions.

Figure 2.7 shows the plot of the first phantom displacement in three directions SI, AP, and ML. Take notice of Figure 1.2 of Chapter 1 for the terms of anatomical directions. The phantom motion was 2-dimensional in AP and SI directions, and the ML direction in the obtained plot is produced by the sensor noise.

Strengths and weaknesses

The phantom design is MR-compatible, meaning that it can be used in MRI sessions and experiments without affecting the quality of the images, e.g. it does not consist of any metal parts. As mentioned, the phantom structure includes the acrylic main body, plastic screws and nuts, Agilus 30 actuators, veroclear actuator plates, and plastic wheels, and it can be used in other projects and experiments with MR imaging.

A disadvantage of this phantom design is that after a few cycles, the polymer actuator which is easily tear-able, gets damaged due to the increase of the air pressure and the air starts to leak out.

Another disadvantage, is that the amplitudes of motion are very small (as shown in Figure 2.7 which shows the phantom motion amplitudes) and not realistic comparing to the average human respiratory motion. The reason is that the actuators cannot stretch completely due to the air leakage and cannot contract completely due to the insufficient exit air flow. Also, the extra

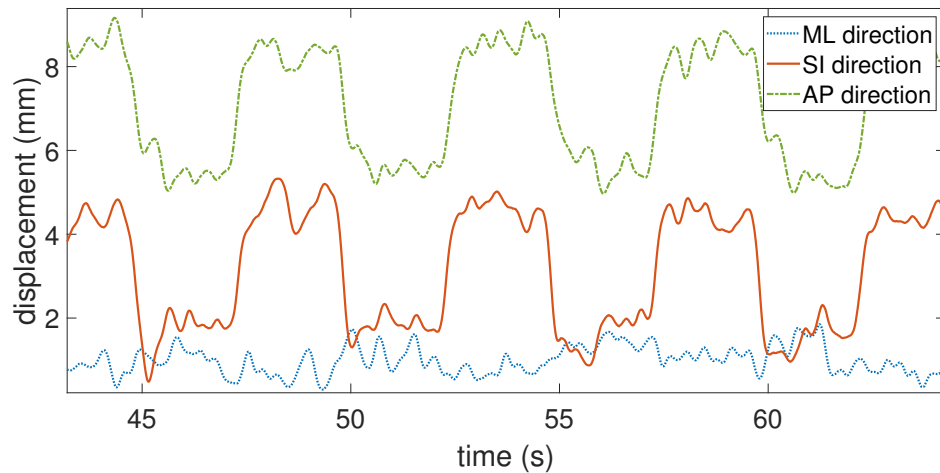


Figure 2.7: The plot of the phantom motion in three directions, obtained from assessment experiment 1.

force exerted by the latex diaphragm tension and the gelatin liver weight prevent the phantom from free movement and make the phantom displacement smaller.

2.3.2 Attaching new actuators

The two SI actuators were replaced by a new design in order to prevent them from tearing and air leakage and to produce larger displacements.

As shown in Figure 1.4 of Chapter 1, for improving the phantom and making it more realistic, some design considerations have been taken into account in the rest of this chapter. For example, the choice of material to manufacture the actuators, or the dimensions of the actuator design, etc.

Manufacturing new actuators

A mold for new actuators for SI motion of the phantom were designed by Nehal Mathur, former bachelor's student [30].

In this project, two SI actuators have been manufactured using the 3D-printed mold and liquid rubber⁸, as shown in Figure 2.8.

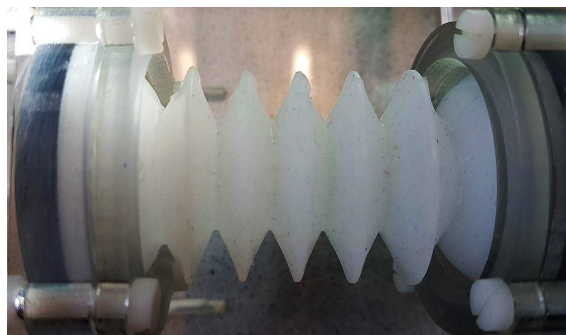


Figure 2.8: The new actuator made of liquid rubber.

The advantages of the new actuators are that they work with lower air pressure (around 0.1 *bar* comparing to 2 *bar* in the previous phantom) with no air leakage.

⁸Ecoflex™ 00-50

New solenoid valves

The solenoid valves implemented in the first prototype (Figure 2.2 and 2.3) have been replaced by new ones⁹, since the new actuators work with a lower air pressure and the previous solenoid valves were not able to work in that low pressure range.

Note that the air flow comes from the compressor at a high pressure for the sake of the AP actuator. However, before the flow goes into the SI actuators, the pressure is decreased by a pressure regulator, since the SI actuators work in a lower pressure range.

Assessment experiment 2

Another preliminary experiment has been conducted to evaluate the new phantom motion, and the resulting plot is given in Figure 2.9. As shown in the plot, the amplitudes of motion are still insufficient and the cycles are not realistic.

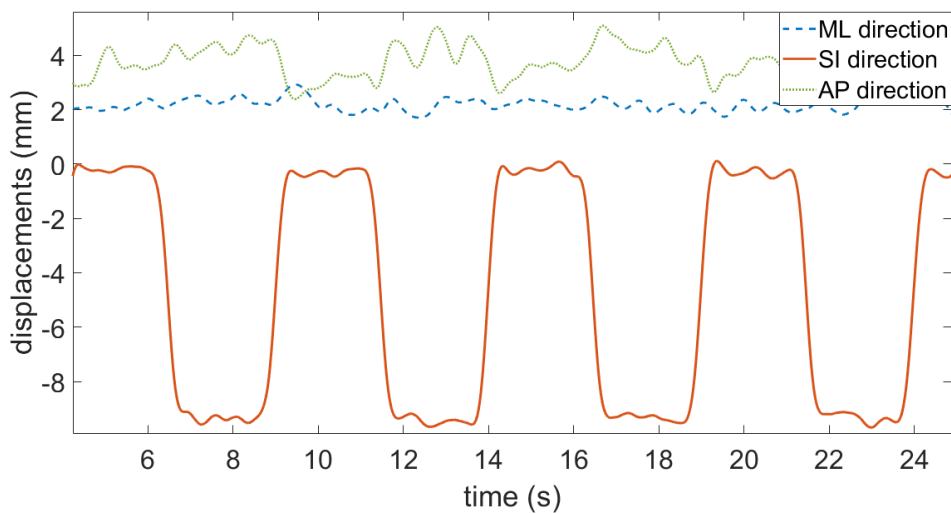


Figure 2.9: The plot of the phantom motion in three directions, obtained from assessment experiment 2.

Strengths and weaknesses

Although the new actuators work with lower air pressure with no air leakage, they suffer from buckling and being overly blown.

They don't have any exit air flow, air leakage, or vacuuming, and the pressure inside the actuators rises continuously and the actuators get overly blown. Also, the actuators buckle during the phantom motion, because the designed length of the actuators is too large. As a result, the amplitudes of motion in SI and AP directions are still small and non-realistic, as shown in Figure 2.9.

2.3.3 Improving the actuators

In order to prevent the actuators from buckling and getting overly blown, they have been improved. The length of the SI actuators have been reduced to prevent them from buckling. Also, they have been wrapped by a strip, which acts as a holder and prevent them from being overly blown as shown in Figure 2.10.

Assessment experiment 3

The third assessment experiment has been conducted to evaluate the improve in the phantom motion. The phantom motion in three directions is presented in Figure 2.11. The plot suggests

⁹MHE2-M1H-3/2G-QS-4 (196134) Solenoid valve, Festo company



Figure 2.10: The improved SI actuator, which is shorter and wrapped by a strip.

that the motion amplitudes are still small. However, they have been improved comparing to Figure 2.9.

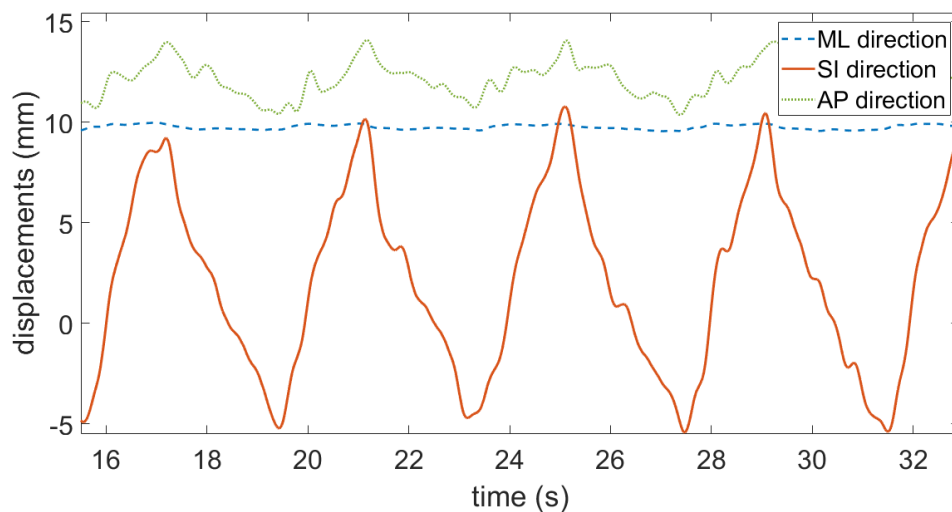


Figure 2.11: The plot of the phantom motion in three directions, obtained from assessment experiment 3.

Strengths and weaknesses

Although the attempts done in this section were effective and they reduce the buckling and blowing behavior of the actuators, there was still no exit way for the air flow. Therefore, in the experiments, an amount of air leakage existed by loosening the tubes connections on purpose (otherwise the actuators would explode due to increasing the pressure).

As a result of not having a vacuum pump and air suction, again the phantom displacements were small and insufficient.

The best solution for managing the exist air flow was installing a vacuum pump, which is explained in the next section.

2.3.4 Installing a vacuum pump

As mentioned above, a vacuum pump was required and implemented for suction of the air out of the actuators in each cycle. In order to implement a vacuum pump into the phantom design, the mechanical connections of the previous phantom (as in figure 2.3) have been changed. Figure 2.12 shows the altered mechanical connections of the phantom and the way of implementing the vacuum pump.

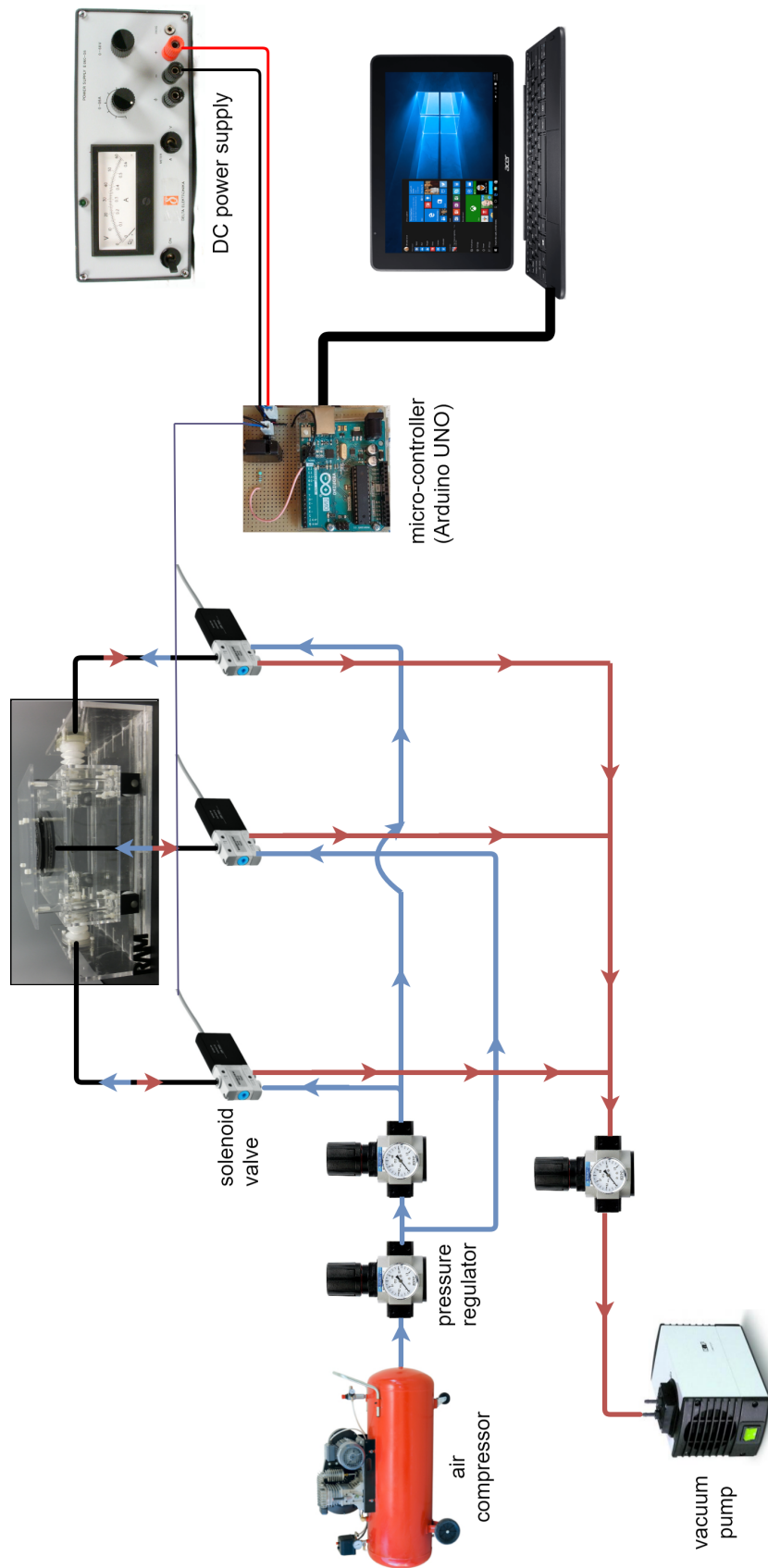


Figure 2.12: The electrical and mechanical connections of the improved phantom.

As Figure 2.12 suggests, each actuator is connected to the output of a solenoid valve, and the solenoid valve is connected to two inputs: the constant air flow of the compressor, and the constant suction of the vacuum pump. When an actuator is in the phase of expansion, the solenoid valve is letting the air flow in. Then, the valve switches to the vacuum pump connection, and as a result, the air is sucked out of the actuator, and the actuator goes back to its initial state.

Note that all three actuators have been connected to the vacuum pump as explained above. The left SI actuator is synchronized with the AP actuator, meaning that their corresponding solenoid valves get connected to the air flow or to the vacuum pump at the same time. The right SI actuator works oppositely to the other two actuators, meaning that when they are connected to the vacuum pump and getting empty, it is connected to the compressor air flow and is getting filled, and vice versa.

Assessment experiment 4

Figure 2.13 shows the improved phantom motion in three directions, having the vacuum pump implemented in the system.

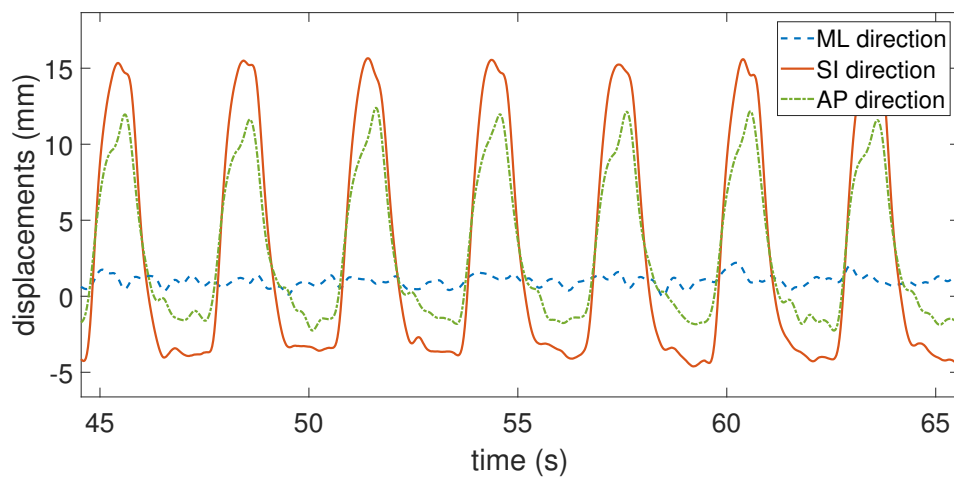


Figure 2.13: The plot of the phantom motion in three directions, obtained from assessment experiment 4.

Strengths and weaknesses

By implementation of a vacuum pump in the system, the previously mentioned problems such as: actuators buckling and getting overly blown was solved.

By sucking the air out of the actuators, the vacuum pump provided a way for air to exit, and as a result, it helped the actuators to contract completely.

It results in a larger displacement as well, because in the previous phantom, the actuators were not able to reach their initial state and contract completely.

The dis-advantage is that the phantom motion is still not smooth and the pattern of the cycles is not realistic enough (comparing to Figure 2.1), since the actuators have an on-off motion due to the switching of the solenoid valves.

2.3.5 Installing digital regulator for motion correction

In order to have a smooth and more realistic phantom motion, it was required to change the input pressure gradually instead of the rapid on-off motion. For this purpose, a digital pressure regulator was implemented to the system as explained in the next section.

Figure 2.14 represents a diagram of the electrical and mechanical connections of the final improved phantom with a digital pressure regulator to control the input pressure.

As shown in the figure, the mechanical connection is similar to Figure 2.12, and the only difference is that now, the input pressure of two SI actuators is the output pressure of the digital regulator. The digital regulator and the AP actuator input pressure come from the compressor. It means that the AP actuator is controlled in the same way as the previous phantom (with the vacuum pump and on-off motion), while two SI actuators' input pressures are now provided and controlled by the digital regulator.

The changes in electrical connection are that now the digital regulator is connected to a power supply, as well as the analogue pins of the micro-controller board (Arduino UNO). The output pressure of the digital regulator is changed gradually and periodically by the Arduino program. The solenoid valves are still connected to the digital pins as before, and they are switched between "high" and "low" states, so that the actuators get activated ex-changeably.

Programming the new phantom motion

In this project, a new algorithm has been implemented in Arduino for controlling the phantom motion smoothly and the code is presented in Appendix A.

As mentioned before, the digital regulator is connected to the analogue pins of the Arduino board, which means that the output pressure can take any desired value (instead of binary outputs "high" or "low").

The left SI actuator expansion corresponds to inhalation, while the right SI actuator expansion corresponds to exhalation. According to Figure 2.1, the duration of the inhalation is shorter than exhalation, and it was taken into account in programming the phantom motion.

Assessment experiment 5

Figure 2.15 shows the result of the assessment experiment with the final improved phantom.

The expansion of the right actuator (equivalently exhalation) is programmed to be done in different velocities in order to reach a pattern more similar to the real case in Figure 2.1.

Strengths and weaknesses

The final phantom design is successfully showing a smooth motion which is more realistic (comparing to Figure 2.1). The frequency of cycles, the duration of inhalation and exhalation, and the amplitudes of motion have been carefully taken care of.

A dis-advantage of the final improved phantom is that the AP actuator has not been controlled by a digital regulator as opposed to the SI actuators. The reason is that the AP actuator is made of Agilus30 material by 3D printing, while the SI actuators are made of liquid rubber as mentioned in the previous sections and as a result, it works in a noticeably higher pressure ranges. Since the period of each cycle is approximately 3 *sec* and the digital pressure regulator has some amount of delay, it doesn't have enough time to reach the high pressure required by the AP actuator. Therefore, if the AP actuator gets connected to the digital regulator as well, it will have insufficient displacement, due to the lack of time to increase the pressure sufficiently. Also, it is a good practice to control it in the previous on-off mode in order to compare the resulting motion with those of the newly-controlled SI actuators.

Another dis-advantage of the final improved phantom is that while the input air flow of the SI actuators is controlled by the digital regulator and altered gradually, the vacuum pump pressure is constant. A further improvement is recommended by adding a digital pressure regulator to the vacuum pump as well. However, as shown in Figure 2.15, the resulting respiratory patterns of the phantom is sufficiently realistic.

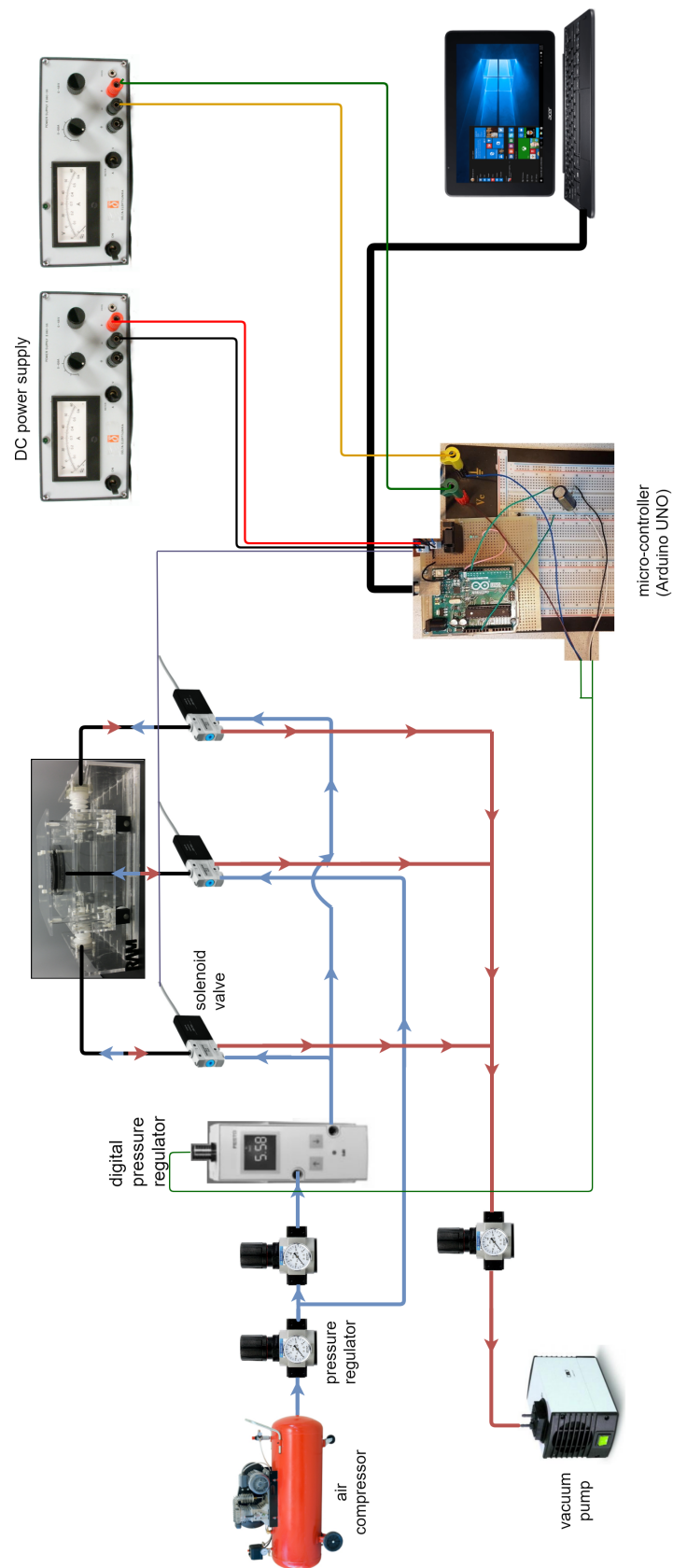


Figure 2.14: The electrical and mechanical connections of the final improved phantom.

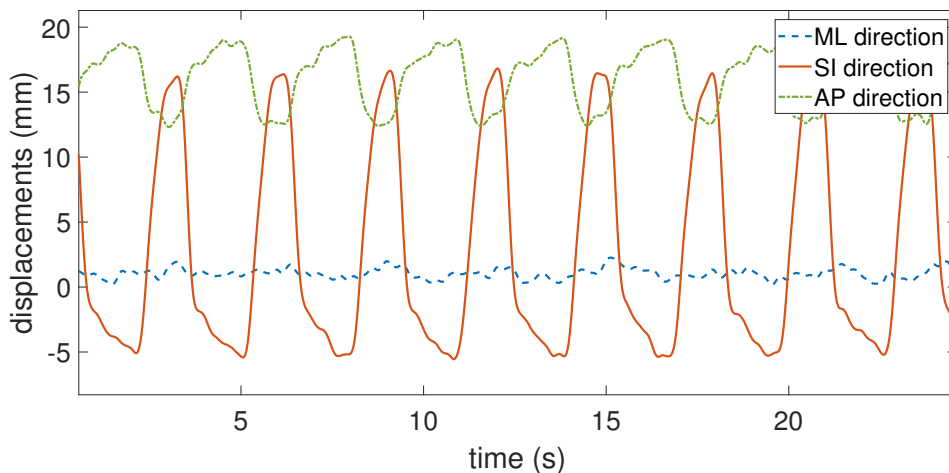


Figure 2.15: The plot of the phantom motion in three directions, obtained from assessment experiment 5.

2.4 MR-compatibility test

As mentioned earlier, all phantom parts are MR-compatible, except the electrical devices and connections. One way to use the liver phantom in a MRI room is to use long air tubes, such that all electrical parts are laid outside of the MRI room, and only the main phantom structure (along with the gelatin liver and latex tissues) remain in the room.

However, using very long air tubes could be challenging, because it leads to drop in pressure, as well as delays in the air flow. Therefore, it is necessary to check whether the phantom works well with long air tubes. A number of experiments (MR-compatibility tests) have been performed to check this.

In this experiment, the three air tubes that are attached to the actuators (the black lines in Figure 2.14) were replaced by three long tubes. Each of the long tubes was 6 m long, which is enough to put the phantom inside an MRI room, separately from the rest of the system.

Figure 2.16 shows the plots that are obtained from three experiments. The top plot is obtained from an experiment with initial short tubes and input pressure of 2 bar, the middle plot shows the same conditions with long tubes, and the bottom plot presents the results with the same long tubes, but with input pressure of 4 bar.

As it is observable from the plots (a) and (b) in Figure 2.16, the phantom amplitudes of motion in respectively SI and AP directions are around 20 and 5 mm with short tubes. However, the mentioned values are respectively about 12 and 2 mm with long tubes. It means that with longer tubes, the air leakage (pressure loss) from the connections increases and as a result, the phantom motion amplitudes decreases.

By comparing the plots (a) and (c) in Figure 2.16, it is clear that the phantom has approximately equal motion amplitudes; however, the input pressure is larger in the case with longer tubes. It means that in order to compensate the increased amount of pressure loss in the connections and to have the same motion amplitudes, it has been necessary to increase the input pressure.

Therefore, by increasing the input pressure, the phantom is still effectively working with 6 m long tubes, which means that it is feasible to use the phantom inside of an MRI room while keeping the electrical devices outside of the room.

2.5 Summary and important notes

In this project, a previously designed and manufactured respiratory motion phantom (Figures 2.2 and 2.3) has been improved and upgraded to make it a usable liver motion phantom for the experiments.

The final improved phantom can be observed in Figures 2.6 and 2.14 with the following notes and recommendations.

- The final improved phantom is a physical model of liver and liver tumor respiratory motion. The main parts are: phantom structure, liver and tumor, diaphragm and skin, compressor, vacuum pump, digital regulator, solenoid valves, and an Arduino board.
- The resulting phantom motion is sufficiently realistic (by comparing Figures 2.1 and 2.15) in terms of the motion amplitude, breathing frequency, the pattern, and smoothness of the motion.
- It is MR-compatible, provided that long tubes of length 6 *m* are used.
- The motion is controlled by a digital pressure regulator. The regulator has a built-in controller, and is able to follow any given path for the pressure. It means that any desired cycle pattern can be created by programming the digital regulator. Especially, random variations can be added to the phantom motion in order to model the inter- and intra-cycle respiratory variations. In this project, variations have not been added to the phantom motion, because as it will be discussed in the next chapters, the cycles should be variation-free for the sake of validating the finite element model.
- In future works, it would be favorable to change the AP actuator similar to SI actuators by 3D-printing a mold. In that case, the AP actuator can be connected to the digital regulator as well and its motion can be improved. (Currently, due to the difference the SI and AP actuators in the material and therefore the working pressure range, the AP actuator is still working in the on-off mode and not smoothly).
- It would be beneficial to attach the vacuum pump to a digital regulator as well in order to change the amount of air suction smoothly.

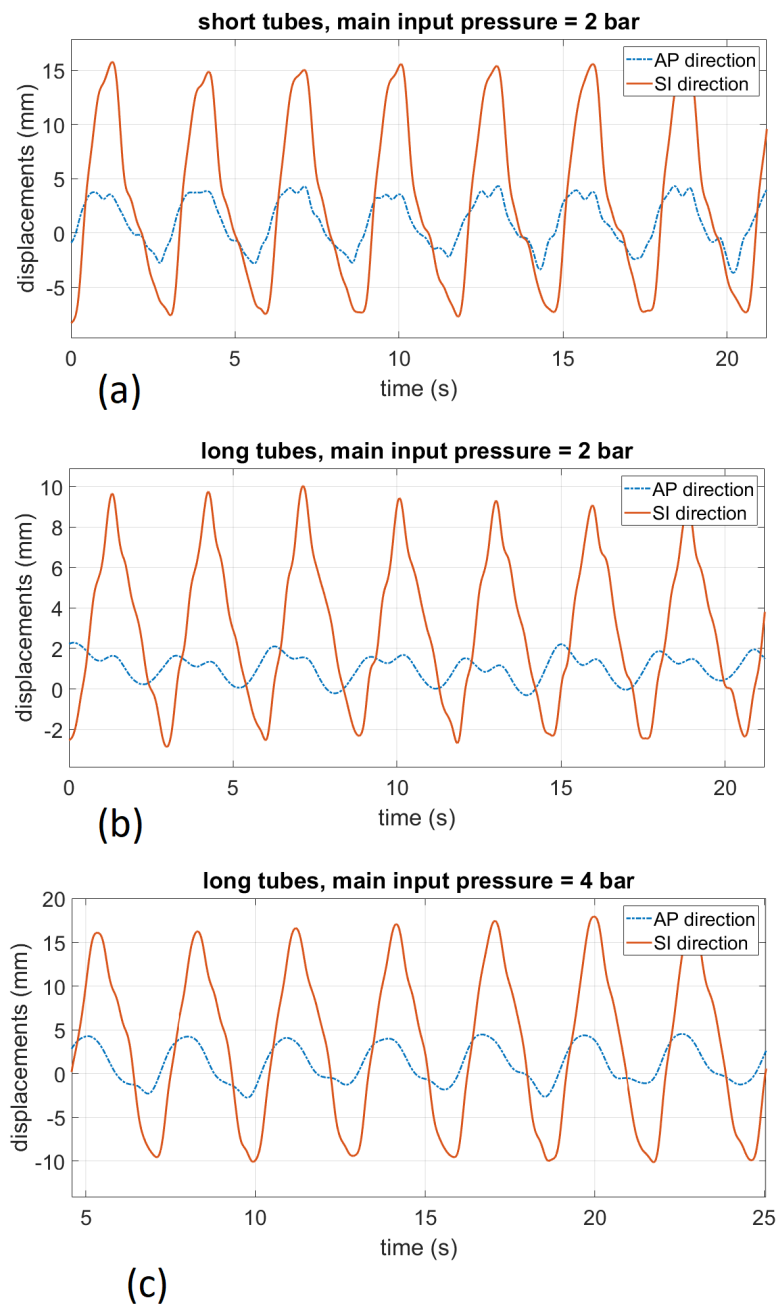


Figure 2.16: The plot of the phantom motion in two directions, obtained from MR-compatibility test. (a) Experiment with short tubes and 2 bar main input pressure, (b) Experiment with long tubes and 2 bar main input pressure, and (c) Experiment with long tubes and 4 bar main input pressure.

3 Sensors and experimental setup

In this chapter, the types of sensors for measuring surrogate signals and the motion of interest that are mostly used in similar works are explained. Then, the chosen set of surrogates and sensors for this project are described, as well as the experimental setup. Next, the experimental data post-processing is explained. The chapter ends with a discussion about the finite element model and its contribution to this project.

3.1 Motion of interest and surrogate signals in similar works

As mentioned in Chapter 1, the liver tumor motion will be estimated from the surrogate signals in this work.

One of the requirements of the surrogate signals is that they should be highly correlated with the motion of interest. Also, they should have an updating frequency higher than that of the respiratory cycles in order to capture the breathing patterns [25, 29]. To have more clinically applicable results, the surrogate signals should be measured at high updating frequencies to approximate a real-time estimation model.

In Chapter 1, Table 1.1, a list of the types of surrogates that have been mostly used in the literature is given.

As it is observed in the table, one of the most common surrogates is spirometry, which is based on the measurement of the respiration air volume. The surrogates obtained from spirometry are highly correlated with the motion of interest; however, there is always air leakage which produces inaccuracies [25].

Another type of surrogate signals that is very common and can be seen in Table 1.1 of Chapter 1 is the displacement of external markers placed on the abdomen or chest skin which can be measured by different devices: by infrared emitters and receivers, by imaging modalities such as MRI, CT, or fluoroscopy, and by digital camera.

In one of the studies, optical markers were placed on patients abdominal skin and their motion was recorded by a digital camera. Simultaneously, MR images were taken from the patients abdomen. After MR image segmentation and extracting the motion of interest from the images, the markers displacements were correlated to the motion of interest. It is concluded from their study that markers displacements have the advantage of having a high correlation with the motion of interest [25].

In another study, an IMU (inertial measurement units) has been utilized to measure the angles of deflection of a needle which was inserted into a liver phantom and the angles had a high correlation with the point of interest motion [29].

The displacement of optical markers obtained from digital camera as well as IMU output signals are two types of commonly used surrogates which are easily available and highly correlated with the internal organs motion as mentioned above. In Table 1.1 of Chapter 1, it is observable that external markers are very common in similar works, while IMU has gained less attention. One of the aims of this project is to compare the commonly used surrogate signal (markers displacement) with a less common one (IMU signals).

In this study, both optical markers and IMU are employed in order to make a comparison between the accuracy of the models and determine which surrogates result in a more accurate motion estimation model. It is one of the goals of this project and is also mentioned in Section 1.5 of Chapter 1.

In Table 1.1 of Chapter 1, there is also a list of the mostly used sensors for measuring the motion of interest in the literature. A number of most common techniques for measurement of the

motion of interest are: electromagnetic (EM) tracker and imaging modalities such as MRI, CT, and fluoroscopy.

One of the differences between imaging modalities and EM tracker is that the frequency of obtaining the images is not high enough for real-time applications comparing to EM trackers, meaning that the motion of interest cannot be estimated at a sufficiently high updating rate. Also, EM tracker gives the exact position of the region of interest without the need for image segmentation. There exists imaging modalities that capture the motion of the region of interest in real-time such as ultrasound. However, ultrasound cannot always provide exact information about the position of the region of interest and also it cannot pass through the bones. It means that in some cases, ultrasound is not able to detect and track the objects.

3.2 Sensors and experimental setup

In this project, two different sensors have been used to measure surrogate signals: external markers with a digital camera, and an IMU (inertial measurement unit) attached to the hub of a needle which is inserted in the phantom. Also, for measuring the liver tumor motion, an electromagnetic sensor (EM tracker) has been implemented.

3.2.1 External markers and digital camera

In order to capture the displacements of all points of the abdomen skin, four markers have been placed on the latex skin such that they have different SI and AP locations and cover the complete width of the liver, as shown in Figure 3.1-(a).

A digital camera¹ with 30 fps recording frame rate has been used in the experiments of this report, along with MATLAB Image Acquisition Toolbox. As it is presented in Figure 3.1-(b), the latex skin motion which is in the plane SI-AP is recorded by the camera placed at a specific distance from the plane of motion.

For converting the unit of the markers motion in the video from pixels to the real millimeters unit, a calibrated paper is held in the plane of markers motion during the experiments by a gripper, as shown in Figure 3.1-(b).

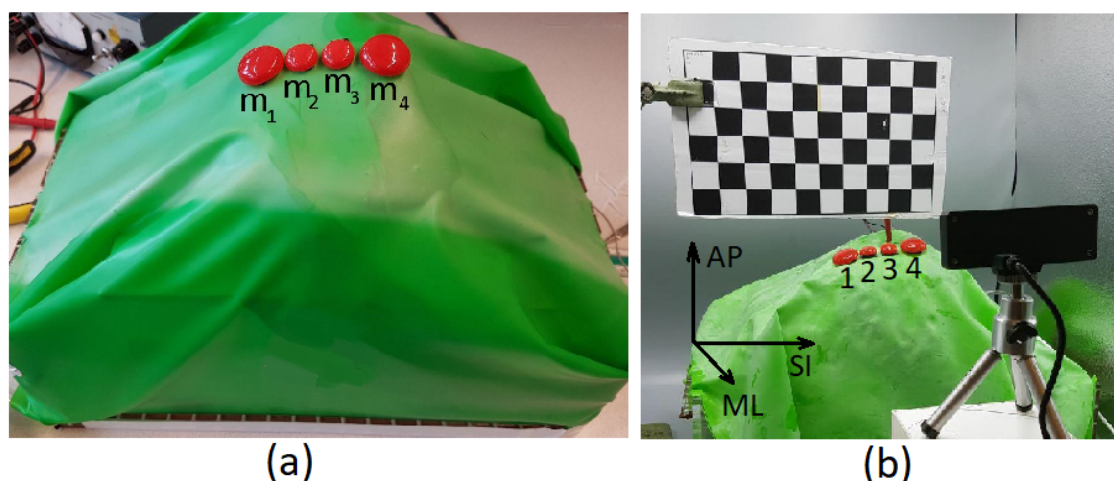


Figure 3.1: The external markers attached to the phantom along with the digital camera. (a) Four markers, named m_1 to m_4 , laying on the liver, and (b) The setup of the digital camera and calibrated paper which is held in the markers' plane of motion, as well as the phantom coordinates system ML-SI-AP.

¹Logitech C920 PRO HD Webcam

3.2.2 Inertial measurement unit (IMU)

In this project, an IMU² was attached to the hub of a plastic needle, and the needle is inserted into the liver phantom and latex skin as shown in Figure 3.2. This sensor has 9DOF: a triaxial 14-bit accelerometer, a triaxial 16-bit gyroscope, and a triaxial geomagnetic sensor. More detailed descriptions are given in [42]. It is small (of dimensions $5.2 \times 3.8 \times 1.1 \text{ mm}^3$) and lightweight enough for this project. Its output signals relevant to this work are linear accelerations, angular rates, and absolute orientation expressed in Euler angles (or quaternions) at updating rate of up to 100 Hz .



Figure 3.2: The IMU (at the top-right of the figure) is attached to a plastic needle which is inserted in the latex skin and liver phantom.

The IMU is connected to the analogue pins of a micro-controller board³, and the board is programmed to collect the data via the IMU. The data are written to the serial ports of a computer, and then they are logged and saved by another programming language software, named Processing.

During the experiments, the deflection angles of the needle as well as its angular rates and linear accelerations are measured by IMU in order to generate surrogate signals.

3.2.3 Electromagnetic (EM) tracker

The tumor motion is measured by an electromagnetic (EM) sensor⁴, inserted into the tumor (the wired sensor in Figure 2.4 of Chapter 2).

The position data of the tumor in three directions is measured by the EM tracker at updating rate of 40 Hz during each experiment, while at the same time, the IMU and digital camera are measuring and recording surrogate signals.

3.2.4 Experimental setup and procedures

The experimental setup consists of: the improved final version of the phantom (described in Chapter 2), the IMU attached to a needle, external markers, digital camera, calibrated paper, and EM tracker as mentioned in the previous section.

The duration of the experiment was 100 s , with about 30 respiratory cycles. The amplitude and frequency of the phantom motion is given in Section 2.1 of Chapter 2.

²BNO055, Bosch Sensortec, Germany

³Arduino UNO, Arduino, Italy

⁴NDI medical Aurora, 6DOF Reference, 25 mm Disc, Part Number: 610066, Northern Digital Inc., Canada

3.3 Data post-processing

After the experiment, the data which were obtained from different devices were processed. Different post-processing steps have been operated on the data and will be explained in this section: image segmentation for obtaining the markers displacements, change of coordinates systems for the IMU data, removing outliers, filtering and smoothing, and synchronization.

3.3.1 Image segmentation and markers tracking

A MATLAB script has been written using the idea given in MathWorks [47] for image segmentation based on color thresholds, in order to segment the markers and obtain their displacements from the recorded video. The complete code is presented in Appendix B, and the steps are explained in this section. Also, the resulting images after each step are shown in Figure 3.3.

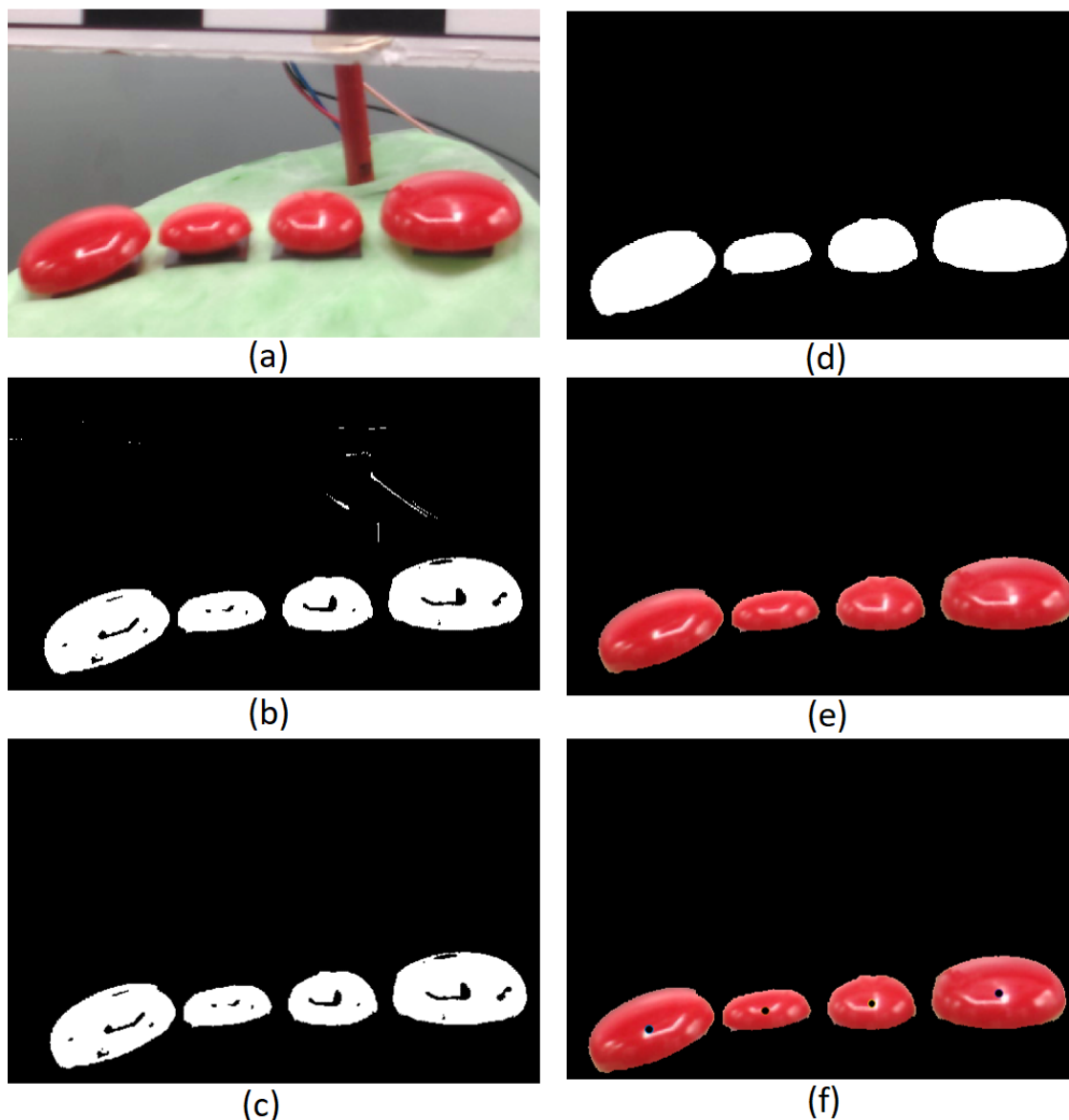


Figure 3.3: The steps of color segmentation for tracking the markers: (a) the original image before segmentation, (b) the resulting image after segmentation based on color thresholds, (c) the result after removing the small objects, (d) after closing the borders and filling the holes, (e) after putting back the colors, and (f) the final segmented image along with the centers of all markers.

First, the color high- and low-thresholds of the markers are defined, which are dependent on each experiment conditions, such as the ambient light intensities, etc. For each experiment, the color thresholds are changed manually by inspecting the RGB values of the pixels. Since the markers are red, the red color thresholds are higher than green and blue.

```
1 %Color high- and low-thresholds
2 redThresholdLow = 160;
3 redThresholdHigh = 260;
4 greenThresholdLow = 20;
5 greenThresholdHigh = 140;
6 blueThresholdLow = 30;
7 blueThresholdHigh =140;
```

Then, the video is read frame by frame. Each frame is an image that is to be segmented as shown in Figure 3.3-(a). For that, the RGB channels are defined:

```
1 video = VideoReader('v.avi'); %Reading the recorded video
2 n = 1;
3
4 while hasFrame(video)
5     image = readFrame(video); %Reading the recorded video
        frame by frame
6
7     redChannel = image(:, :, 1); %Defining the RGB channels
8     greenChannel = image(:, :, 2);
9     blueChannel = image(:, :, 3);
```

Next, the RGB masks are defined and the image is segmented based on the color thresholds:

```
1 %RGB masks: color segmentation based on the thresholds
2 redMask = (redChannel >= redThresholdLow) & (redChannel
        <= redThresholdHigh);
3 greenMask = (greenChannel >= greenThresholdLow) & (
        greenChannel <= greenThresholdHigh);
4 blueMask = (blueChannel >= blueThresholdLow) & (
        blueChannel <= blueThresholdHigh);
5
6 img =(redMask & greenMask & blueMask); %The segmented
        image
```

The image that is obtained at this step is shown in Figure 3.3-(b). Then, the MATLAB function `bwareaopen` is employed to remove the small objects. The resulting image after removing the small objects is represented in Figure 3.3-(c).

```
1 smallestAcceptableArea = 500;
2 img=bwareaopen(img, smallestAcceptableArea); %Removing
        the small objects
```

After that, with the help of `imclose` and `imfill` functions, the borders of the markers are closed, and the holes are filled. The resulting image is shown in Figure 3.3-(d).

```
1 structuringElement = strel('disk',1);
2 img = imclose(img, structuringElement); % Smooth the
        borders
```

```

3
4 img = imfill(img, 'holes'); % Fill in any holes

```

Next, an RGB image of the segmented markers is formed in order to put the colors back on the image. The result is represented in Figure 3.3-(e).

```

1 Mask1 = cast(img, class(redChannel));
2 maskedImageR = Mask1 .* redChannel;
3 maskedImageG = Mask1 .* greenChannel;
4 maskedImageB = Mask1 .* blueChannel;
5
6 maskedRGBImage = cat(3, maskedImageR, maskedImageG,
    maskedImageB);

```

Then, the location of the center of each marker is derived (based on the number of pixels) using `regionprops` command for each frame. The centers locations are saved in an array and are shown in Figure 3.3-(f).

```

1 stats = regionprops(img, 'centroid'); %Finding the center
    of each marker
2 loc = cat(1, stats.Centroid);
3 m1x(n)=loc(1,1); m1y(n)=loc(1,2);
4 m2x(n)=loc(2,1); m2y(n)=loc(2,2);
5 m3x(n)=loc(3,1); m3y(n)=loc(3,2);
6 m4x(n)=loc(4,1); m4y(n)=loc(4,2);

```

After that, the segmented image is saved. Also, the time stamps are stored in an array in order to have the locations of the markers as a function of time.

```

1 imwrite(img, fullname) %Save the segmented image
2 n = n+1;
3 end %end of while loop
4
5 t=(1/Video.FrameRate):(1/Video.FrameRate):Video.Duration;
    %Saving the time stamps as a time array

```

Finally, using the image of the calibrated paper, the number of pixels which are equivalent to one millimeter are calculated. Then the obtained markers displacements are converted from pixel scales to millimeters. Also, the markers motion are converted from the image's X-Y coordinates to the phantom SI-AP coordinates. Take notice of Figure 3.1-(b) for the phantom coordinates system ML-SI-AP.

```

1 % converting pixels to millimeter as well as converting
    from image X-Y coordinates to phantom SI-AP coordinates
2 n=25/106.5; %Coefficient of conversion
3
4 m1_SI= m1x*n; m1_AP= -m1y*n;
5 m2_SI= m2x*n; m2_AP= -m2y*n;
6 m3_SI= m3x*n; m3_AP= -m3y*n;
7 m4_SI= m4x*n; m4_AP= -m4y*n;

```

3.3.2 Suggestions about image segmentation

The image segmentation code in the previous section has successfully worked in this project and the displacements of the markers centers have been tracked well. However, a limitation of this code is that it is sensitive to the ambient lights, since the light changes the RGB values. Therefore, for each experiment, the values of thresholds have been chosen separately and manually.

In order to improve the image segmentation code and make it more robust to the ambient changes, it is suggested to use HSV (hue, saturation, value) representation of the colored images instead of RGB. In this case, H (hue) is constant, because it corresponds to the color only. However, S (saturation) and V (value) are variant and depend on the ambient conditions such as the light. It is possible to write the segmentation code and separate the colors based on the hue, instead of RGB channels and defining the thresholds. This way, the color segmentation code will be more robust to the ambient changes. Also, it will not be necessary to change the RGB thresholds manually for every time of experiment, and instead, the hue can be chosen automatically.

3.3.3 Change of coordinates

The IMU measures the data with respect to an inertial coordinates system. It is necessary to transform the data expression from the inertial coordinates to the phantom coordinates in order to have a more comprehensible data.

Before the experiment, the null position of the IMU at which all Euler angles are zero is determined and recorded, which corresponds to the inertial coordinates.

After the experiment, the signals which are expressed in the inertial coordinates are converted to the phantom ML-SI-AP coordinates, knowing the constant angles between the mentioned two coordinates.

Note that markers displacements are converted to SI-AP coordinates as mentioned in the last section. Also, the EM tracker's output signals are expressed in an inertial coordinate parallel to that of the phantom and is easily converted to the phantom coordinates.

3.3.4 Removing outliers

The outliers (if observed) of the experiment signals are removed using the MATLAB command `isoutlier`.

3.3.5 Filtering and smoothing

Since all data contain a specific amount of noise, it is necessary to smooth the data by a low-pass filter. For selection of the cut-off frequency of the low-pass filter, the breathing frequency of the phantom should be taken into account to avoid filtering important information. It means that the cut-off frequency should be high enough comparing to the respiration frequency.

Also, it should be noted that the amplitude of high-frequency oscillations should be small comparing to the main amplitude of motion; otherwise, smoothing the oscillations would reduce the accuracy. In the experiment, the accuracy of the sensors was high enough so that the amplitudes of the high-frequency oscillations were very small comparing to the main motion.

3.3.6 Synchronization

Since the signals have been collected from different devices and computers, it is necessary to perform data synchronization after the experiment. The synchronization has been performed in two steps: aligning the starting and ending times of the signals and signals re-sampling to obtain equal sample times.

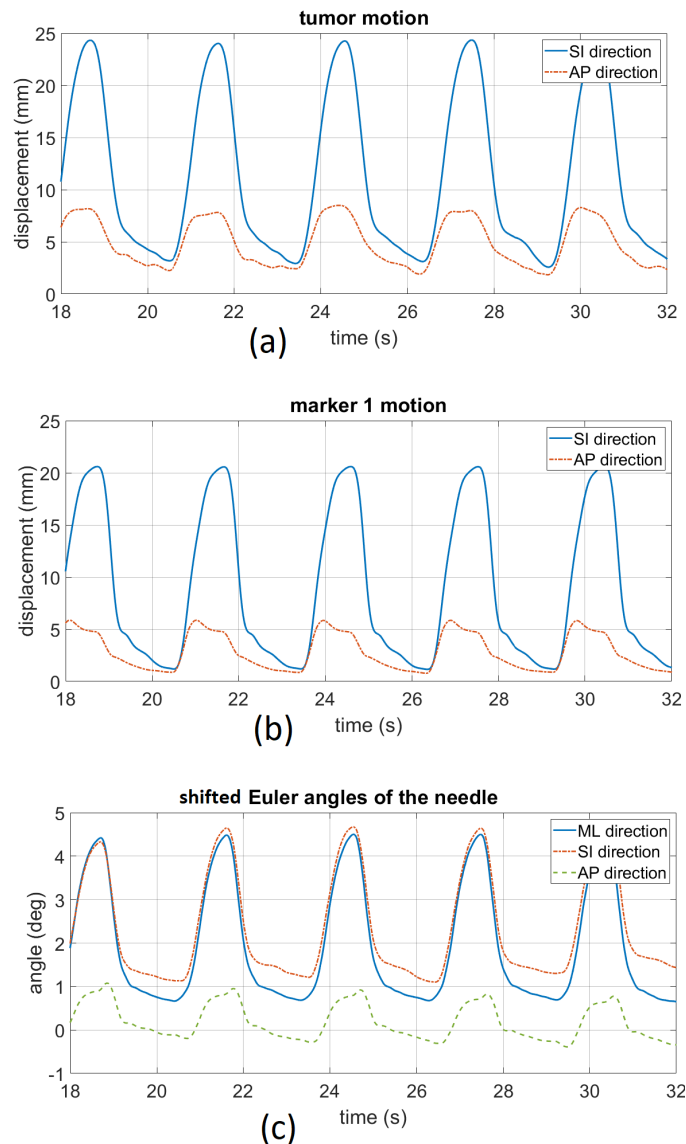


Figure 3.4: The final processed data from the experiment. (a) The tumor motion in SI and AP directions, (b) the marker 1 motion in SI and AP directions, and (c) the deflection angles of the needle (shifted through the vertical axis).

The start and ending points of the signals have been equalized by aligning the last peaks of the signals. Note that during the experiment, all the sensors data logging were terminated in such a way that the ending times of the signals do not differ more than one complete cycle. It means that the last peak of all signals occurred at the same time.

Also, since the sampling rates of the sensors are different, a re-sampling has been performed by interpolation in order to equalize the sampling time of the signals.

Figure 3.4 presents the final processed signals obtained from the sensors plotted against time. Figures a, b, and c show respectively the signal of the tumor motion in SI and AP directions, the first marker motion in SI and AP directions, and the angles of deflection of the needle with respect to the phantom ML-SI-AP coordinates. Note that the motion plots of other markers are similar to that of the marker 1 and are not repeated here.

3.4 Finite element model

In the experiment, the geometrical properties such as the location of the markers, the location of the liver in the setup, the location of the IMU needle in the liver, the location of the tumor inside the liver, etc. as well as other properties such as the input flow and vacuum pump pressure were recorded for the sake of the finite element modeling.

The FE modeling has been performed by one of this project's supervisors (Hamid Naghibi Beidokhti M.Sc) with a FE analysis software (Abaqus FEA).

A view of the created FE model of the experimental setup is shown in Figure 3.5.

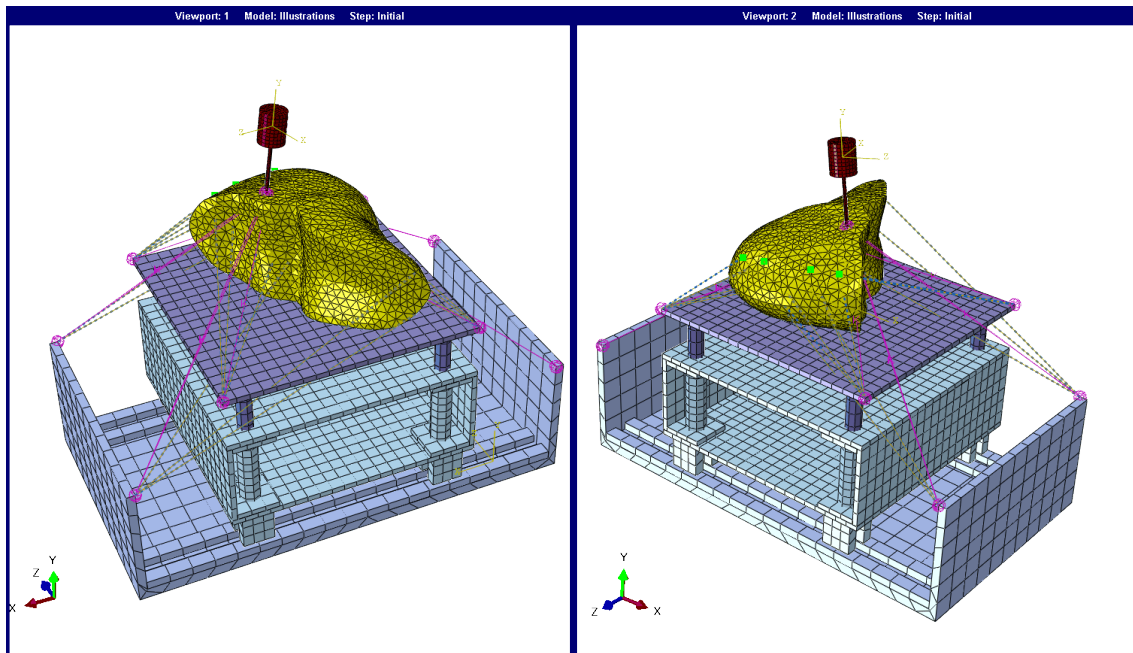


Figure 3.5: A view of the created finite element model of the experimental setup.

The contribution of the FE model in this project is that it models the experimental setup and makes it possible to repeat the experiment for different values of the constant parameters mentioned in the previous chapters. It means that, instead of repeating the experiment with different values of parameters to obtain more data sets for training, the phantom motion and the experiment is simulated by FEM, and more sets of data will be generated by the FE model for different values of the parameters. Then, the effect of changing the parameters on the motion as well as on the learning-based estimation accuracy will be analyzed.

The reason to choose FEM to generate more data sets instead of repeating the experiment is mainly that it is not possible to change only one desired parameter while fixing accurately the rest of the parameters. For example, it is not possible to repeat the experiment with a different tumor size, while keeping the values of the latex tension force, the displacements, the sensors positions, etc. exactly the same, meaning that the repeat-ability of the experiment is low.

3.5 Summary

In this chapter, it was discussed why external markers and IMU signals have been chosen as surrogate signals, which will be used as the inputs of the learning algorithm.

Also, the experimental setup was shown as well as how the surrogates and the tumor motion are measured.

Then, it was explained how the data obtained from the experiment are post-processed and put together for the learning algorithms and motion estimation.

Finally, it is argued how FEM helps to the flow of this project by generating more data sets for different values of the concerned parameters in order to use then in learning algorithms and analyze the effect of the parameters on the motion and on the estimation accuracy.

4 Supervised-learning results from the experimental data

In this chapter, two data sets which have been obtained from two experiments (one with random variations and the other without variations) are post-processed as mentioned in the previous chapter. Then, the data sets are analyzed in order to choose suitable learning algorithms. Next, it is explained how the mathematical learning-based model for the respiratory motion estimation is obtained using the chosen algorithms. Following that, the results of the motion estimation are presented. This chapter ends with comparisons between the performances of different algorithms as well as between the contributions of surrogate signals to the motion estimation accuracy, which is the answer to one of the research questions in Chapter 1.

4.1 Experimental data

In this chapter, two experiments have been performed to generate the required input and output data sets. One experiment was performed as described in the previous chapter (no random behavior). The other experiment was the same, except that a random variation has been added to the amplitudes of motion.

The random variations have been added by generating random numbers and adding them to the output pressure of the digital regulator (for SI direction). The generated random numbers are in the range $\pm 10\%$ of the input pressure. It means that, instead of having a deterministic input pressure P , the input pressure in the second experiment was changing randomly in the range $[0.9P - 1.1P]$ for SI direction.

Note that the random variations have been applied on SI direction only. The random numbers have been generated in the phantom motion code and added by means of the digital regulator. Since the AP actuator was not connected to any digital regulator, it was not possible to control the output pressure in a random way for AP direction.

4.2 Selecting appropriate algorithms for the problem

In order to select the most appropriate models for the motion estimation in this project, the experimental signals have been analyzed to find a correlation between the inputs and outputs.

For clarification, the inputs are: four external markers motion, each of them in two directions SI and AP, three Euler angles (needle deflections), linear accelerations in three directions ML, SI, and AP measured by IMU, and three angular rates which are the rates of needle deflection. The outputs are the tumor motion in two directions SI and AP.

Figure 4.1 shows the relations between the tumor motion in SI direction and the input signals measured in the first experiment for about 30 respiratory cycles. Figure 4.2 represents the same plots for the second experiment (with random variations) for 7 respiratory cycles.

The plots (a) and (b) in both experiments (Figures 4.1 and 4.2) suggest that although a linear fit can easily estimate the correlation between the markers motion and tumor SI motion, the relations are not completely linear and a more complex model will improve the results. The plots in (a) and (b) give the impression of two separate 2nd order polynomials. In this project, the inhalation and exhalation phases have been separated and two 2nd order polynomials are fit to the data.

In both cases, the plot (c) represents the correlation between the Euler angles (the needle deflection) and the tumor motion in SI direction, which is approximately a linear function. For the data set with random variations, the relationship is less linear.

As shown in plots (d) and (e) of both cases, there is not a meaningful correlation between the tumor displacement and the needle angular rates or the needle linear accelerations.

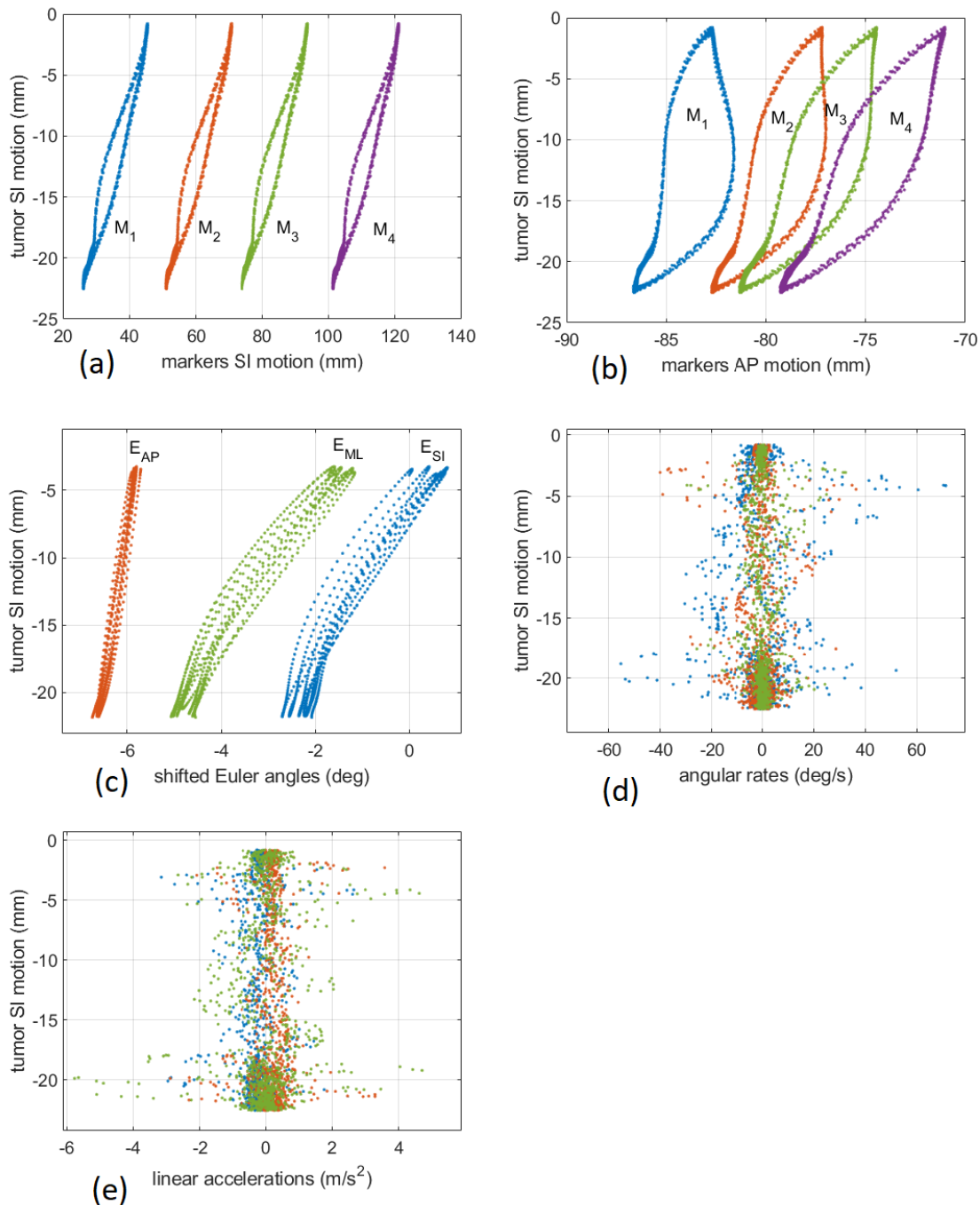


Figure 4.1: The relations between the tumor motion in SI direction and all input signals for 30 respiratory cycles obtained from the first experiment (without random variations), when the input signals are: (a) markers motion in SI direction, (b) markers motion in AP direction, (c) deflection angles of the needle, (d) angular rates of the needle deflection, and (e) the linear accelerations at the hub of the needle.

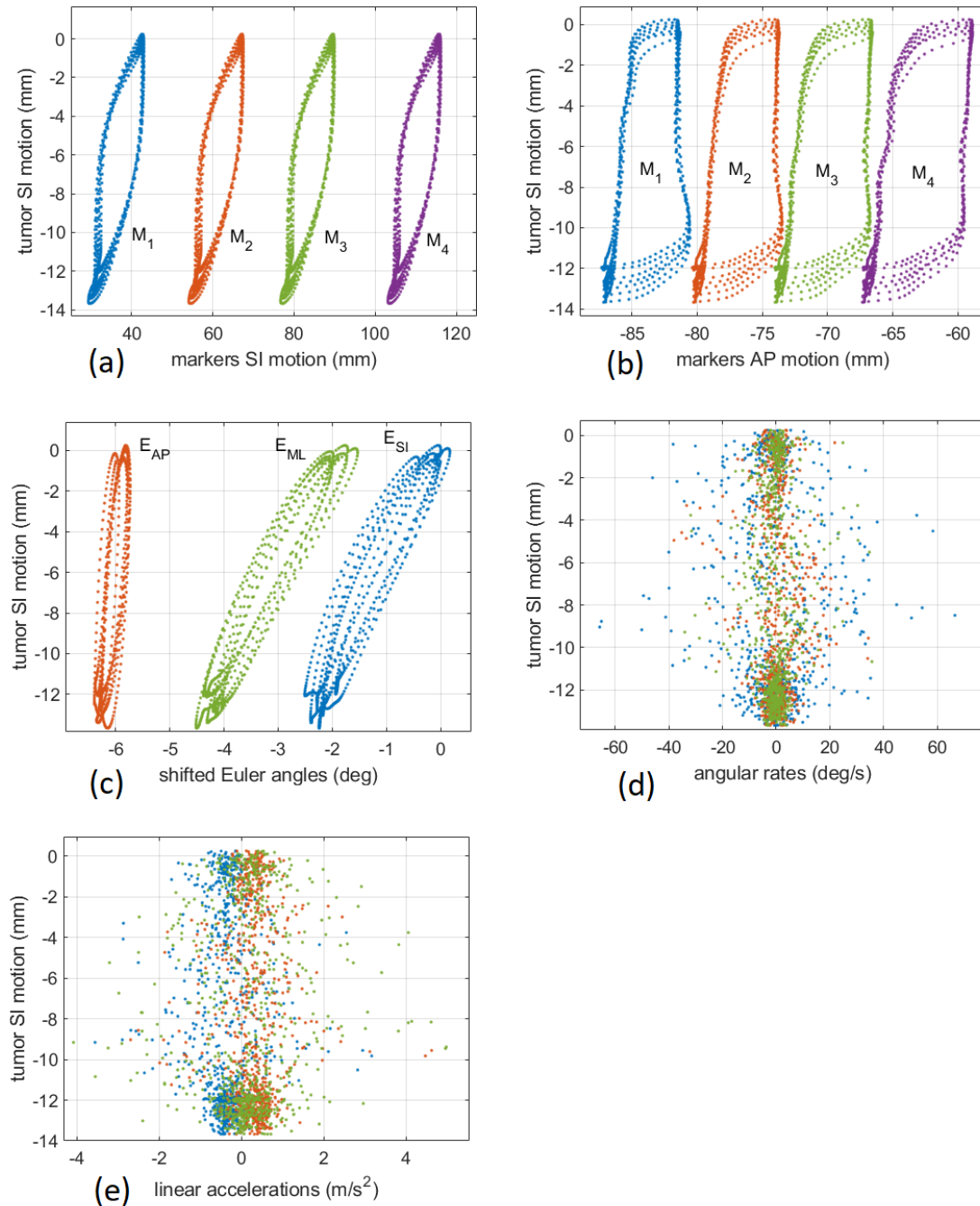


Figure 4.2: The relations between the tumor motion in SI direction and all input signals for 30 respiratory cycles obtained from the second experiment (with random variations), when the input signals are: (a) markers motion in SI direction, (b) markers motion in AP direction, (c) deflection angles of the needle, (d) angular rates of the needle deflection, and (e) the linear accelerations at the hub of the needle.

Note that the plots of the tumor AP motion versus the input signals are similar to Figures 4.1 and the plots are not presented in the report to prevent from repetition.

The following important points are concluded in this section:

- Linear regression algorithms can be a good candidate for this project due to the simplicity of the problem. However, 2nd order polynomial regression along with a respiratory phase parameter (to separate inhalation from exhalation) is expected to result in more accuracy. It means that in the regression algorithm, the tumor motion should be expressed as a 2nd order function with respect to the markers motion, and at the same time, a linear function with respect to the Euler angles.
- Among linear regression methods, ordinary multivariate regression has been chosen along with the most common regularization methods ridge and lasso to compare the results with the ordinary case. Shortly, the selected regression algorithms for this project are:
 - ordinary multivariate linear regression,
 - ridge regression,
 - lasso regression,
 - and 2nd order polynomial regression along with a respiratory phase parameter.
- The linear accelerations and angular rates do not have a meaningful correlation with the tumor displacement, and as a result, they will not be employed as inputs (features) of the regression algorithms.

4.3 Optimization and acquiring the models

As stated in the previous section, different linear and polynomial regression algorithms have been employed in this project. More details about acquiring the models in MATLAB will follow.

4.3.1 Ordinary multivariate linear regression

In this method, which is the simplest one, the output signal is approximated by a linear function of the surrogate signals, or:

$$y \approx y_{est}(\theta) = \sum_{i=0}^n \theta_i x_i, \quad (4.1)$$

where y is a vector which is the tumor motion signal measured in the experiment, y_{est} is a vector of approximations of the output signal y , n is the number of features or measured input signals, x_0 is a constant vector of ones, θ_0 is the bias term, x_i , $i = 1, 2, \dots, n$ are the features or surrogates, each of which is a vector of measurements, and θ_i , $i = 1, 2, \dots, n$ are the resulting weights of the features [52].

The goal is to find the parameters θ_0 , θ_i such that the approximated output y_{est} has the least deviation from the given output y , or equivalently, minimizing a pre-defined cost function.

Note that in this project, two regression models are obtained, one for the tumor motion in SI direction, and the other for AP direction.

Among various methods, one of the most common methods of finding the unknown parameters is the least square estimate, in which the cost function is the sum of the squared estimation errors, or the norm of the estimation error vector:

$$J(\theta) = \frac{1}{m} \|y - y_{est}(\theta)\|^2, \quad (4.2)$$

where m is the number of measured samples or the number of elements in the vectors y and y_{est} , and the unknown parameters are found for the minimum value of the cost function.

One of the numerical methods to solve the problem and to converge to the optimal answer is gradient descent [52].

In analytic methods, the solution of the least square estimate problem is

$$\theta = (X^T X)^{-1} X^T y, \quad (4.3)$$

where θ is a vector of all parameters θ_0, θ_i , and X is an m by $(n + 1)$ matrix, the columns of which are the features x_0, x_i .

In this project, the optimization has been done by MATLAB function `mvregress`.

4.3.2 Ridge regression and regularization analysis

Adding a regularization parameter helps to obtain a model with a higher ability of generalization, meaning that the estimation accuracy will be higher for "unseen" input data. By adding a regularization parameter, the estimation error for the training set increases, while it decreases for the test set (which is "unseen" data). Regularization is favorable when the model is prone to over-fitting, e.g. when the features (surrogate signals) are highly correlated. [52].

Ridge regression is one of the most common methods with regularization, and in MATLAB, it can be implemented by `ridge` function. In this method, the cost function has an extra regularization term compared to the ordinary regression cost function in Equation (4.2). The cost function for ridge regression is [25]:

$$J(\theta) = \frac{1}{m} \|y - y_{est}(\theta)\|^2 + k \sum_{i=1}^n \theta_i^2. \quad (4.4)$$

The solution is similar to Equation (4.3), except that now, there is also a regularization term:

$$\theta = (X^T X + kI)^{-1} X^T y, \quad (4.5)$$

where k is the regularization parameter [49].

When the regularization parameter k is small, the problem converges to an ordinary regression problem, and the ability of the model to generalize and have a modified performance for unseen data decreases, and vice versa. When k is large, the regularization penalty becomes larger, the training error increases, while the test error decreases [52].

In order to find the best value of the regularization parameter, it is necessary to perform a regularization analysis. First, the training data set is split into the training and cross-validation sets. Then, the regularization parameter k is changed over a specific interval, and the parameters of the model are calculated based on the training set data for each value of k . Next, the estimation error (or the cost function) is calculated for each value of k on the cross-validation set using the calculated parameters for each k . Finally, the value of k at which the cross-validation error is minimum is picked.

Figure 4.3 illustrates the regularization parameter analysis performed in this project. Figure 4.4 presents the same plots for the second experiment (with random variations).

The obtained best values of the regularization parameter k in this project for the SI and AP estimation models are:

$$k_{SI} = 7e - 05, \quad k_{AP} = 6e - 05, \quad (4.6)$$

and for the second experiment (with random variations) the optimal regularization parameter is:

$$k_{SI} = 9e - 05. \quad (4.7)$$

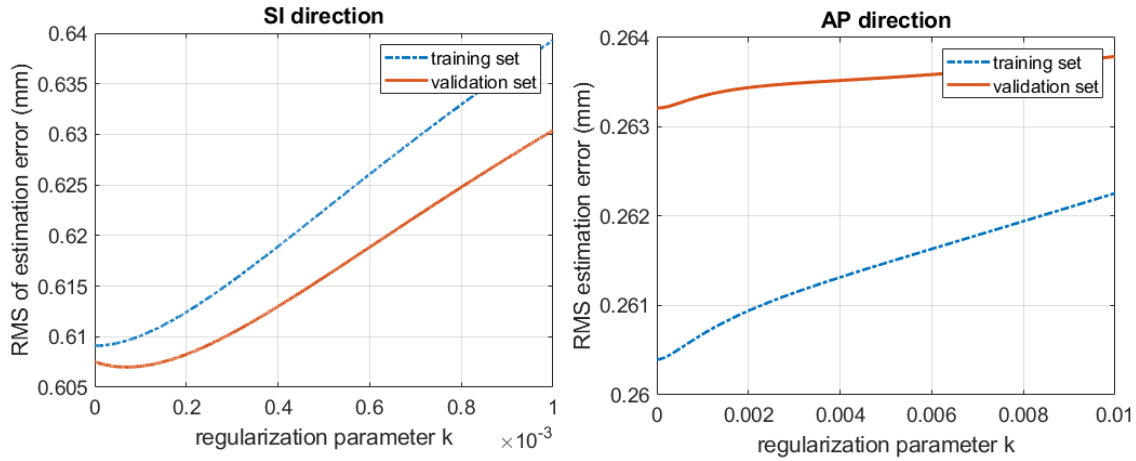


Figure 4.3: Regularization parameter analysis for ridge regression in SI and AP directions for the first experiment (without random variations). The errors are calculated on cross-validation set as well as training set.

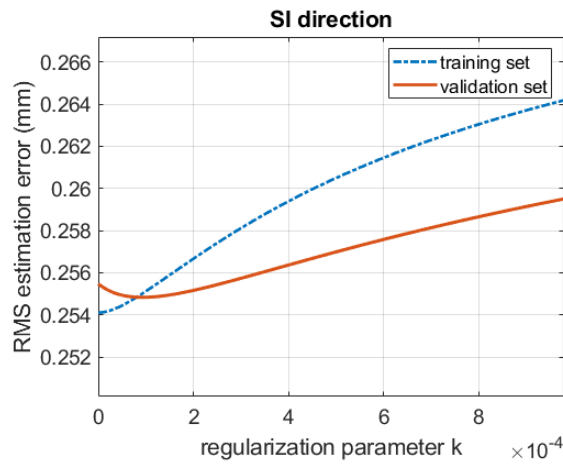


Figure 4.4: Regularization parameter analysis for ridge regression in SI direction for the second experiment (with random variations). The errors are calculated on cross-validation set as well as training set.

4.3.3 Lasso regression and regularization analysis

Similar to ridge regression, lasso is a regression algorithm with regularization. The difference between ridge and lasso algorithms is the regularization penalty in the cost function. While the cost function of ridge algorithm is described as Equation (4.4), the cost function of lasso regression is [25]:

$$J(\theta) = \frac{1}{m} \|y - y_{est}(\theta)\|^2 + \lambda \sum_{i=1}^n |\theta_i|. \quad (4.8)$$

The difference in the regularization penalty has created a major difference in the solution of the optimization. Although the obtained parameters θ in both regression algorithms are minimized, they can be exactly zero in lasso regression. In other words, lasso ignores a number of features that are in-relevant or correlated with the other features.

Another difference between ridge and lasso algorithms is that lasso is computationally more expensive, since there is not a closed-form solution for lasso [25] (similar to the one for ridge in Equation (4.5)).

A similar regularization analysis has been performed in order to select the best values of parameter λ for the two regression models SI and AP directions, and is illustrated in Figure 4.5. Figure 4.6 shows the same analyses for the second experiment (with random variations).

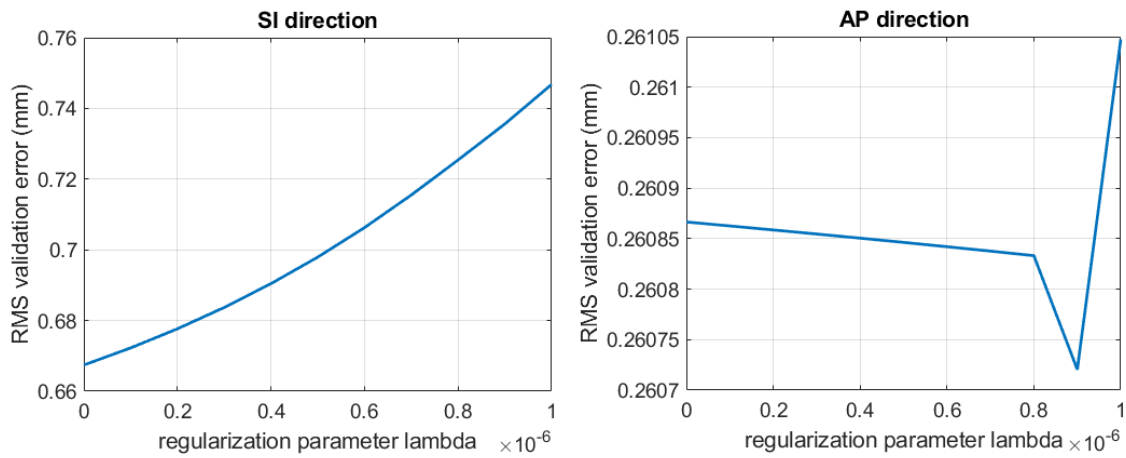


Figure 4.5: Regularization parameter analysis for lasso regression in SI and AP directions for the first experiment (without random variations). The errors are calculated on the cross-validation set.

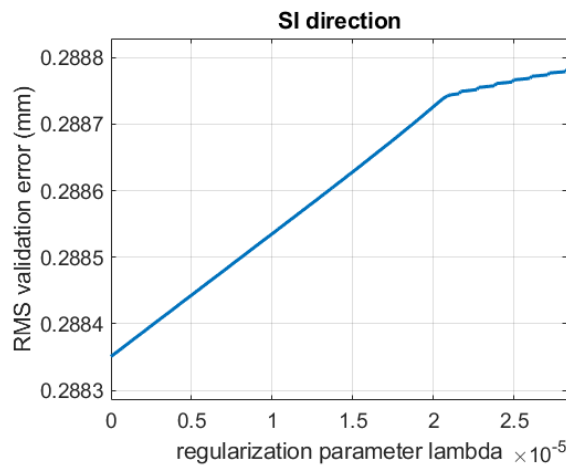


Figure 4.6: Regularization parameter analysis for lasso regression in SI direction for the second experiment (with random variations). The errors are calculated on the cross-validation set.

In this project, the optimal λ values in SI and AP directions have been:

$$\lambda_{SI} = 0, \quad \lambda_{AP} = 9e - 07, \quad (4.9)$$

and for the other experiment (with random variations) the optimal values are:

$$\lambda_{SI} = 0. \quad (4.10)$$

Note that in both cases, and in both algorithms ridge and lasso, the regularization parameters are obtained to be close to zero, meaning that the model has not been prone to over-fitting.

4.3.4 2nd order polynomial regression along with a respiratory phase parameter

A quadratic fit can be found similar to the linear regression problem in Equation (4.1), if additional quadratic features are defined. In this context, the output estimation y_{est} is still a linear function of the unknown parameters, while it includes quadratic terms x_i^2 or $x_i x_j$.

As mentioned in the previous sections, the correlation between the tumor motion and markers motion is more close to a 2nd order polynomial than a linear fit (but it was a linear correlation for the Euler angles). For that, the inhalation and exhalation phases have been separated by defining a phase parameter. The phase parameter has been defined based on the peaks and valleys of the measured signals. Then, two quadratic polynomials have been fit separately to the inhalation and exhalation data.

In this project, the quadratic estimations have been defined as:

$$\begin{aligned} y_{inhale} &\approx \hat{y}_{inhale}(\alpha, \beta, \gamma) = \sum_{i=0}^n \alpha_i x_i + \beta_i x_i^2 + \gamma_i z_i, \\ y_{exhale} &\approx \hat{y}_{exhale}(\alpha', \beta', \gamma') = \sum_{i=0}^n \alpha'_i x_i + \beta'_i x_i^2 + \gamma'_i z_i, \end{aligned} \quad (4.11)$$

where the features x_i are formed from the markers motion signals, and z_i are from the Euler angles signals, because as mentioned before, the tumor motion is approximately a linear function of the Euler angles and there is no need to add extra quadratic terms.

The parameters α , β , γ , α' , β' , and γ' are obtained by a multivariate linear regression. The respiratory phase parameters are defined as:

$$\begin{cases} a_{in} = 1, & a_{ex} = 0 & \text{inhalation,} \\ a_{in} = 0, & a_{ex} = 1 & \text{exhalation.} \end{cases} \quad (4.12)$$

The final motion estimation is obtained from the following equation:

$$y \approx y_{est} = \hat{y}_{inhale} a_{in} + \hat{y}_{exhale} a_{ex}. \quad (4.13)$$

As it will be shown in the next section, the quadratic fit is more accurate than the linear regression results.

However, a dis-advantage of this method is that the obtained motion estimation has discontinuities at the peaks and valleys, where the model jumps from the inhalation to exhalation and vice versa.

This model can improve by defining a more smooth respiratory phase parameter instead of the step-wise parameter in Equation (4.12). In that case, the model will be more general and not specific and separate for inhalation and exhalation. However, the accuracy will be lower in the modified version, and it is a trade-off between the accuracy of the estimation and the smoothness of the estimated signal.

Figure 4.7 shows the plot of estimated tumor motion as well as the measured motion versus time (for the first experiment without random variations), and the dis-continuities are visible in the plot at the peaks and valleys.

4.4 Motion estimation results and performances

In this section, the estimation results are compared between the mentioned regression methods and also between the two experiments (with and without random motion) using different measures.

4.4.1 Estimation errors

Figure 4.8 shows a graphical comparison between the ordinary linear regression and polynomial algorithms, which is the plots of estimated and real (measured) tumor motion in SI and AP directions (for the first experiment without random variations).

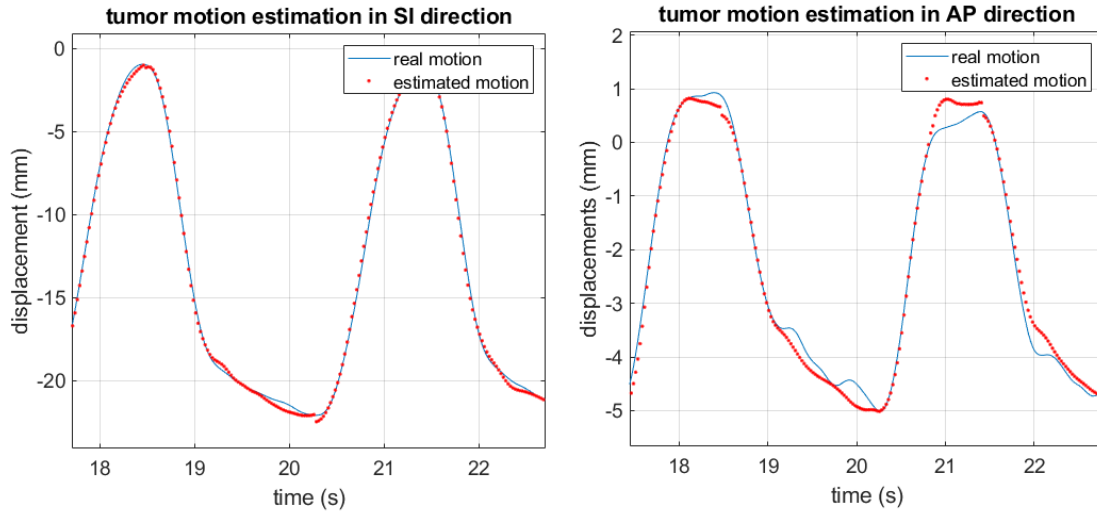


Figure 4.7: The estimation results from the 2nd order polynomial regression for the first experiment (without random variations).

In order to compare the algorithms numerically, the RMS (root mean squared) relative errors of all algorithms have been calculated for the two experimental data sets.

The RMS absolute estimation errors are calculated from the relation

$$\text{RMS absolute estimation error} = \text{RMS}(e_{\text{abs}}) = \|y - y_{\text{est}}\| = \sqrt{\sum_{i=1}^m (y_i - y_{\text{est}_i})^2}, \quad (4.14)$$

where y and y_{est} are respectively the measured and estimated vector of the outputs (tumor motion) as defined in Equations (4.1) and (4.13), m is the length of the output vectors, and y_i and y_{est_i} are the i -th element of the measured and estimated vectors, respectively.

Note that the relative errors are obtained by dividing the absolute error by the tumor motion amplitude:

$$\text{RMS relative estimation error} = \text{RMS}(e_{\text{rel}}) = \frac{\text{RMS}(e_{\text{abs}})}{\text{tumor motion amplitude}}. \quad (4.15)$$

Also note that the errors have been computed on the test set, separate from the training set. It means that 80% of the data have been selected randomly for training the model, and the rest 20% have been utilized to calculate the estimation errors. In lasso and ridge regression models, the percentages have been 60%, 20%, and 20% for the training set, cross-validation set, and test set, respectively. Also, all sets have been identical for all algorithms in order to have a fair comparison.

Figure 4.9 illustrates the RMS relative estimation errors for all algorithms in the first experiment (without random variations) as well as for the second experiment (with random variations).

From the plots, it can be interpreted that in both cases, the most accurate model is the polynomial fit as mentioned before.

Also, the errors of different linear algorithms (ordinary, lasso, and ridge) are approximately equal in both experiment cases. The reason is that the optimal regularization parameters in ridge and lasso regression have been very small (Equations (4.9) and (4.6)) and the model converged to the ordinary regression without regularization.

By comparing the results of the first and second experiments, the effect of adding random variations to the motion can be evaluated. For this purpose, the relative errors must be compared (not absolute errors), since the amplitudes of motion in two experiments were not equal.

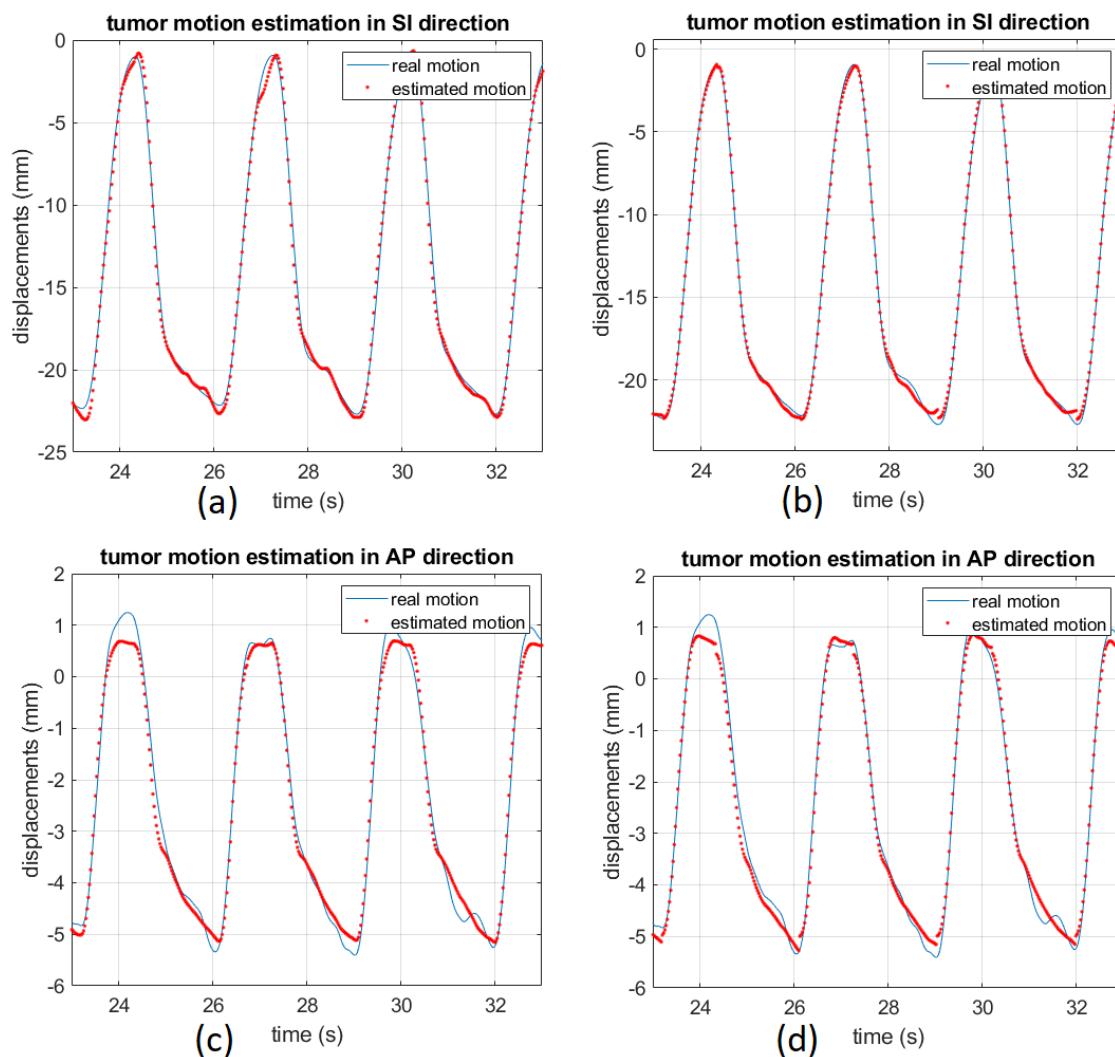


Figure 4.8: (a) and (c) the tumor motion estimation results with ordinary linear regression method in SI and AP directions, (b) and (d) the estimation results with polynomial method.

Also, in order to make a fair comparison, the data from both experiments should have the same number of cycles (same number of data points).

For the first experiment without random variations, the relative test set errors of ordinary linear method in SI and AP directions are respectively 1.37% and 2.87%, while with polynomial method the errors are respectively 0.76% and 2.41%. It can be interpreted that the polynomial method is a more accurate fit.

By comparing the plots (a) and (c) of Figure 4.9, it can be observed that the estimation errors increase by adding random motion to the phantom. It was expected, because random variations make the experiment more similar to the real case and by introducing random behavior, motion prediction becomes more difficult.

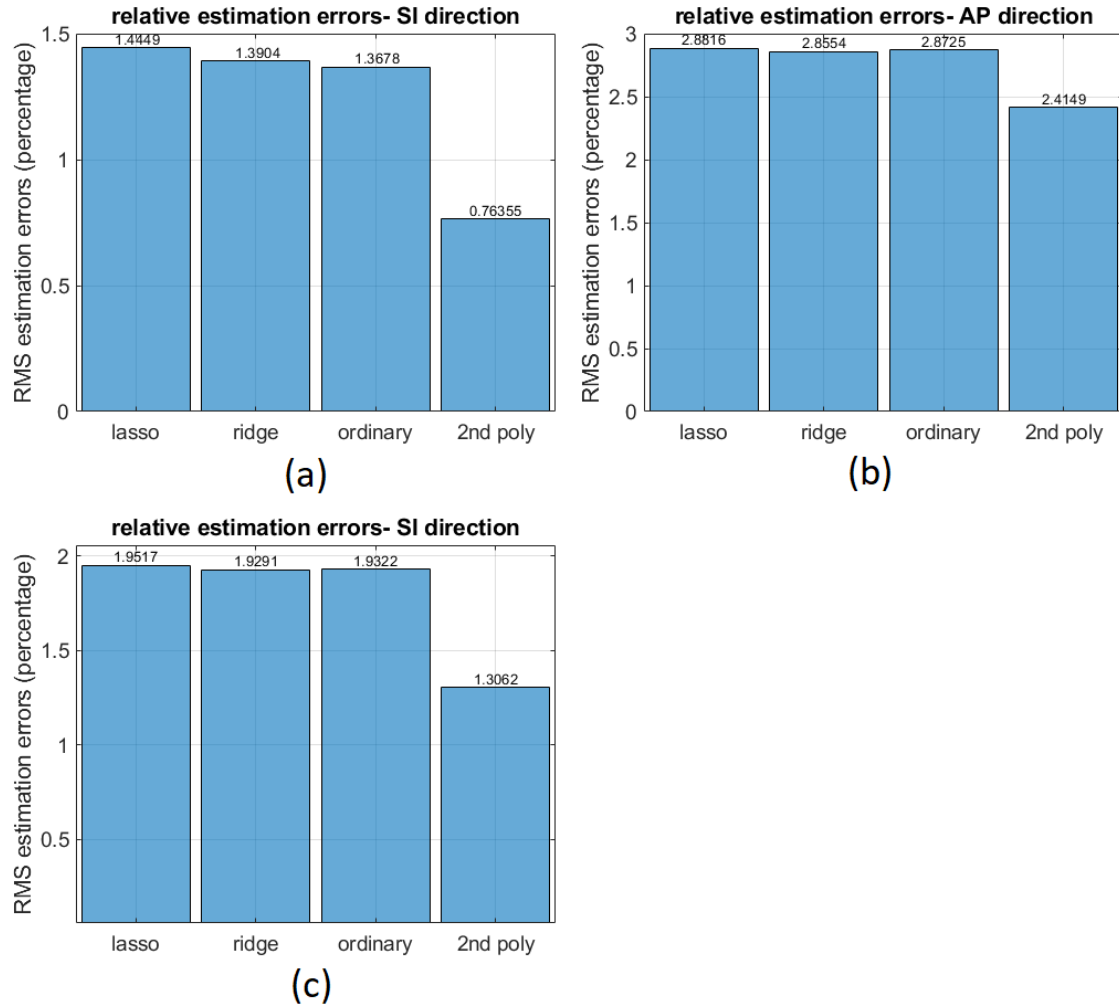


Figure 4.9: The RMS relative estimation errors of different regression algorithms for the experimental data. (a) and (b) are related to the first experiment (without random variations), and (c) is related to the second experiment (with random motion).

4.4.2 Coefficient of determination (R^2)

Another measure for evaluating the regression algorithms is the coefficient of determination (R^2), which is defined as [48]:

$$\begin{aligned}
 R^2 &= \frac{SSR}{SST} = 1 - \frac{SSE}{SST}, \\
 SSR &= \sum_{i=1}^m (y_{est_i} - \bar{y_{est_i}})^2, \\
 SSE &= \sum_{i=1}^m (y_i - y_{est_i})^2, \\
 SST &= \sum_{i=1}^m (y_i - \bar{y_i})^2,
 \end{aligned} \tag{4.16}$$

where y_i and y_{est_i} are respectively the i -th element of the measured and estimated vectors, m is the length of the output vectors, and the bar sign stands for the average of the data.

According to the above definition, coefficient of determination (R^2) is the proportion of the variance in the outputs of the regression model that is predicted by the inputs of the model.

Its value is between 0 and 1, which are often related to an extremely bad fit and a perfect fit, respectively.

Figure 4.10 presents the plots of calculated R^2 values for different regression algorithms for both experimental cases (with and without randomized motion). In all plots, the calculated R^2 values are large and close to 1.

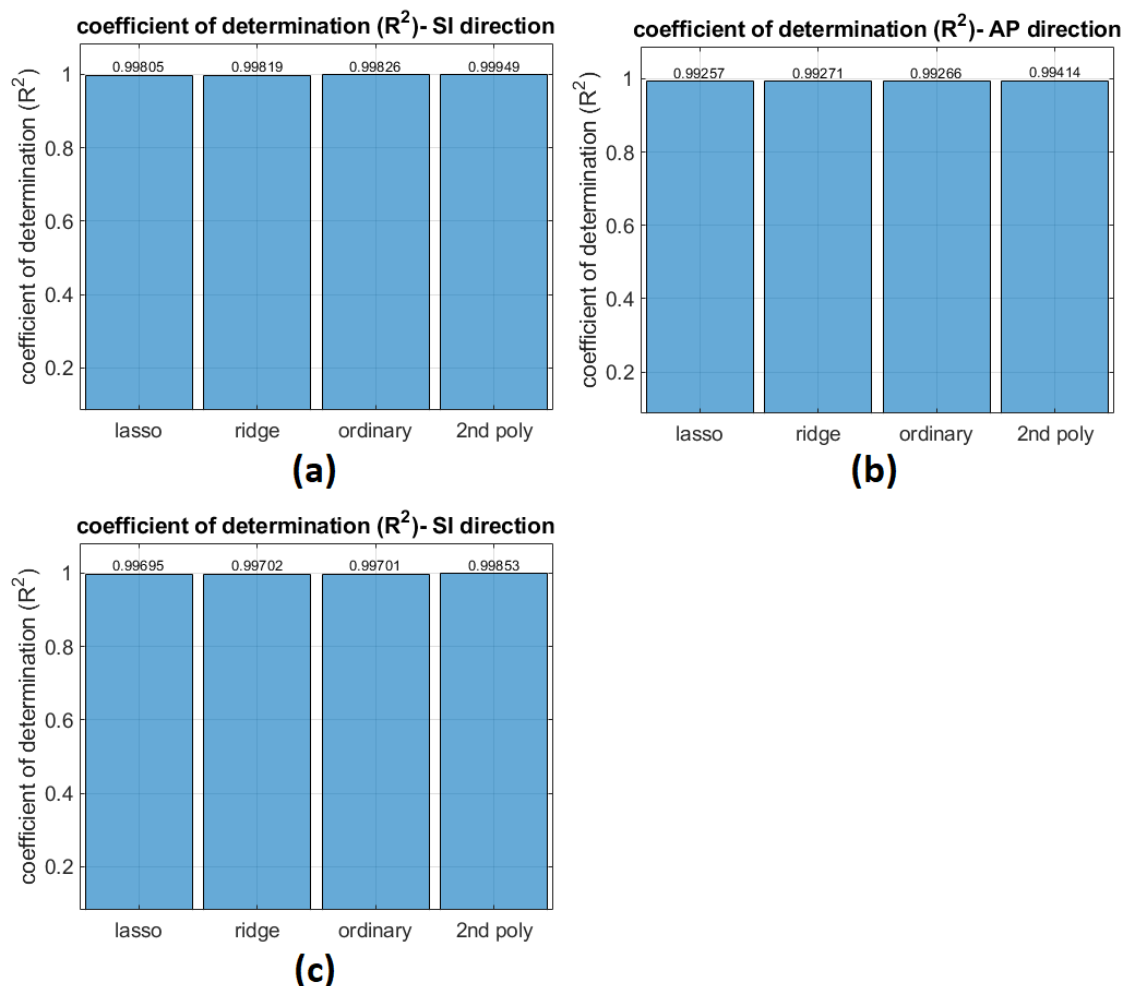


Figure 4.10: The calculated values of coefficient of determination (R^2) for different regression algorithms for the experimental data. (a) and (b) are related to the first experiment (without random variations), and (c) is related to the second experiment (with random motion).

Note that coefficient of determination (R^2) is NOT necessarily a measure of goodness-of-fit, but it is a measure of to what extent the estimated and measured outputs are linearly correlated (i.e. $y = ay_{est} + b$). In this context, goodness-of-fit means how much the relation between the measured and estimated outputs is close to the specific line $y = y_{est}$ ($a = 1$, $b = 0$) [11].

It means that, coefficient of determination (R^2) cannot determine whether a regression model is biased (or too simple) or not.

In Figure 4.10, the calculated R^2 value of the linear regression algorithm is as high as that of the polynomial algorithm. It means that the coefficient of determination (R^2) has not been able to detect that the linear model is more biased (simpler) than the second order model.

As a result, the coefficient of determination (R^2) is often used along with other measures of evaluation.

4.4.3 Standardized residuals plot

The plots of residuals help to investigate the distribution of the errors (or residuals) of the predicted model.

The residual plot is the plot of the residuals (errors) on the vertical axis vs. an independent variable, or the inputs (features), or the estimated values, etc. on the horizontal axis.

The standardized residuals plot is similar to the regular residuals, except that the vertical axis is scaled and the outliers can easily be detected from the plot.

In this project, the standardized residuals are calculated from the following relation:

$$\text{standardized residual} = SR = \frac{y - y_{est}}{\frac{\text{RMS}(e_{abs})}{\sqrt{m-n}}}, \quad (4.17)$$

where m is the length of the output vectors y and y_{est} , and n is the number of model parameters including the intercept term. The denominator of the above formula represents the standard deviation of the errors.

The standardized residual has been calculated for each test sample data and plotted vs. the sample number, and is shown in Figure 4.11.

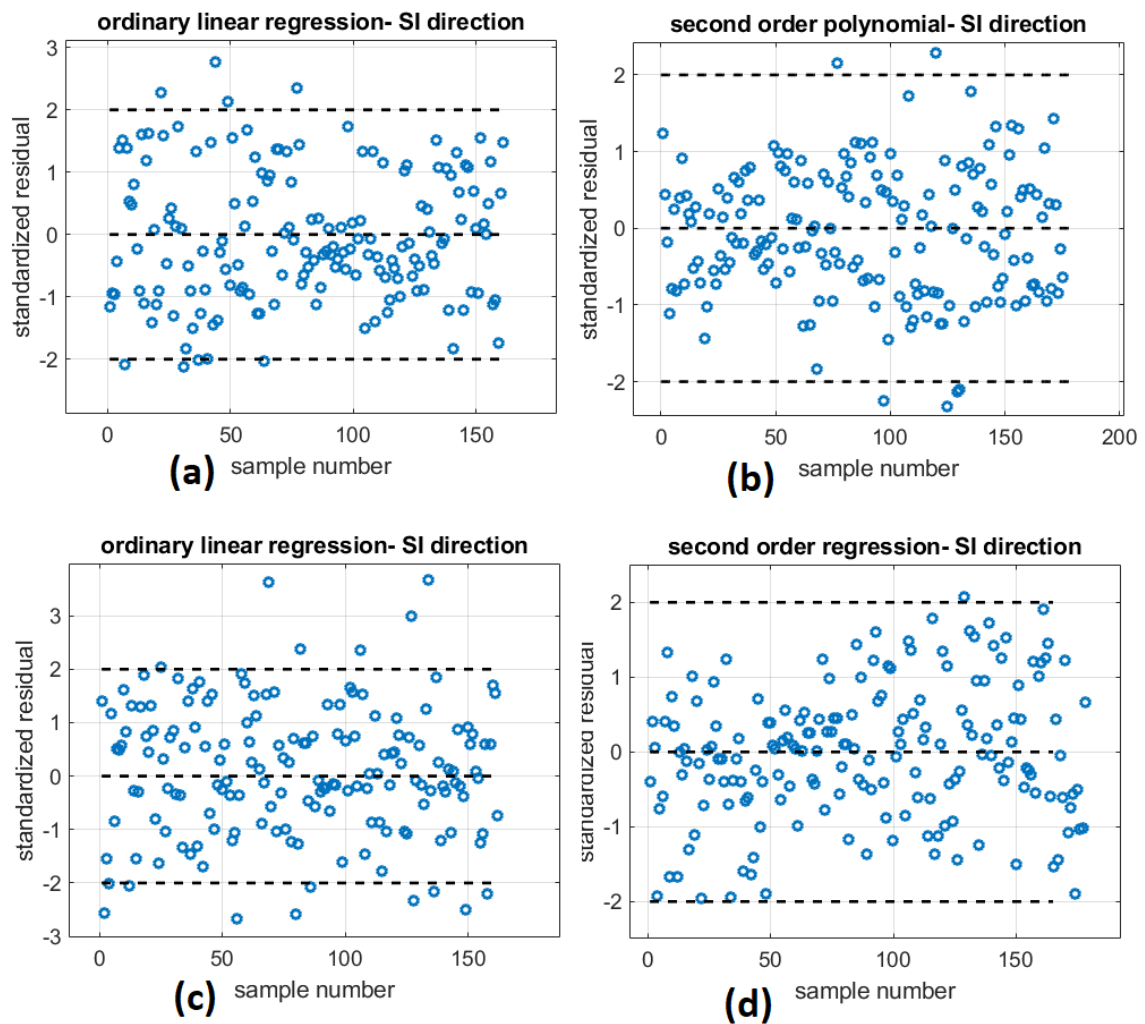


Figure 4.11: The standardized residuals calculated for different cases in SI direction. (a) and (b) are the plots for the first experimental data (without randomized motion), and (c) and (d) are the plots for the second experimental data (with randomized motion).

Note that the residuals for AP direction are similar to the plots of Figure 4.11.

From the plots (a) and (b), it can be observed that the errors are more concentrated close to zero with a polynomial regression, which means that it is a more accurate fit. Also, the errors in plot (c) are more scattered (farther from zero) than (a) and in (d) are more scattered (farther from zero) than (b), because the data in (c) and (d) are from the second experiment with randomized motion and the errors are larger.

4.4.4 Training time

Another useful measure for the comparison of different regression algorithms is the training time, or the time that it takes for the computer to find the optimal parameters of the regression model.

The training time is important in real-time applications, since the data are measured, processed, and at the same time, the parameters of the regression model are optimized. All of the procedures should be done in a minimum amount of time, so that the delay becomes small and therefore the results can be useful for real-time motion estimations. In off-line applications like this project, the regression model can be learned in advance and the importance of the training time is much lower. However, in order to assess which algorithms can be used in real-time applications, a comparison between the training time of different regression methods are given in this section.

The training time depends on several factors, such as:

- the regression model complexity (or the number of parameters to be optimized),
- the number of training samples,
- the computation algorithm,
- the speed of the computer, which depends on the memory, processor, etc.

In this project, the training time of different regression algorithms have been calculated using the MATLAB function `tic`, `toc` for the first set of experimental data (without randomized motion) for the same training data set¹.

Figure 4.12 presents the calculated training time for different algorithms.

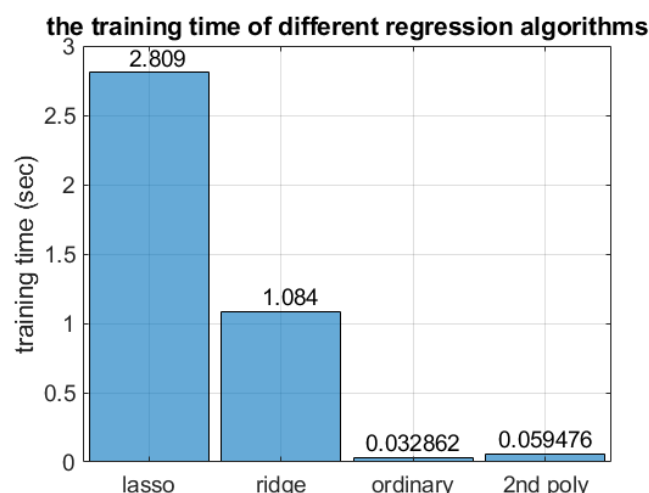


Figure 4.12: The calculated training time of different regression algorithms with the data from the first experiment (without randomized motion).

¹Information about the computer that was used: processor: Intel(R) Core(TM) i7 CPU Q 720 @ 1.60GHz 1.60 GHz, installed memory (RAM): 8 GB

As shown in the figure, the training time of ridge and lasso algorithms are larger than ordinary linear regression, because the time for finding the optimal regularization parameter has been included, meaning that the algorithm has been repeated many times for different values of the regularization parameter. Without including the cross-validation in the training time, the difference between the training time of linear methods would have been smaller.

Also, the training time of lasso regression is greater than ridge, since it is computationally more expensive (as mentioned in the previous sections) (the factor of computation algorithm).

Another interesting point is that the training time of the second-order polynomial method is approximately twice that of the ordinary linear regression. The reason is that the second-order polynomial method has more number of parameters to be optimized than the linear model (the factor of model complexity).

Choosing the best algorithm is a trade-off between the accuracy of the result and the complexity (or training time) of the model. Although the training time of polynomial regression is larger than that of ordinary linear regression, it is still small. By noticing Figure 4.9 and the fact that the polynomial method has the smallest estimation error while its training time is small enough, it can be concluded that the polynomial method is an appropriate algorithm for this project and possibly for real-time estimations.

4.4.5 Learning curves

The learning curve is a plot in which the change of errors due to the change in the number of training samples is illustrated.

The horizontal axis of the learning curve is the number of training samples (or the size of the training set). Each training set, the size of which is shown on the horizontal axis, is used to train a separate regression model and the training error is shown as a point in the plot for the specific size of the training set. Each of the obtained models is also used to calculate the test error, using a fixed-size test set, and the test errors are also shown in the learning curve plot.

In the learning curve plots, the training error increases with the increase in the number of training samples. The reason is that for a larger training set, it is more difficult to fit a model to the data which can generalize and estimate all point accurately, than a training set with a few data points, in which a model can easily fit to the data well.

However, the trend of test error is opposite to the training error: the test error decreases as the number of training samples increases. The reason is that by using more data points to train the model, the obtained model has "seen" more training data and is more able to generalize. Therefore, such model has smaller error on the "unseen" data.

Another property of the curves is that they converge to a specific error value. It means that the change in the errors becomes very small for a large-enough training set and the curves become approximately a horizontal line.

By means of the learning curve, it can be specified whether a model has bias (under-fit) or variance (over-fit). In general, if both the training error and test error converge to a small value, the model is fine. If both errors converge to approximately the same value, but that error value is large, it means that the model is too simple or suffers from under-fit (bias). If there is a gap between the training and test error, meaning that the test error is large while the training error is small, it is an indication of that the model is over-fitting (the model is accurate for the training set data but it cannot generalize well for the "unseen" data). Finally, if the curves have not converge yet (the errors changes are still large), it means that the number of training samples is too small and more data should be used for training [52].

Figure 4.13 shows the learning curve for the regression models in SI and AP directions for ordinary linear regression model as well as second-order polynomial. The data is from the second experiment (with randomized motion).

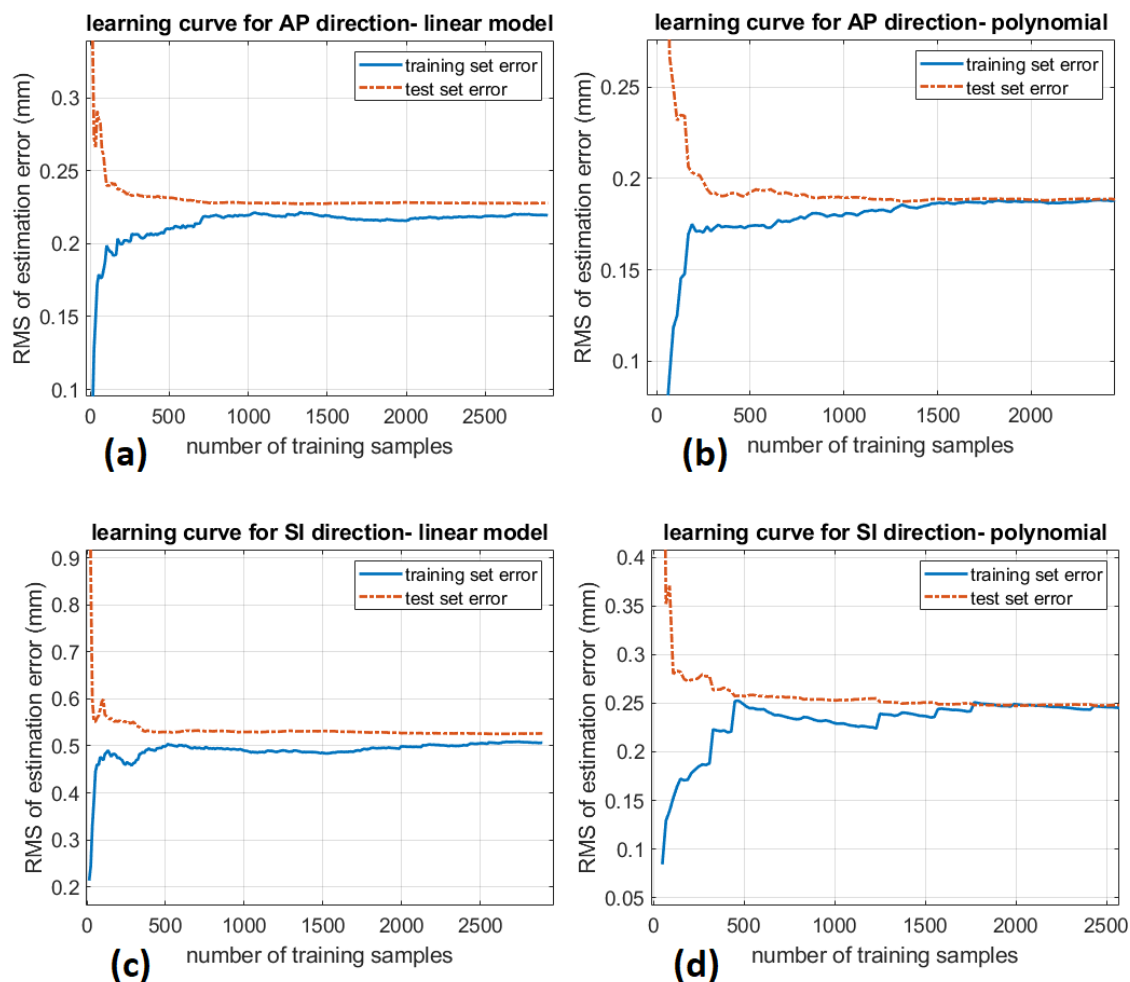


Figure 4.13: The learning curves of ordinary linear regression model in AP and SI directions in plots (a) and (c), respectively. Similar plots are shown for second-order polynomial model in (b) and (d). The data is from the second experiment (with randomized motion).

As it is observable in the plots, in all cases, the training and test errors have converged to an approximately constant value, meaning that the number of training samples has been sufficient.

In the plots of linear regression model, the training and test errors are larger than those of the polynomial model, meaning that the linear model is less accurate for motion estimation.

Also, the gaps between the training and test errors are larger than those of the polynomial models. It means that the linear regression model has higher bias (under-fit) than the polynomial model, because linear model has lower complexity and therefore is less appropriate and less accurate to describe the input-output relation.

4.5 Comparison between the surrogate signals

In order to compare different features (surrogate signals) in terms of their contribution to the overall estimation error and determine which surrogates are more effective in the tumor motion estimation, a feature selection analysis has been performed. For this purpose, various models have been obtained for different choices of surrogates.

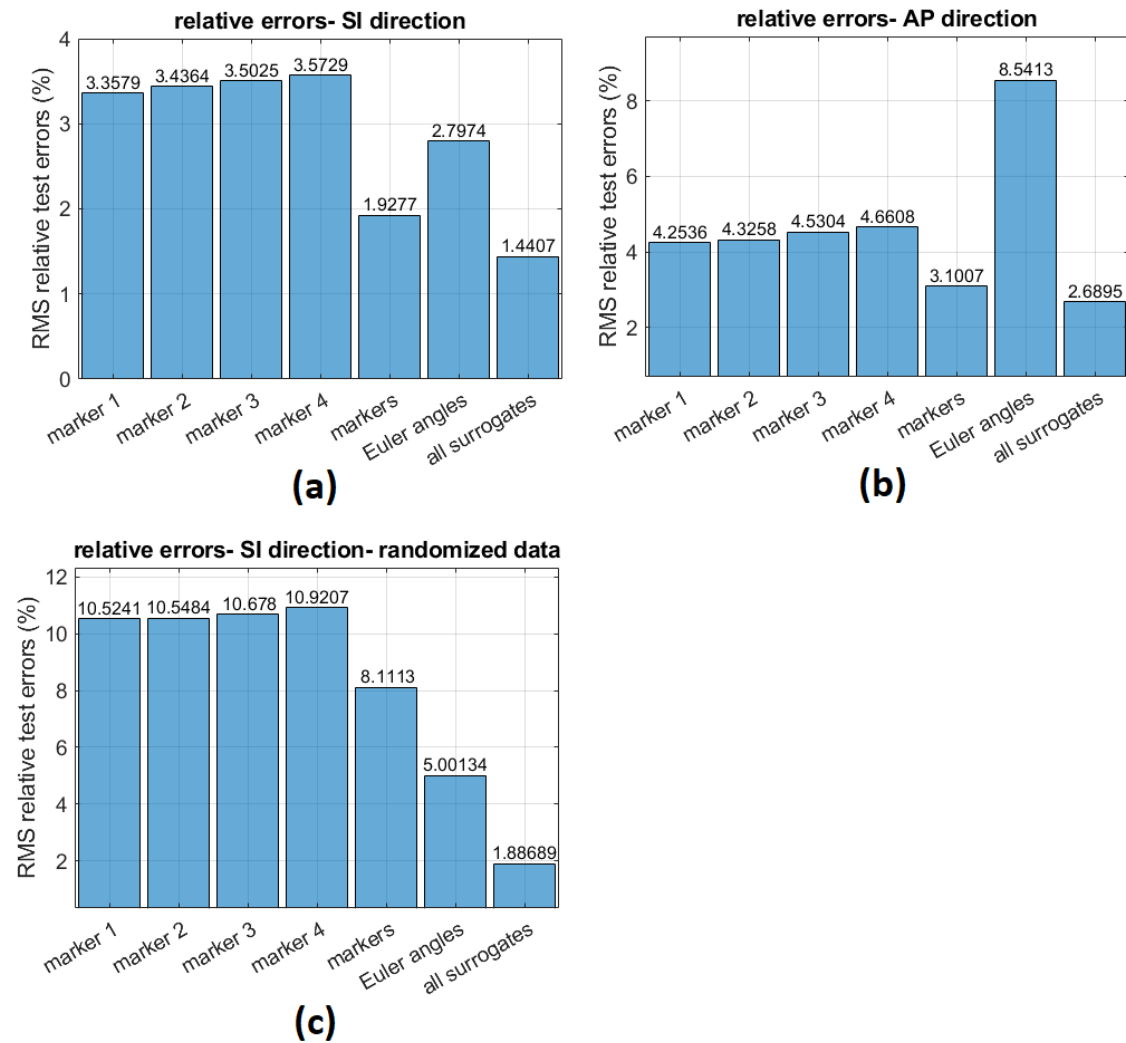


Figure 4.14: The RMS relative errors of ordinary linear regression model for different choices of surrogates, (a) and (b) for tumor SI and AP motion estimation, with the data from the first experiment (without randomized motion), and (c) in SI direction with the data from the second experiment (with randomized motion).

Figure 4.14 presents the RMS of relative estimation errors for tumor motion in SI and AP directions, and the estimations are based on an ordinary linear regression model. The plots (a) and (b) are obtained from the first experimental data set (without randomized motion) and the plot (c) is obtained from the second experiment (with randomized motion).

Figure 4.15 illustrates the same analysis with the same data sets, but with a polynomial regression model.

Note that the errors have been divided by the tumor motion amplitude in order to have relative errors and make it possible to compare the randomized motion experiment with the other experimental data.

The following important points can be observed from the plots of Figures 4.14 and 4.15:

- By comparing the plot (c) with (a) in both figures, it can be seen that all the relative errors are larger in case the motion includes random variations (as expected).
- The difference between the estimation errors of all four markers is small, since the markers have been placed closely and the markers' motions are highly correlated.

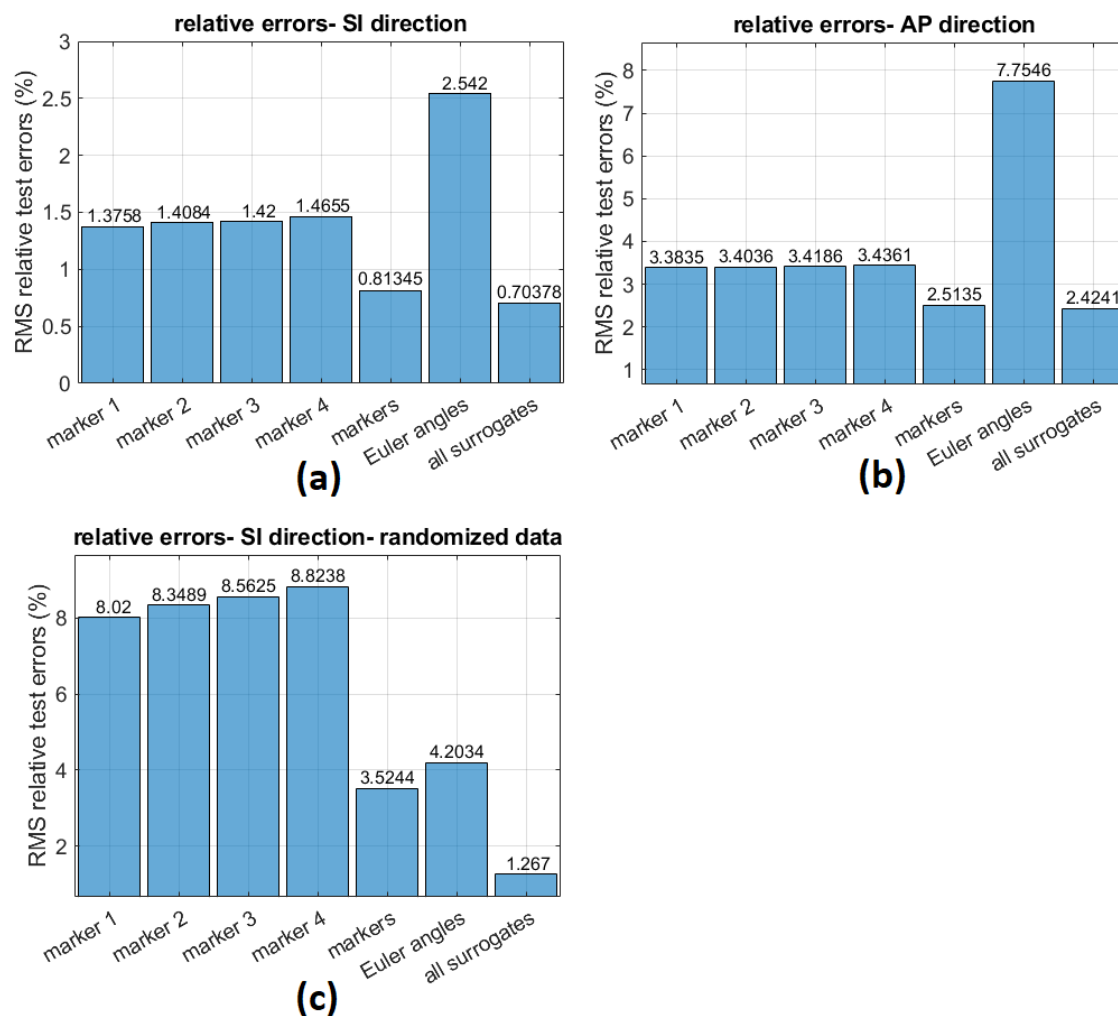


Figure 4.15: The RMS relative errors of second-order polynomial regression model for different choices of surrogates, (a) and (b) for tumor SI and AP motion estimation, with the data from the first experiment (without randomized motion), and (c) in SI direction with the data from the second experiment (with randomized motion).

- The combination of all markers has led to an error smaller than that of each separate marker. Although the markers motions are correlated, they still have a small difference and combination of the markers helps to increase the accuracy. It is because by having multiple markers, the dynamics of the phantom can be better captured and described comparing with when only one marker is present.
- By comparing the errors related to the markers and to the Euler angles, it can be observed that there is no specific relation between them. In one case, the error of the Euler angles is smaller than all markers; in another case, it is smaller than all markers but larger than the combination of markers; and in another case, it is larger than all markers. Therefore, between the Euler angles and the markers, there is no superiority and the answer to the question of "which surrogate signal is more helpful?" depends on the experimental data set, the regression algorithm, etc.
- The estimation error with all surrogate signals is the smallest error in all cases. It means that augmenting all surrogates and adding the information about the angles to the markers motions helps to increase the accuracy.

The answer to the first research question: The level of correlation between the surrogates and the tumor motion depends on the specific experimental data measured from each patient. In this project and with the constructed phantom, there is no specific superiority when the Euler angles and markers displacements are compared. However, the combination of all Euler angles and markers displacements results in a more accurate model comparing with when only the Euler angles or the markers are used (the combination of all surrogates is better than each one of the surrogates).

4.6 Summary

In this chapter, the best learning algorithms for the tumor motion estimation have been chosen by analyzing the relation between the input and output data obtained from the experiments. The data sets have been measured in two experiments: one with and the other without random motion variations.

Then, it is explained how to obtain and optimize different regression models using a specific cost function and MATLAB commands.

Next, different regression algorithms have been employed to fit a correlation model between the surrogate signals and tumor motion, and comparisons have been made between the performances of the algorithms using different measures of evaluation.

Finally, different surrogate signals have been compared in order to determine which surrogates have a higher correlation with the tumor motion and to answer one of the research questions of this project that was posed in Chapter 1.

5 Model generalization with FEM

This chapter is devoted to the simulation of the experimental setup and investigating the effects of different parameters on the tumor motion estimation. First, a finite element model of the complete experimental setup, including the liver and tumor phantom, the markers, and IMU is created using one experimental data set and then validated with another data set. Then, the simulation has been repeated for different values of the parameters. Also, surrogate signals and tumor motion signals have been generated for different cases. The finite element modeling and simulations have been performed by one of this project supervisors (Hamid Naghibi Beidokhti M.Sc). Next, by a sensitivity analysis, the effect of the parameters on the tumor motion has been investigated. This chapter ends with a discussion about the contribution of FEM to this project, the effect of the parameters on the learning-based tumor motion estimation, and the answers to the research questions in Chapter 1.

5.1 Creation and validation of FE model

As mentioned in Chapter 3, the complete experimental setup has been modeled with a finite element analysis software¹ by Hamid Naghibi Beidokhti M.Sc, as shown in Figure 3.5. The model includes all parts of the phantom such as the liver, tumor, actuators, etc. as well as the markers and IMU (attached to a needle).

The purpose of simulating the experiments with FE modeling is to repeat the experiments for different values of the parameters and generate more data sets (tumor motion and surrogate signals). Then, the simulation data are used to investigate the effect of the change of the parameters on the tumor motion as well as on the learning-based model.

The reason of simulating the experiments by FEM instead of repeating the experiments is that the experiments have low repeat-ability, meaning that it is not possible to keep all parameters exactly the same while changing one parameter only. For example, it is impractical to avoid changes such as the change of tension force in the latex parts (skin and diaphragm), since they are removed and secured again for each experiment.

The model has been created and validated based on the experimental data. For this purpose, an experiment without randomized motion has been performed in two different modes with two different amplitudes of motion (normal and shallow breathing modes). The data from the normal breathing mode has been used for creation of the model, and the other data set (shallow breathing mode) for validation of the created model.

In both experiments, the air pressure of the AP actuator has been changing between 0 and 2 *bar*. The pressure of SI actuators has been between 0 and 0.5 *bar* in the normal breathing experiment and between 0 and 0.3 *bar* in the shallow breathing experiment.

Figure 5.1 illustrates the plots of experimental data for creating the FE model, as well as the simulated data from the FEM. In all plots, the simulated data agrees well with the experimental data (as expected).

Note that only the plots of marker 1 are given in the figure, since the plots of other markers are similar to marker 1.

As discussed above, another experimental data set with different motion amplitudes and different pressure of the actuators (or shallow breathing) has been used for validation of the FE model. Therefore, the FEM has been simulated in shallow breathing mode as well for validation and comparison with the experimental data.

¹Abaqus FEA

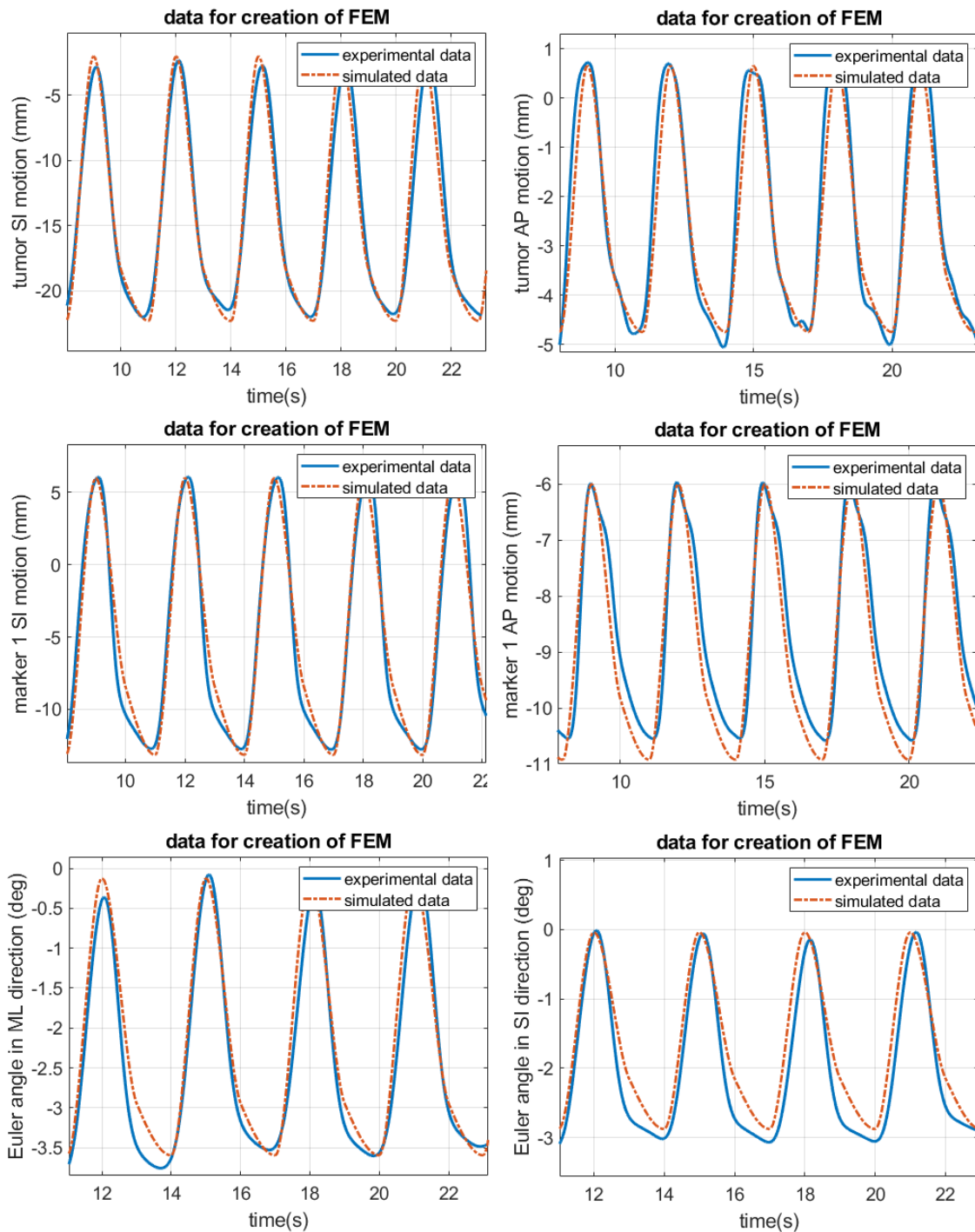


Figure 5.1: The plots of experimental data for creation of FE model along with the simulated data for comparison.

Figure 5.2 shows the plots for validation of FE model. The data from the shallow breathing experiment as well as the relevant simulated data are plotted. Again, the simulated data agrees well with the experimental data, meaning that the simulation is valid.

5.2 Data sampling frequency

One of the factors that affects the total simulation time of the FE model is the value of the simulation step time (or the updating rate or the sampling frequency of the simulation data). The FE simulation time becomes very large for very small sampling frequencies, which are often unnecessary.

In this project, the sampling frequency of the simulated data has been chosen as small as possible, in order to reduce the simulation time. However, there is a lower limit for the sampling frequency, according to the Nyquist Theorem:

$$f_s \geq 2f_{max}, \quad (5.1)$$

where f_s denotes the sampling frequency and f_{max} indicates the highest frequency of the system dynamics.

In order to capture the dynamics of the respiratory signals, the sampling frequency of the FE simulation data must be at least twice the respiratory frequency.

In this project, the respiratory frequency is approximately 0.3 Hz. In order to satisfy Equation (5.1), the FE sampling frequency is chosen to be 1 Hz.

$$f_{max} = 0.3 \text{ Hz}, \quad f_s = 1 \text{ Hz}. \quad (5.2)$$

Note that in addition to Equation (5.1), another constraint for the simulation is that the points of peaks and valleys of the respiratory signals are always included in the simulations.

Also note that the simulated data have been interpolated to generate sufficient number of data points. For this purpose, after that the data have been simulated with the sampling frequency of 1 Hz, the data are then interpolated by cubic Hermite interpolation to generate more data points with a high enough sampling frequency. However, it is required to check whether the interpolated data is reliable.

Figure 5.3 illustrates the plots of an example case, which has been simulated with sampling frequencies of 1 Hz and 10 Hz. The data with the sampling frequency of 1 Hz have been interpolated with frequency of 10 Hz, and is plotted as well.

By comparing the interpolated data with the simulated data with sampling frequency of 10 Hz, it is concluded that the difference between the interpolated data and higher-frequency simulated data is negligible.

Therefore, in this project, the simulations have been performed with sampling frequency of 1 Hz (in order to reduce the total simulation time) and then interpolated to generate sufficient number of data points.

5.3 Sensitivity analysis

In order to observe the effect of changes of the parameters on the tumor motion, a sensitivity analysis has been performed.

For that purpose, the FE simulation has been repeated for different cases in which the parameters have been changed.

In Chapter 1, it was mentioned that although in the existing literature, there are numerous studies about considering the effects of many parameters (such as the inter-cycle, inter-patient, and

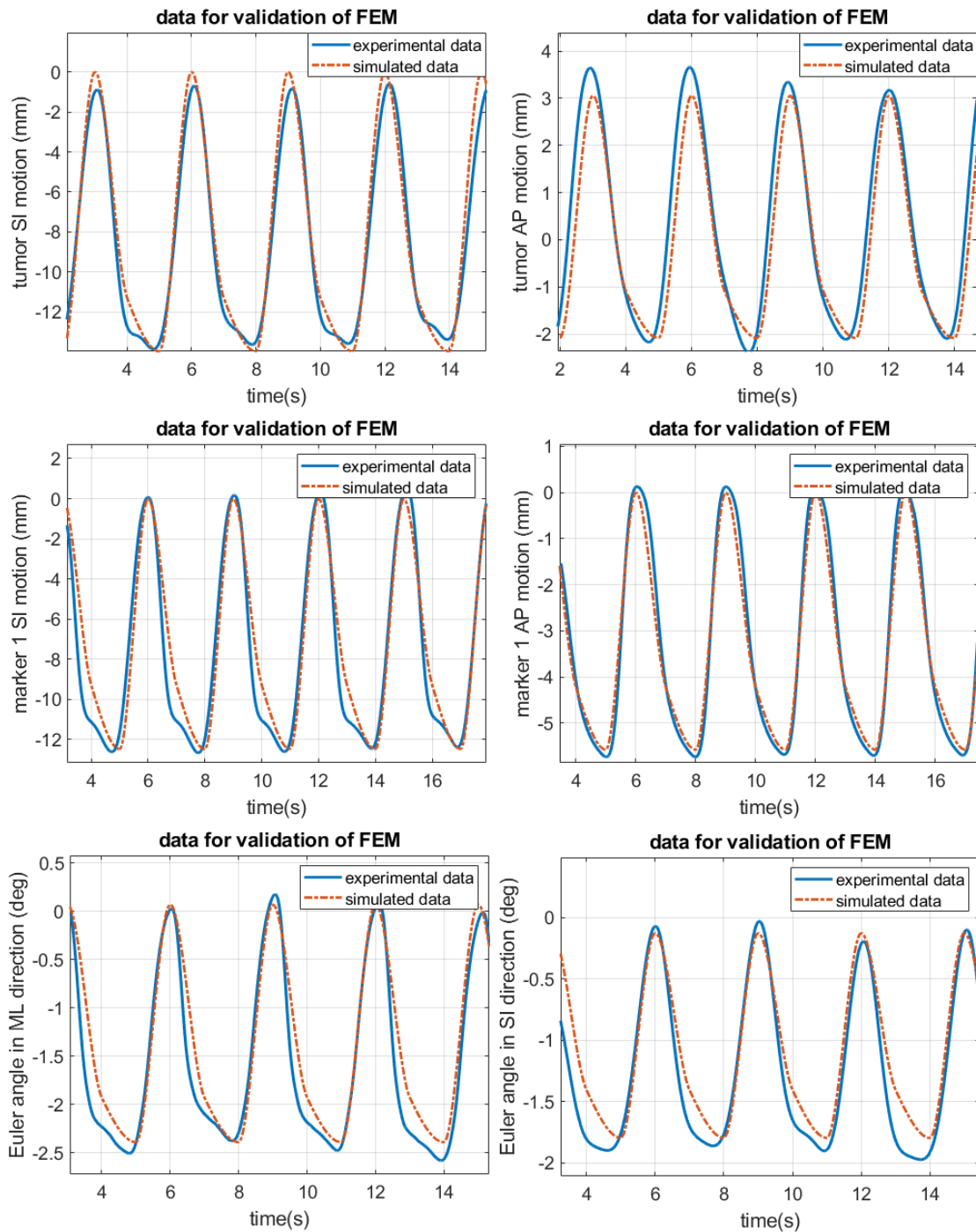


Figure 5.2: The plots of experimental data for validation of FE model along with the simulated data for comparison.

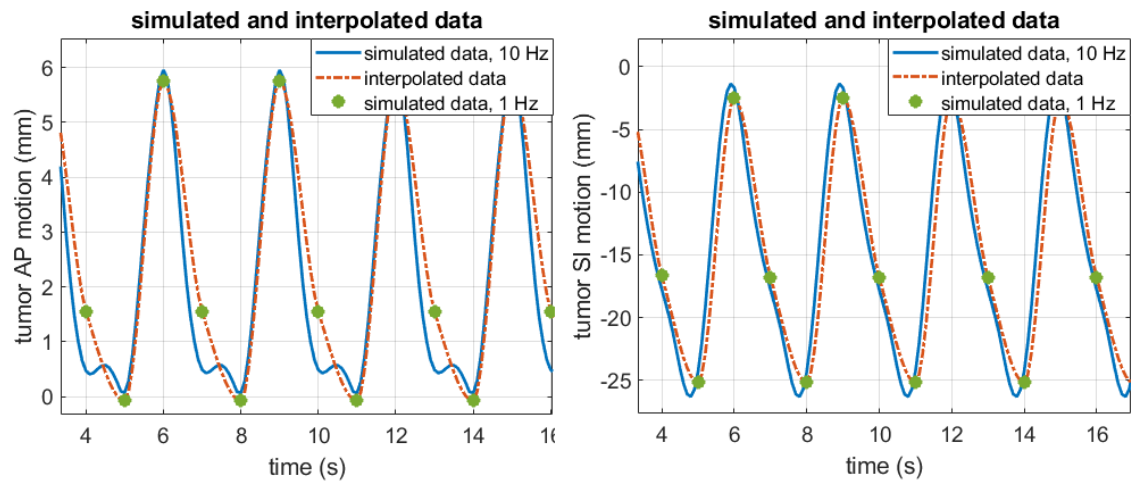


Figure 5.3: The plots of simulated data with high and low sampling frequencies (10 Hz and 1 Hz) along with the interpolated data which is obtained from the low-frequency simulated data by interpolation.

inter-fractional variations, etc.) into account in the context of respiratory motion estimation, still there exist a number of parameters that rather less studies so far have considered their effects on respiratory motion estimation.

The parameters that have not been studied (widely) in the previous works and literature are but not limited to:

the tumor size, the shape and deformations of the tumor, location of tumor inside the organ, properties of the organ tissue (like density or elasticity) as well as the tumor tissue, the breathing pattern (deep, normal, etc.), and the position of the sensors that measure the surrogates and motion of interest.

Among the mentioned parameters, the parameters that have been considered in this project to generate FEM data sets are:

- the tumor size,
- the tumor location inside the liver,
- and the liver elasticity.

The reason of not choosing the parameter shape and deformation of the tumor is that the modeling and simulation of this case is complex and beyond the scope of this project. Also, the rest of the parameters have not been picked since their effects would be less important or less dominant comparing to the chosen parameters, or although their effects cannot be ignored (e.g. the effects of the breathing pattern), the limited time scope of this project did not allow to simulate them as well.

Table 5.1 presents different choices of parameters, resulting in 8 different cases. The FE model has been simulated in these cases in order to compare the simulation data and evaluate the effects of the parameters by means of a sensitivity analysis.

Note that the values of the parameters tumor size and liver elasticity have been chosen according to the ranges in the literature, which were mentioned in Chapter 2, Section 2.3.

Also note that for the parameter tumor location inside the liver, four locations with different SI, AP, and ML coordinates have been selected.

As it can be seen in Table 5.1, between each two cases, only one parameter differs and any other parameters are equal. For example, in order to observe the effect of the tumor size on the tumor motion amplitude, FE simulations have been performed (cases 1, 2, and 3) in which all

Table 5.1: Different cases of parameters choices in which the FE model has been simulated for the sensitivity analysis.

Case No.	Tumor radius			Liver elasticity			Tumor location in the liver			
	1 cm	2 cm	3 cm	8 kPa	16.5 kPa	40 kPa	Loc. 1	Loc. 2	Loc. 3	Loc. 4
1			×		×			×		
2		×			×			×		
3	×				×			×		
4			×	×				×		
5			×			×		×		
6			×		×		×			
7			×		×				×	
8			×		×					×

parameters, pressures, forces, etc. are equal, except that the tumor size is different between the simulations. In this example, any change in the tumor motion amplitude can be attributed to the change in tumor size.

Note that the FE simulated data for the sensitivity analysis exclude any randomness in the motion. The reason is that if the simulated motion was randomized, then it would not be possible to identify which part of the change in the tumor motion was due to the change in parameters and which part was due to the randomness of motion.

In this project, the sensitivity of tumor motion to the change of parameters is defined as:

$$\text{Sensitivity} = \frac{\text{change of tumor motion amplitude}}{\text{change of parameter}},$$

or:

$$S = \frac{\Delta a}{\Delta p}, \quad (5.3)$$

where a denotes the amplitude of tumor motion and p represents the value of a parameter.

In the next parts, the sensitivity of tumor motion to each of the parameters will be discussed.

5.3.1 Sensitivity of tumor motion to tumor location in the liver

By comparing the cases 1, 6, 7, and 8 in Table 5.1, it is observed that these cases can be used to calculate the sensitivity of tumor motion amplitude to the tumor location in the liver.

The sensitivities are calculated based on Equation (5.3) from the simulated data.

The sensitivities of tumor motion amplitude in SI and AP direction to the tumor location in SI direction are:

$$S_{SI} = -2.1651e-4 \left[\frac{mm}{cm} \right], \quad S_{AP} = 0.0018 \left[\frac{mm}{cm} \right]. \quad (5.4)$$

The sensitivities to the tumor location in AP direction are:

$$S_{SI} = -0.0015 \left[\frac{mm}{cm} \right], \quad S_{AP} = -1.7853e-4 \left[\frac{mm}{cm} \right], \quad (5.5)$$

and the sensitivities to the tumor location in ML direction are:

$$S_{SI} = 5.5304e-4 \left[\frac{mm}{cm} \right], \quad S_{AP} = -2.7278e-4 \left[\frac{mm}{cm} \right]. \quad (5.6)$$

Note that all sensitivities are approximately zero, meaning that in this project, the tumor motion amplitude is not dependent on the tumor location in the liver.

According to [23, 12, 14] in Table 1.2, the results are different in the real case and with the human liver, the tumor motion depends on the tumor location. For example, the tumors which are closer to the chest have smaller motion amplitudes, and the tumors closer to diaphragm have larger motion amplitudes.

The reason why the tumor motion amplitude is sensitive to the tumor location in the real case is that the tissues of the liver, tumor, diaphragm, etc. are all deform-able and thus, the motions of different parts are not equal. However, it is not the case in this project. It means that the liver in the simulations and in the phantom is more similar to a rigid body than a deform-able organ and the motions of all points of the liver are approximately equal.

It is one of the limitations of the phantom and FE model that they were not able to mimic the liver deformations sufficiently. It can be caused by insufficient force in the actuators, latex skin, and diaphragm. Also, the tumor motion should have been smaller when it is closer to the latex skin (similar to the chest in real case).

5.3.2 Sensitivity of tumor motion to tumor size

It is possible to observe the effect of tumor size on the tumor motion amplitude by comparing the tumor motion data sets that are simulated in cases 1, 2, and 3 of Table 5.1.

Figure 5.4 illustrates the tumor motion plots in SI direction for different tumor sizes from case 1 and case 2. Note that the plots for tumor AP motion are similar.

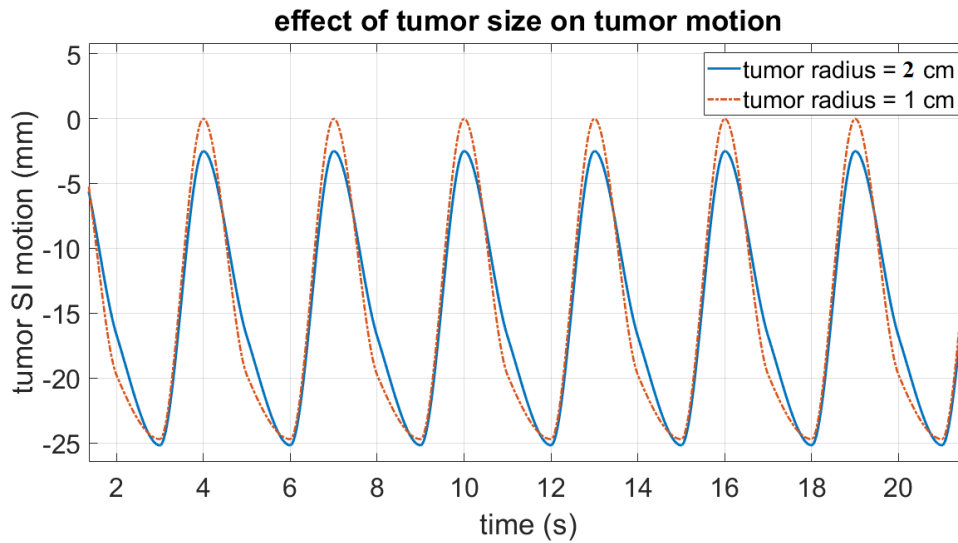


Figure 5.4: The simulated plots of tumor motion in SI direction for different tumor sizes (case 1 and case 2).

From the plot, it is observable that the tumor motion amplitude decreases by increasing the tumor size.

From the FE simulation data, the average sensitivity of tumor motion in SI and AP directions to the tumor radius calculated from Equation (5.3) are:

$$S_{SI} = -1.5577 \left[\frac{mm}{cm} \right], \quad S_{AP} = -0.1287 \left[\frac{mm}{cm} \right]. \quad (5.7)$$

Note that the sensitivities are negative, meaning that the tumor motion amplitude decreases by the increase of tumor radius.

According to [14, 23, 12, 20] in Table 1.2, in human body, larger tumors have smaller motion amplitudes and they reduce the liver motion as well. An explanation for this behavior can be

that larger tumors have larger weights and inertia and thus, it is more difficult for the liver and tissues to move the tumor, and they deform and change shape more than moving the tumor.

As mentioned in the previous part, the phantom and FE model have not been able to mimic the liver deformations sufficiently and it moves more rigidly than having deformations (and it could be caused by insufficient force in the actuators, latex skin, and diaphragm). However, similar to the real case, the sensitivity of the tumor motion amplitude to the tumor size is negative and is not zero. The reason can be that when the tumor is larger, the total weight and inertia of the liver and tumor is larger. Therefore, with the same amount of force (or air pressure), the motion amplitude decreases slightly.

5.3.3 Sensitivity of tumor motion to liver elasticity

By comparing the simulation results of cases 1, 4, and 5 in Table 5.1 and using the Equation (5.3), the sensitivities of tumor motion amplitudes in SI and AP directions to the liver elasticity are calculated:

$$S_{SI} = 0.2073 \left[\frac{mm}{kPa} \right], \quad S_{AP} = 0.0495 \left[\frac{mm}{kPa} \right]. \quad (5.8)$$

The positive sign of the sensitivities suggests that the tumor motion amplitude increases by having more liver elasticity (or more rigid liver). An explanation for this is as follows.

The tumor motion can be caused by two different sources: rigid body motion, and motion due to liver deformations. As mentioned in the previous parts, the deformations of the liver in the phantom and FE model are negligible, and the liver moves approximately rigidly (because of the insufficient force in the actuators, latex skin, and diaphragm). It means that the first mentioned source has more contribution to the tumor motion in this project. Therefore, with a higher liver elasticity (more rigid liver), the (rigid body) motion amplitude of the tumor increases.

To the author's knowledge, there is no study in the literature that describes the effect of liver elasticity (which is different between the patients) on the tumor motion. Since the real case is different with this project in having more liver deformations, it cannot be concluded whether the sensitivity of tumor motion amplitude to the liver elasticity is positive, negative, or zero in the real case.

5.3.4 Discussion

The sensitivity of the tumor motion amplitude to the parameters tumor size, liver elasticity, and tumor location in the liver which was obtained in this project can be summarized as:

$$S_{size} < 0, \quad S_{loc} \approx 0, \quad S_E > 0. \quad (5.9)$$

The answer to the second research question: The sensitivity of the tumor motion amplitude to the tumor size is negative, similar to the literature. The sensitivity to tumor location in the liver is negligible, while in the literature, the tumor location is an important factor. The difference between the results in the literature and in this work is mainly because the liver in real case has deformations, while in this project moves more like a rigid-body. It can be caused by insufficient force in the actuators, latex skin, and diaphragm (or any other limitations of the phantom). To the author's knowledge, there is no information about the sensitivity to liver elasticity in the literature. In this work, it has been obtained to be positive; however, it cannot predict the sensitivity to elasticity in the real case, because the liver model and the real human liver are different in having deformations. It can be concluded that the liver phantom and thus the FE model can improve by adding deformation and shape changes to the liver motion.

5.4 Generalization of the regression model

In Chapter 4, the data measured in the experiments have been used in regression models for tumor motion estimation. In this chapter, the experiments have been simulated by FE model and repeated for different values of parameters. Similar to the sensitivity analysis in which the simulations have been performed in difference cases, the simulations have been repeated for different values of parameters as shown in Table 5.1.

Note that in contrast to the sensitivity analysis, the simulations for this part of the project include random variations in order to make the data and therefore the resulting learning-based model more realistic. The motion has been randomized by adding or subtracting a random number to or from the motion amplitude, which can be maximum 10% of the motion amplitude. It means that the motion amplitudes vary randomly in the range $[0.9 - 1.1]d$ instead of a fixed amplitude d .

The purpose of this section is to generalize the learning-based model so that it includes various parameters which are different between the patients.

For this purpose, the features of the previous regression models in Chapter 4 which are the measured surrogate signals are now including the new features (parameters). It means that, in the generalized model, the features are the simulated surrogate signals as well as the parameters: tumor size, tumor location in the liver, and liver elasticity. Note that each surrogate signal is a vector of simulated values of length m , and each of the new features is a constant vector of length m in each case. Then, all cases are augmented in order to create the generalized features, output, and regression model.

Similar to Equation (4.1) in Chapter 4, the ordinary linear regression model can be written as:

$$y \approx y_{est}(\theta) = \sum_{i=0}^n \theta_i x_i + \alpha S + \beta L + \gamma E. \quad (5.10)$$

Now, y (the tumor motion) is the augmented vector obtained from all simulation cases, y_{est} is a vector of approximations of the output signal y , n is the number of features or simulated input signals, x_0 is a constant vector of ones, θ_0 is the bias term, x_i , $i = 1, 2, \dots, n$ are the augmented vectors of the simulated features or surrogates from all cases, S , L , and E are respectively the vectors of parameters: size, tumor location, and liver elasticity each of which is a vector augmented from constant vectors from all cases, and θ_i , $i = 1, 2, \dots, n$ as well as α , β , and γ are the resulting weights of the regression model.

Before explaining the estimation results and the errors, the plots of the correlation between the simulated input and output data are given in Figure 5.5. The simulated data are related to case 1 from Table 5.1.

By comparing the plots of Figure 5.5 with the plots of Figures 4.1 and 4.2 in Chapter 4 from the experimental data, it can be observed that the non-linear relationship between the surrogates and the output (tumor motion) and the "hysteresis"-like behavior exist more in the experimental data than in the simulated data. The fact that the simulation data are more linearly correlated than the experiments is one of the limitations of the FE model.

5.4.1 Linear regression model from the simulated data in all cases

The weights of the regression model in Equation (5.10) are obtained as explained in chapter 4. Since the correlation between the simulated tumor motion (output) and some of the surrogates (inputs) is very close to a linear relation (as shown in Figure 5.5), the estimation test errors become very small, which is not realistic and not comparable with the experimental results.

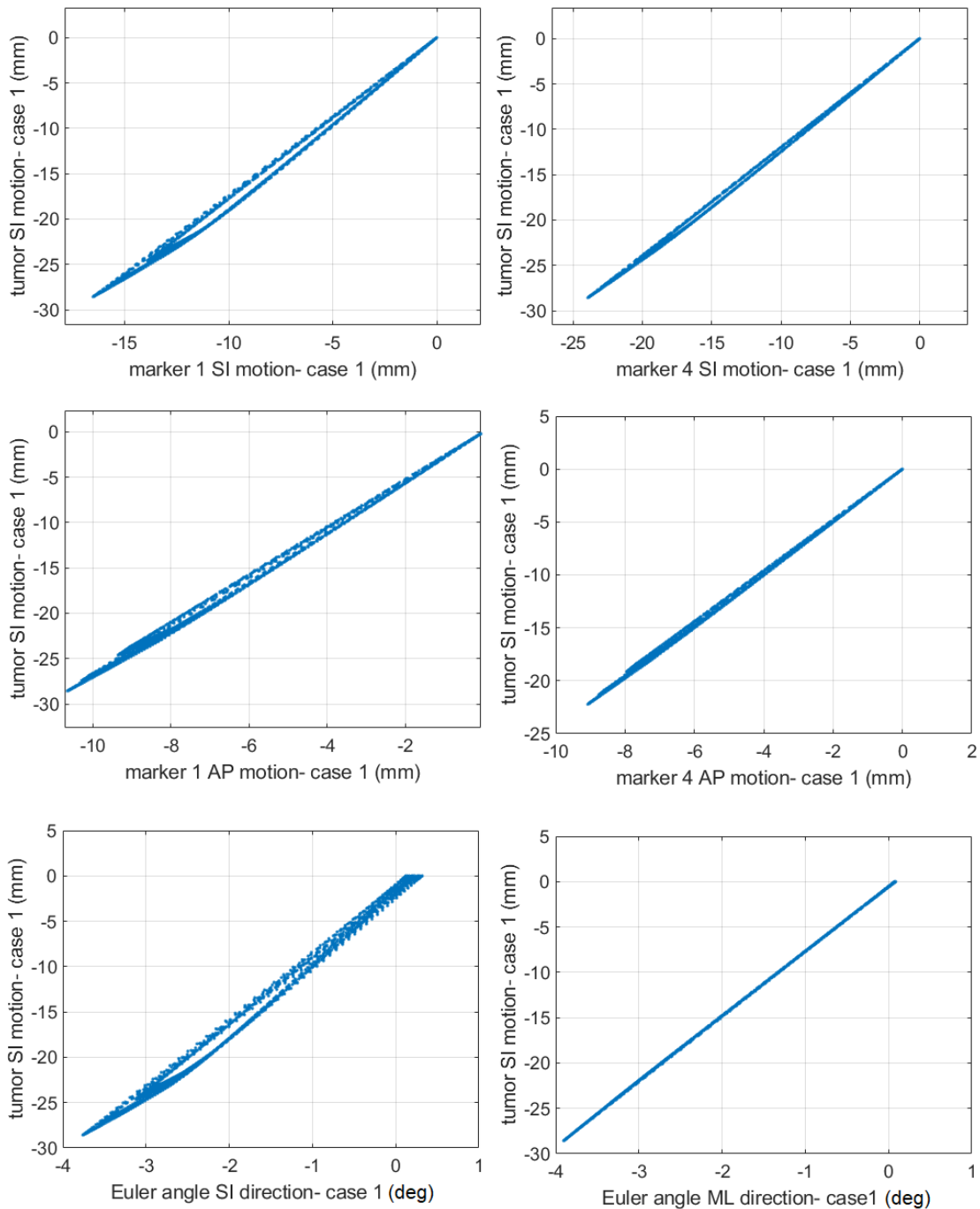


Figure 5.5: The plots of the relationship between some of the simulated input and output signals from case 1 of Table 5.1.

For the estimation of tumor motion in SI direction, the test error with the experimental data with randomized motion with ordinary linear regression model in Chapter 4 was:

$$e_{test} = 1.9\% \text{ with experimental data.}$$

However, for the data from the simulation of the same experimental case, the estimation error is:

$$e_{test} = 0.0013\% \text{ with simulated data,}$$

and the estimation error for all simulated data together (augmentation of all simulation cases in the generalized model) is:

$$e_{test} = 0.0078\% \text{ with all simulated data augmented.}$$

As mentioned above, the estimation errors are very small and unrealistic due to the fact that some of the input-output simulated data relations are linear. Therefore, the simulated features that have a perfectly linear relation with the tumor motion have been ignored in this project.

The remaining surrogates that have been considered in the generalized regression model are:

- Surrogate signals for the motion estimation in SI direction: marker 1 motion in SI and AP directions, the Euler angle in SI direction.
- Surrogate signals for the motion estimation in AP direction: the Euler angle in ML and SI directions.

By ignoring the unrealistic features, the estimation error of the generalized model becomes comparable to that of the experimental data model. For comparison, the errors are:

$$\begin{aligned} e_{test} &= 1.9\% \text{ with experimental data,} \\ e_{test} &= 5.2\% \text{ with experimental data with ignored features,} \\ e_{test} &= 1.2\% \text{ with simulated data with ignored features,} \\ e_{test} &= 2.2\% \text{ with all simulated data augmented with ignored features.} \end{aligned} \tag{5.11}$$

Figure 5.6 shows the plots of the simulated tumor motion by FEM and estimated motion by linear regression, from the augmented data (all simulation cases together). The plots suggest a reasonable motion estimation and are comparable with Figure 4.8 in Chapter 4.

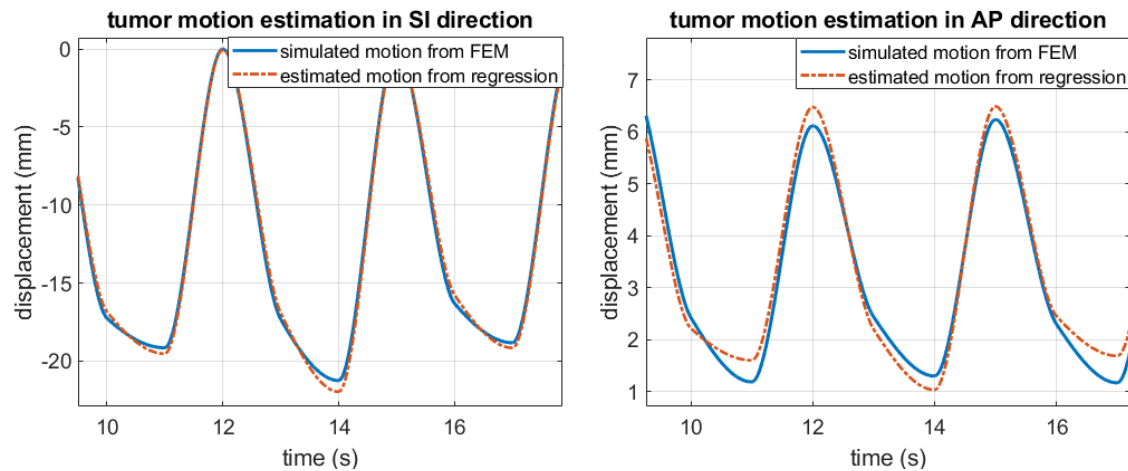


Figure 5.6: The plots of tumor motion simulated by FEM along with the estimated motion from the regression model with all data augmented (generalized model)

From the errors listed in Equation (5.11), a number of conclusions can be made:

- Like any other model, the FE model deviates from the experimental data. The main difference is in having non-linear relations between the surrogates and tumor motion. It can improve by creating a new phantom in which the liver has deformations, as discussed in the sensitivity analysis section.
- By generalizing the model, the estimation error increases. The estimation error from the simulation data with different parameters (augmented from different cases) is 2.2%, while the estimation error from only one simulation case (case 1) is 1.2%. It was expected, since by generalizing the regression model, more training and test data sets are included with more variations of the parameters. Therefore, the estimation error of the model with all simulation cases with different parameters is larger than only one simulation case.
- In the previous point, although the error of the generalized model is larger than that of only one case, the difference is small (about 1%). The reason why including the variety in the parameters is not increasing the error to a great extent is that the sensitivities of the tumor motion to the parameters are not large, as discussed in the previous sections.
- The estimation error from the experimental data is 5.2%, while the error from the same simulated case is 1.2%. It was also expected, since the simulation model has less amount of non-linearities and hysteresis comparing with the measured data.

5.4.2 Augmentation of the experimental data with FE simulated data of the same case

As mentioned before, one of the contributions of the FE model to this project is to increase the number of data sets for different cases and parameters in order to generalize the regression model. Also, one of the objectives of this project is to determine whether it is possible to extend the experimental data set by FEM and to what extent the FE model is a good representation of the experiments.

For this purpose, in this section, a comparison is made between the estimation error of the experimental data alone, with the same experimental data augmented with the FE simulated data. If the two errors are comparable, it means that the FEM has been successfully a good representation of the phantom.

First, an ordinary linear regression model is estimated from the experimental data set with random variations, similar to Chapter 4. Since some of the surrogates are ignored in the simulated data, the same features are ignored in the experimental data in order to have a fair comparison. In this case, the RMS test error of tumor motion estimation in SI direction is:

$$RMS(e_{\text{experiment}}) = 2.9 \text{ mm}, \text{ or } 8.3\%. \quad (5.12)$$

Then, the same data set from the experiment is augmented with the FEM simulated data set (from the same case and same parameters). If the data sets are augmented such that 50% of the data is from the experiment and the other 50% of the data is from the simulations, then the RMS estimation error of the new augmented data set is:

$$RMS(e_{\text{augmented}}) = 2.01 \text{ mm}, \text{ or } 5.7\% \quad (5.13)$$

The two obtained errors are comparable, meaning that the FE model has been successful in simulating, generating, and extending the experimental data set. However, there is a difference in the errors suggesting that like any other model, there is still a difference between the FE model and the experiments.

Note that in the real case and with the data from human body, the estimation errors are larger due to the existence of more motion variations and non-linearities. According to [25], the relative motion estimation errors in SI direction with ordinary linear regression are in the range 8-10% from the data measured from 3 patients in 6 sessions.

5.4.3 Discussion

In this section, the regression model for estimation of tumor motion has been generalized using the simulated data from FE model. The following conclusions can be made based on the results of this section:

- Like any other model, the FEM deviates from the experimental data. One of the limitations of the FE model is that it was not able to represent the non-linear relationships between the signals completely. Therefore, the relation between the inputs and output has been more linear and the estimation errors were smaller and less realistic.
- By generalizing the regression model and including different parameters in different cases, the estimation error increases as expected. However, the amount of the increase of the error is not significant, since the sensitivity of the tumor motion to the change of parameters is not large.

The answer to the last research question: By extending and augmenting the experimental data with simulated data, the average motion estimation error decreases. It was expected, since the simulated data includes less amount of non-linearities; therefore, it is less realistic. However, the change in the error is not significant, meaning that the FE simulation has modelled the experiments sufficiently well.

It is well-known that a model always deviates from the real system and cannot represent all aspects of the system completely. The answer to the question of to what extent a model is a good representation of the system depends on how much similarity is required in the specific applications.

In this project, a respiratory motion phantom has been created based on the real human body motion (an experimental model). Then, the phantom has been modeled by finite element methods (a simulation model). In both modeling procedures, there exists a specific amount of deviation, and the deviations can be observed by comparing the motion estimation errors. The motion estimation error from the real human data is larger than that of the phantom experimental data, and it is larger in the phantom data than the FEM simulated data. The reason is that in each step of modeling, some aspects of the system are neglected or simplified.

It can be concluded that both phantom and FE model have successfully modelled the respiratory motion of the liver and tumor. However, they still need improvements in order to become more realistic.

5.5 Summary

In this chapter, it was explained how the finite element model of the respiratory motion phantom along with the sensors have been created and validated by means of two different experimental data sets.

Then, with a sensitivity analysis, the effects of different parameters on the tumor motion amplitude have been investigated, which was the answer to one of the research questions of this project. By comparing the sensitivity analysis results based on the simulated data with the results from the literature, it was concluded that one of the main limitations of the FEM and phantom is that they cannot mimic the deformations of the liver well.

After that, it was explained how to generalize the regression model for tumor motion estimation using the simulated data. Next, the motion estimation errors based on the simulated data have been compared with those of the experimental data in order to check whether the simulated results are realistic.

Finally, by augmenting the experimental data with the simulated data (simulated from the same case and same parameters), it was concluded that although the FE model has some limi-

tations, it was able to extend the experimental data set with a reasonable similarity (the answer to the last research question).

6 Conclusion and recommendations

In this project, first, a previously designed and manufactured robotic phantom has been improved to represent the respiratory motion of the liver and liver tumor. Then, experiments have been performed to measure surrogate signals as well as the tumor motion. Next, different regression algorithms have been developed to map the surrogates to the motion of interest. Following that, a FE model of the experiment has been created to generate more data sets for different values of constant parameters. Then, a sensitivity analysis has been performed in order to understand the effect of the parameters on the tumor motion. Finally, it was evaluated whether the estimation results from the FE model agree with the experimental results.

The following paragraphs are the answers to the research questions:

- With the developed experimental phantom, there is no superiority regarding the effect of the surrogate signals on the estimation accuracy. It means that it is not possible to determine which surrogates have a higher correlation with the tumor motion, as it depends on the data set and variations between the patients that cannot be predicted. However, combination of all surrogates results in the most accurate case, meaning that the combination of the surrogates is the best choice of the surrogates.
- The effects of the parameters: tumor size, tumor location in the liver, and liver elasticity on the tumor motion are partly similar to the literature. The difference between the obtained results with the previous works is mainly due to the limitations of the phantom and FEM, and the fact that they have not been able to mimic the liver deformations well.
- By generating more data sets by FEM and extending the experimental data, the resulting motion estimation accuracy was comparable with that of the experimental data alone. It means that the FE model is a sufficiently good representation of the experimental data.

Also, the following points are important to mention:

- By Generalizing the regression model with different parameters tumor size, tumor location in the liver, and liver elasticity and using them as features of the regression model, the motion estimation error increases. It is expected, since by adding more variations and cases, the model becomes closer to a universal model.
- Like any other model, the respiratory motion phantom deviates from the real patients, and the FEM deviates from the phantom. The differences between the real case (patients) and the phantom data or the FE simulated data are inevitable and caused by the inherent errors in modelling the patients with the phantom, as well as modelling the phantom with FEM. For example, the non-linear relationship between the input and output signals from the phantom data has not been represented completely in the FE data. Also, some aspects of the phantom have been ignored or simplified for the sake of FEM creation, such as the air leakage from the AP actuator, or a layer of oil between the liver and latex skin. Another example is that the liver phantom deviates from the human livers by having a rigid-body motion instead of having deformations. Also, some other sources of errors are: the errors in the measurements during the experiments with phantom, the errors created by data interpolation, errors in validating the FEM, etc.

For future works, it is suggested to improve the phantom motion in AP direction as well (similar to the SI direction) and make it more realistic by adding variations in its motion.

Another suggestion regarding the phantom is to create a respiratory motion phantom with which the experiments are repeatable. Therefore, instead of FE modeling, the experiments can

be repeated reliably and the deviations caused by subsequent modelings (phantom model and then FE modeling) will decrease.

Also, the liver phantom should improve such that it mimics the liver deformations well, similar to the real human liver. For example, the force in the actuators, skin latex, and the diaphragm should be increased. Therefore, the problem of rigid-body motion of the liver that was discussed in the sensitivity analysis will be solved and the liver phantom will be more realistic. Also, some non-linear relationships between the surrogates and tumor motion will be created and the phantom will become more realistic.

Since the designed phantom is MR-compatible, it should be also used in an experimental setup with MR imaging to make it more realistic and similar to the experiments in clinics and deal with the challenges of MR imaging.

Additionally, efforts should be made in order to improve the algorithms and experiments to perform the measurements and estimation in real-time, which would be necessary to make this project applicable to real clinical procedures.

Regarding the image segmentation code and tracking the markers, some improvements can be made in order to make the image segmentation more robust to the changes in the ambient light. As discussed in Chapter 3, the main idea is to use hue, saturation, and value (HSV) coordinates for the image segmentation instead of using thresholds for RGB values. Since the hue represents the color, it is invariant and does not depend on the ambient light. By segmenting the colors based on hue, the color segmentation will become more robust to the ambient changes. Also, it is possible to choose the hue thresholds automatically and there is no need to change them for each experiment.

Another improvement to this project can be analyzing the effect of different breathing modes (deep, normal, shallow) on the tumor motion as well as on the estimation accuracy. It is also possible to create a classifier before the motion estimation with regression in order to separate the regression models of different breathing types.

In order to improve the mathematical estimation model for the real-time applications, one suggestion is to create an adaptive model, meaning that the parameters of the model change with time in order to model variations more accurately. Therefore, if the patient breaths differently, the model can adapt to the new respiratory motion.

As a final suggestion, ultrasound can also be employed to measure additional surrogate signals and compare with the surrogate signals used in this work.

A Arduino code for the phantom motion with digital regulator

```

1 int OutputPin = 11;
2 int solenoidPin = 13; //This is the output pin on Arduino
3
4 enum States {StepForward1, StepBackward1, StepForward2,
   StepBackward2, done};
5 States State;
6 int Read;
7
8 void setup()
9 { pinMode(OutputPin, OUTPUT);
10  pinMode(solenoidPin, OUTPUT); //Sets the pin as output
11 }
12
13 void loop()
14 {
15   Read = HIGH;
16   while (Read == HIGH) {
17     switch (State)
18     {
19       case StepForward1:
20
21         digitalWrite(solenoidPin, HIGH); //Switch Solenoid
           HIGH (right actuator is filling, the other two
           are becoming empty)
22         for (int i = 0; i <= 20; i=i+1) {
23           analogWrite(OutputPin, i);
24           delay(35); //increasing the pressure slowly
25         }
26         digitalWrite(solenoidPin, HIGH); //still the same
           actuator is working
27         for (int i = 20; i <=100; i=i+2) {
28           analogWrite(OutputPin, i);
29           delay(1); //increasing the pressure faster
30         }
31         State = StepBackward1;
32         break;
33
34       case StepBackward1:
35
36         digitalWrite(solenoidPin, HIGH); //still the same
           actuator is working
37         for (int i = 100; i >= 0; i=i-1) { //decreasing
           the pressure of incoming flow
38           analogWrite(OutputPin, i);
39           delay(10);
40         }

```

```
41     State = StepForward2;
42
43     break;
44
45     case StepForward2:
46
47         digitalWrite(solenoidPin, LOW); //Switch
           Solenoid LOW (right actuator is becoming empty,
           the other two are filling)
48         for (int a = 0; a <= 20; a=a+2) {
49             analogWrite(OutputPin, a);
50             delay(10); //increasing the pressure slowly
51         }
52         digitalWrite(solenoidPin, LOW);
53         for (int a =20; a <= 100; a=a+4) {
54             analogWrite(OutputPin, a);
55             delay(1); //increasing the pressure faster
56         }
57         State = StepBackward2;
58
59     break;
60
61     case StepBackward2:
62
63         digitalWrite(solenoidPin, LOW);
64         for (int a = 100; a >= 0; a=a-1) {
65             analogWrite(OutputPin, a);
66             delay(10); //decreasing the pressure of incoming
           flow
67         }
68         State = StepForward1;
69
70     break;
71
72     case done:
73         return;
74     break;
75
76 }
77 }
78 }
```

B MATLAB script for image segmentation based on color thresholds

```
1 %% defining the constant parameters
2 %The high and low color thresholds
3 redThresholdLow = 160;
4 redThresholdHigh = 260;
5 greenThresholdLow = 20;
6 greenThresholdHigh = 140;
7 blueThresholdLow = 30;
8 blueThresholdHigh =140;
9
10 smallestAcceptableArea = 500; %For removing the small
    objects from the segmented image
11 %% recording a segmented video from the original video
12 workingDir = tempname; %Directory path for saving the
    output video
13 mkdir(workingDir)
14 mkdir(workingDir,'images')
15 vid = VideoReader('v.avi'); %Reading the recorded video
16 l = 1;
17
18 while hasFrame(vid)
19     i = readFrame(vid); %Reading the recorded video frame
        by frame
20     filename = [sprintf('%03d',l) '.jpg']; %Directory path
        for saving the segmented images
21     fullname = fullfile(workingDir,'images',filename);
22
23     redBand = i(:, :, 1); %Defining the RGB bands
24     greenBand = i(:, :, 2);
25     blueBand = i(:, :, 3);
26
27     %RGB masks: color segmentation based on the thresholds
28     redMask = (redBand >= redThresholdLow) & (redBand <=
        redThresholdHigh);
29     greenMask = (greenBand >= greenThresholdLow) & (
        greenBand <= greenThresholdHigh);
30     blueMask = (blueBand >= blueThresholdLow) & (blueBand
        <= blueThresholdHigh);
31
32     img =(redMask & greenMask & blueMask); %The segmented
        image
33
34     img=bwareaopen(img, smallestAcceptableArea); %Deleting
        small objects
35
36     structuringElement = strel('disk',1); % Smooth the
        border
```

```
37  img = imclose(img, structuringElement);
38
39  img = imfill(img, 'holes'); % Fill in any holes
40
41  stats = regionprops(img, 'centroid'); %Finding the
      center of each marker
42  loc = cat(1, stats.Centroid);
43  m1x(1)=loc(1,1);  m1y(1)=loc(1,2);
44  m2x(1)=loc(2,1);  m2y(1)=loc(2,2);
45  m3x(1)=loc(3,1);  m3y(1)=loc(3,2);
46  m4x(1)=loc(4,1);  m4y(1)=loc(4,2);
47
48  imwrite(img,fullname) %Save the segmented image
49  l = l+1;
50 end
51
52 imageNames = dir(fullfile(workingDir, 'images', '*.jpg'));
53 imageNames = {imageNames.name}';
54
55 outputVideo = VideoWriter(fullfile(workingDir, 'segmented.
      avi')); %Saving the segmented video
56 open(outputVideo)
57
58 for f = 1:length(imageNames)
59     img = imread(fullfile(workingDir, 'images', imageNames{f
      }));
60     writeVideo(outputVideo, img)
61 end
62
63 close(outputVideo)
64
65 t=(1/outputVideo.FrameRate):(1/outputVideo.FrameRate):
      outputVideo.Duration; %Saving the time stamps as a time
      array
66
67 %% code for converting pixels to millimeter as well as
      converting from image X-Y coordinates to phantom SI-AP
      coordinates
68 n=25/106.5; %Coefficient of conversion
69
70 m1_SI= m1x*n; m1_AP= -m1y*n;
71 m2_SI= m2x*n; m2_AP= -m2y*n;
72 m3_SI= m3x*n; m3_AP= -m3y*n;
73 m4_SI= m4x*n; m4_AP= -m4y*n;
```

Bibliography

- [1] Ernst F; Martens V; Schlichting S.; Beširević A.; Kleemann M.; Koch C.; Petersen D.; Schweikard A. "correlating chest surface motion to motion of the liver using ϵ -svr – a porcine study". *Medical Image Computing and Computer-Assisted Intervention*, pages 356–364, 2009.
- [2] McClelland J.R.; Hawkes D.J.; Schaeffter T.; King A.P. "respiratory motion models: A review". *Medical Image Analysis*, (17):19–42, 2013.
- [3] Liu H.; Koch N.; Starkschall G.; Jacobson M.; Forster K.; Liao Z.; Komaki R.; Stevens C. "evaluation of internal lung motion for respiratory-gated radiotherapy using mri: Part ii—margin reduction of internal target volume". *International Journal of Radiation Oncology, Biology, Physics*, 60(5):1473–1483, 2004.
- [4] Koch N.; Liu H.H.; Starkschall G.; Jacobson M.; Forster K.; Liao Z.; Komaki R.; Stevens C.W. "evaluation of internal lung motion for respiratory-gated radiotherapy using mri: Part 1-correlating internal lung motion with skin fiducial motion". *International Journal of Radiation Oncology, Biology, Physics*, 60(5):1459–1472, 2004.
- [5] Langen K.; Jones D. "organ motion and its management". *International Journal of Radiation Oncology, Biology, and Physics*, 50(1):265–278, 2001.
- [6] Ahn S.; Yi B.; Suh Y.; Kim J.; Lee S.; Shin S.; Shin S.; Choi E. "a feasibility study on the prediction of tumour location in the lung from skin motion". *The British Journal of Radiology (BJR)*, 77(919):588–596, 2004.
- [7] Ahn S.; Yi B.; Suh Y.; Kim J.; Lee S.; Shin S.; Shin S.; Choi E. "a feasibility study on the prediction of tumour location in the lung from skin motion". *The British Journal of Radiology (BJR)*, 77, 2014.
- [8] Keall P.; Mageras G.; Balter J.; Emery R.; Forster K.; Jiang S.; Kapatoes J.; Low D.; Murphy M.; Murray B.; Ramsey C.; VanHerik M.; Vedam S.; Wong J.; Yorke E. "the management of respiratory motion in radiation oncology report of aapm task group 76". *Medical Physics*, 33(10):3874–3900, 2006.
- [9] Durichen R.; Davenport L.; Bruder R.; Wissel T.; Schweikard A.; Ernst F. "evaluation of the potential of multi-modal sensors for respiratory motion prediction and correlation". *International Conference of the IEEE Engineering in Medicine and Biology Society (EMBC)*, 2013.
- [10] Torshabi A.E.; Pella A.; Riboldi M.; Baroni G. "targeting accuracy in real-time tumor tracking via external surrogates: a comparative study". *Technology in Cancer Research and Treatment*, 9(6):551–561, 2010.
- [11] Legates D.; McCabe G.Jr. "evaluating the use of "goodness-of-fit" measures in hydrologic and hydroclimatic model validation". *Water Resources Research*, 35(1):233–241, 1999.
- [12] Ehrhardt J.; Werner R.; Schmidt-Richberg A.; Handels H. "statistical modeling of 4d respiratory lung motion using diffeomorphic image registration". *IEEE Transactions on Medical Imaging*, 30(2), 2010.
- [13] Hoymann H. "lung function measurements in rodents in safety pharmacology studies". *Frontiers in Pharmacology*, 2012.
- [14] Plathow C.; Fink C.; Ley S.; Puderbach M.; Eichinger M.; Zuna I.; Schmähl A.; Kauczor H. "measurement of tumor diameter-dependent mobility of lung tumors by dynamic mri". *Radiology and Oncology*, 73(3):349–354, 2004.
- [15] Tehrani J.; Yang Y.; Werner R.; Lu W.; Low D.; Guo X.; Wang J. "sensitivity of tumor motion simulation accuracy to lung biomechanical modeling approaches and parameters".

Physics in Medicine and Biology, 60, 2015.

- [16] Werner R.; Ehrhardt J. "patient-specific finite element modeling of respiratory lung motion using 4d ct image data". *Medical Physics*, 36(5):1500–1511, 2009.
- [17] Lu W.; Low D.A.; Parikh P.J.; Nystrom M.M.; Naqa I.M.; Wahab S.H.; Handoko M.; Fooshee D.; Bradley J.D. "comparison of spirometry and abdominal height as four-dimensional computed tomography metrics in lung". *Medical Physics*, 2005.
- [18] Hoisak J.D.; Sixel K.E.; Tirona R.; Cheung P.C.; Pignol J.P. "correlation of lung tumor motion with external surrogate indicators of respiration". *International Journal of Radiation Oncology, Biology, and Physics*, 2004.
- [19] Schweikard A.; Glosner G.; Bodduluri M.; Murphy M.J.; Adler J.R. "robotic motion compensation for respiratory movement during radiosurgery". *Computer Aided Surgery: Official Journal of the International Society for Computer Aided Surgery*, 5(4):263–277, 2000.
- [20] Cai J.; Read P.; Shenga K. "the effect of respiratory motion variability and tumor size on the accuracy of average intensity projection from four-dimensional computed tomography: An investigation based on dynamic mri". *Medical Physics*, 35(11):4974–4981, 2008.
- [21] Clifford M.; Banovac F.; Levy E.; Cleary K. "assessment of hepatic motion secondary to respiration for computer assisted interventions". *Computer Aided Surgery*, 2002.
- [22] King A.; Boubertakh R.; Ng K.; Ma Y.; Chinchapatnam P.; Gao G.; Schaeffter T.; Hawkes D.; Razavi R.; Rhode K. "a technique for respiratory motion correction in image guided cardiac catheterisation procedures". *Proceedings of SPIE - The International Society for Optical Engineering*, 2008.
- [23] Liu H.H.; Balter P.; Tutt T.; Choi B.; Zhang J.; Wang C.; Chi M.; Luo D.; Pan T.; Hunjan S.; Starkschall G.; Rosen I.; Prado K.; Liao Z.; Chang J.; Komaki R.; Cox J.D.; Mohan R.; Dong L. "assessing respiration-induced tumor motion and internal target volume using four-dimensional computed tomography for radiotherapy of lung cancer". *International Journal of Radiation Oncology, Biology, Physics*, 68(2):531–540, 2007.
- [24] Lifeinharmony. "anatomy of stomach and diaphragm". <http://www.lifeinharmony.me/anatomy-of-stomach-and-diaphragm/>, 2018. [Online; accessed 27-August-2018].
- [25] Fahmi S.; Simonis F.; Abayazid M. "respiratory motion estimation of the liver with abdominal motion as a surrogate". *The International Journal of Medical Robotics and Computer Assisted Surgery*, 2018.
- [26] Plathow C.; Zimmermann H.; Fink C.; Umathum R.; Schöbinger M.; Huber P.; Zuna I.; Debus J.; Schlegel W.; Meinzer H.; Semmler W.; Kauczor H.; Bock M. "influence of different breathing maneuvers on internal and external organ motion: Use of fiducial markers in dynamic mri". *International Journal of Radiation Oncology, Biology, Physics*, 62(1):238–245, 2005.
- [27] University of Michigan Medical School. "basic body plan and patterns". <https://sites.google.com/a/umich.edu/bluelink/curricula/first-year-medical-curriculum/sequence-1-Foundations/session-1-basic-body-plan-patterns/s11o>, 2018. [Online; accessed 27-August-2018].
- [28] Isaksson M.; Jalden J.; Murphy M.J. "on using an adaptive neural network to predict lung tumor motion during respiration for radiotherapy applications". *Medical Physics*, 2005.
- [29] Abayazid M.; Kato T.; Silverman S.G.; Hata N. "using needle orientation sensing as surrogate signal for respiratory motion estimation in percutaneous interventions". *International Journal of Computer Assisted Radiology and Surgery*, 13(1):125–133, 1 2018.

- [30] Mathur N. "computational modeling of soft actuators of an mr-compatible robotic phantom that mimics respiratory motion of the liver". Master's thesis, University of Twente, 2018.
- [31] World Health Organization. "cancer". <http://www.who.int/news-room/fact-sheets/detail/cancer>, 2018. [Online; accessed 20-July-2018].
- [32] World Health Organization. "early cancer diagnosis saves lives, cuts treatment costs". <http://www.who.int/news-room/>, 2018. [Online; accessed 20-July-2018].
- [33] Costa P. "mr-compatible soft actuation phantom to simulate respiratory motion in liver". Master's thesis, University of Lisbon, 2018.
- [34] Jin P. "prostate tracking using 3d active appearance models with 2d fitting: feasibility testing with deformable prostate phantom". Master's thesis, University of Twente, 2013.
- [35] Ionascu D.; Jiang S.; Nishioka S.; Shirato H.; Berbeco R. "internal-external correlation investigations of respiratory induced motion of lung tumors". *Medical Physics*, 2007.
- [36] Lei P.; Moeslein F.; Wood B.; Shekhar R. "real-time tracking of liver motion and deformation using a flexible needle". *International Journal of Computer Assisted Radiology and Surgery*, 6(3):435–446, 2012.
- [37] Vedam S.S.; Kini V.R.; Keall P.J.; Ramakrishnan V.; Mostafavi H.; Mohan R. "quantifying the predictability of diaphragm motion during respiration with a noninvasive external marker". *Medical Physics*, 30(4):505–513, 2004.
- [38] Dr. Artour Rakhimov. "normal respiratory frequency, volume, chart, ...". <https://www.normalbreathing.com/index-nb.php>, 2018. [Online; accessed 11-September-2018].
- [39] Beddar A.S.; Kainz K.; Briere T.M.; Tsunashima Y.; Pan T.; Prado K.; Mohan R.; Gillin M.; Krishnan S. "correlation between internal fiducial tumor motion and external marker motion for liver tumors imaged with 4d-ct". *International Journal of Radiation Oncology, Biology, and Physics*, 2007.
- [40] Cerviño L.I.; Chao A.K.; Sandhu A.; Jiang S.B. "the diaphragm as an anatomic surrogate for lung tumor motion". *Physics in Medicine and Biology*, 2009.
- [41] Cerviño L.I.; Jiang Y.; Sandhu A.; Jiang S.B. "tumor motion prediction with the diaphragm as a surrogate: a feasibility study". *Physics in Medicine and Biology*, 2010.
- [42] Bosch Sensortec. "bno055". https://www.bosch-sensortec.com/bst/products/all_products/bno055, 2018. [Online; accessed 24-October-2018].
- [43] American Cancer Society. "liver cancer stages". <https://www.cancer.org/cancer/liver-cancer/detection-diagnosis-staging/staging.html>, 2018. [Online; accessed 18-September-2018].
- [44] American Cancer Society. "treatment of liver cancer, by stage". <https://www.cancer.org/cancer/liver-cancer/treating/by-stage.html>, 2018. [Online; accessed 20-July-2018].
- [45] Chi P.; Balter P.; Luo D.; Mohan R.; Pan T. "relation of external surface to internal tumor motion studied with cine ct". *Medical Physics*, 2006.
- [46] Shin D.; Kang S.; Kim D.; Kim T.; Kim K.; Koo H.; Cho M.; Ha J.; Yoon D.; Suh T. "development of an advanced deformable phantom to analyze dose differences due to respiratory motion". *Progress in Medical Physics*, pages 1–10, 2017.
- [47] Image Analyst The MathWorks, Inc. "simple color detection". <https://nl.mathworks.com/matlabcentral/fileexchange/26420-simplecolordetection>, 2018. [Online; accessed 23-September-2018].

- [48] Inc. The MathWorks. "coefficient of determination (r-squared)". <https://nl.mathworks.com/help/stats/coefficient-of-determination-r-squared.html>, 2018. [Online; accessed 15-October-2018].
- [49] Inc. The MathWorks. "ridge". <http://nl.mathworks.com/help/stats/ridge.html>, 2018. [Online; accessed 29-September-2018].
- [50] Cancer Research UK. "tests to diagnose". <https://www.cancerresearchuk.org/about-cancer/liver-cancer/getting-diagnosed/tests-diagnose>, 2018. [Online; accessed 20-July-2018].
- [51] Cancer Research UK. "treatment". <https://www.cancerresearchuk.org/about-cancer/liver-cancer/treatment>, 2018. [Online; accessed 20-July-2018].
- [52] Andrew Ng; Stanford University. "machine learning". <https://www.coursera.org/learn/machine-learning>, 2018. [Online; accessed 29-September-2018].
- [53] vanVeen Y.; Jahya A.; Misra S. "macroscopic and microscopic observations of needle insertion into gels". *Journal of Engineering in Medicine*, 226(6):441–449, 2012.
- [54] Markidou A.; Shih W.; Shih W. "soft-materials elastic and shear moduli measurement using piezoelectric cantilevers". *Review of Scientific Instruments*, 76, 2005.
- [55] Nava A.; Mazza E.; Furrer M.; Villiger P.; Reinhart W. "in vivo mechanical characterization of human liver". *Medical Image Analysis*, 12:203–216, 2008.
- [56] Park J.C.; Park S.H.; Kim J.H.; Yoon S.M.; Song S.Y.; Liu Z.; Song B.; Kauwelo K.; Webster M.J.; Sandhu A.; Mell L.K.; Jiang S.B.; Mundt A.J.; Song W.Y. "liver motion during cone beam computed tomography guided stereotactic body radiation therapy". *Medical Physics*, 39(10):6431–6442, 2012.
- [57] Miao D.; Zhao H.; Hong H.; Zhu x.; Li C. "doppler radar-based human breathing patterns classification using support vector machine". *IEEE Radar Conference (RadarConf)*, 2017.
- [58] Lu Q.; Ling W.; Lu C.; Li J.; Ma L.; Quan J.; He D.; Liu J.; Yang J.; Wen T.; Wu H.; Zhu H.; Luo Y. "stiffness value and ratio to discriminate malignant from benign focal liver lesions". *Journal of Engineering in Medicine*, 275(3):880–888, 2015.